ISSN 1916-9639 (Print)
ISSN 1916-9647 (Online)

APPLIED PHYSICS RESEARCH

CANADIAN CENTER OF SCIENCE AND EDUCATION®

Vol. 9, No. 6 December 2017

Editorial Board

Contents

Applied Physics Research; Vol. 9, No. 6; 2017
ISSN 1916-9639 E-ISSN 1916-9647
Published by Canadian Center of Science and Education

An experimental result coming from Neutrino research gives for all particles the ratio (s_i /m_i) defined by Quantum Inertial theory in conjunction with the Micro-quanta paradigm

Maurizio Michelini[1]

[1] ENEA-Casaccia Research Centre - Rome, Italy

Correspondence: Maurizio Michelini, ENEA-Casaccia Research Centre, Rome, Italy. E-mail: m_michelini@alice.it

Received: July 26, 2017 Accepted: August 11, 2017 Online Published: October 19, 2017

doi:10.5539/apr.v9n6p1 URL: https://doi.org/10.5539/apr.v9n6p1

Abstract

Rejecting some old misconceptions (such as the "pulling" gravitation that ravaged classical physics) the Inertial-Gravitational theory supported by the Micro-quanta paradigm incorporates both the relativistic concepts of *Mass - Momentum - Energy* and the *quantic Inertial Model* of the particle mass. The flux of micro-quanta supports primarily the physical interaction that *generates* the Inertial forces defined by Newton. Scholars believing that Inertial forces originate from the properties of the *empty space*, do not pertain to the community of physicists believing on Newton's Inertial Law. This great ancient physicist admitted he was unable to explicit the physical nature of his Law of Inertia ("*Hypotheses non fingo*"). However, marking the difference between "*empty*" and "*absolute*" space, he remained in his conviction that some unknown physical reality *originates* (in the absolute space) the inertial forces upon accelerated masses. At present, Micro-quanta paradigm describes the quantic objects that generate through collisions the *physical* inertial forces on particles. Since the flux of micro-quanta fills all space, there is no need to refer these collisions to some external System of reference. The relative velocity between quanta and particles comes out from the momentum that micro-quanta confer to particles. By this reason the Micro-quanta paradigm defines on *pure dynamical* bases the relativistic formalism that Special relativity derived from kinematics, so creating flaws that produced the well known paradoxes. To reveal the micro-quanta it's not necessary to devise particular experiments. The technique of the accelerometers has given many evidences of the physical reality guessed by Newton to explain inertial forces exerted on masses. Since the action of micro-quanta is always manifested in *statistical* terms, classical and relativistic physics allowed to describe Inertia and Gravitation *without knowing the quantic nature* of these phenomena. The micro-quanta Paradigm shows in particular the proportionality between cross section and mass (ratio A_u) of all particles colliding with micro-quanta. To the aim of calculating the transmission across matter of micro-quanta and neutrinos (which show the same nature) the only unknown quantity is the numerical value of the ratio A_u. Recalling that micro-quanta flux fills all space, it appears also interesting to search about neutrino collisions with micro-quanta flux as possible cause of the *oscillations* phenomena that occur during neutrino travels across the (so called) astronomic "empty" space. A quantitative indication on the ratio A_o is found in this paper from an experimental measurement of the solar neutrino flux interacting with the Earth mass in the course of the Borexino research carried out at Gran Sasso National Laboratory.

1. Introduction

Quantum Inertia-Gravitation theory is derived, according to the *strict* Equivalence principle, from the Micro-quanta paradigm proposed in 2007 to describe both inertial and gravitational forces originating from the collisions on particles of the Micro-quanta isotropic flux. Derivation of Mass and Momentum of particles moving in space filled by Micro-quanta flux can be done through Compton's collision law. This procedure shows the same formal description of *Mass - Momentum - Energy* given by Special Relativity, but their significance is greater because now the relativistic quantities are generated from *dynamical* bases, whereas S.R. was developed within an empty space through kinematical bases that are responsible for some well known troubling paradoxes. This means that

the new theory is more adherent to the physical nature of dynamical phenomena since it gives indications about the (very small) cross sections characterising particles respect to the incident micro-quanta, which show the same very low interaction with matter that characterises neutrinos. The numerical constants of Micro-quanta (energy, wavelength, flux) may be derived from the *Quantum Pushing* Gravity force originated by the shielding-effect of micro-quanta flux between two particles. This requires dropping the Newton's *pulling* gravitation and cancelling the misconception of the "*gravitational" mass*" that was debated by classical physics. The I*nertial mass* becomes the only mass that can be measured. On the other hand, the recent measurements of the gravitational constant G examined by the Committee of NIST Institute (CODATA 2014) showed discrepancies among them with standard relative uncertainty equal to $4.7x10^{-5}$. This value has to be compared with the uncertainty of other fundamental constants of physics. For instance : Quantum magnetic flux = $6.1x10^{-9}$, Fine structure constant = $2.3x10^{-10}$, Electron mass = 1.2 , Atomic mass constant = $1.2x10^{-8}$, etc. Leaving to CODATA his proper evaluations, I'm convinced that the high discrepancies on the measured G are the symptom of the statistic nature of the so called "universal" gravitational constant proposed by the old *pulling* gravity. The reason may be guessed recalling that the gravitational *pushing* force (due to the mutual shielding between particles immersed in the micro-quanta flux) is pulsating due to the relative positions occupied (for very small times) by adjacent particles that are pushed each other by the incident micro-quanta. In fact, contrary to the absence of any "*macroscopic shield*" postulated by classical Gravitation, the *Pushing* gravity cannot exclude that some fraction of nucleons constituting the test mass may not participate (for a fraction of time) to the macroscopic pushing force. Besides, the uncertain nature of the mass has been enlightened during the half-century research on the Higgs problem, that recently produced the large boson observed at CERN accelerator. Such result appeared disappointing. In his article "*My life as a boson*" P. Higgs observed that it was far from the original concept suggested in his paper (1964) which described an "*invisible field strewn across space, so to give mass every object in the universe*". The parallelism between this original picture and the flux of micro-quanta (that generates the mass of particles by collective collisions on charges) appears evident (see *Inertial model* of particles, paragr.3). In addition to these scientific activities, the experimental evidence of the physical reality guessed by Newton is today given by some widely used commercial devises. Not many physicists have considered that the accelerometers are able to measure the *absolute* acceleration (no recourse to some external reference system) by calculating (Newton) the ratio between the *measured inertial force* and the test mass. Accelerometers are widely used not only in aerospatial applications, but also in the field automobile incidents, mechanical analysis, smartphones, etc.

The structure of *Quantum Inertia-Gravitation* theory allows discovering new effects unknown to current physics. For instance, the mysterious "oscillations" that neutrinos undergo travelling across the so called "*empty*" cosmic space, receive new theoretical interest thinking that all space is filled by physical micro-quanta.

1.1 Theoretical and Empirical Bases of Micro-Quanta

Defining and calculating Quantum Gravitational force is possible only by defining the structure of both Inertial and Gravitational Interactions, that classical and relativistic physics showed to be tightly linked. The *strict Equivalence principle* assumed that both inertial and gravitational forces originate from the *same* physical reality. In the present paper the flux of Micro-quanta paradigm is analysed in order to verify this requirement. Some historical *misconceptions* gave rise to *unphysical* concepts, such as the "*unlimited"* gravitational collapse depending entirely on the characteristics of the old *pulling* gravitation. In nature there are many examples of gravitational collapses, among which the spectacular collapses of Supernovae, enlighting for months a whole galaxy. But this collapse isn't *unlimited* because in the places with remnants of supernovae it has been observed the presence of Neutron stars whose mass is of the order of some Sun masses. After the theoretical study about the finite volume of the gravitational collapsing bodies (Loinger, 2010), some papers showed (Michelini, Jan. 2010, Nov. 2010) that Micro-quanta paradigm, which does not shows the gravitational unlimited collapse, is able to explain some observed- phenomena, such as the mysterious cause that ended Glacial Eras. This cause is still waiting a physical explanation that did not come from the great effort developed by two international missions in Antarctica: VOSTOK (Petit et al., 1999) and EPICA (Augustin et al., 2004) which extended the drilled Ice cores up to one million years ago. Besides, some experimental observations (such as the excess infrared emissions from planets, the planetary physics, the Earth high seismicity) are still waiting a rational explanation. For instance, the strong seismic events on Earth and other planets (with the satellite Io) appear to be linked to planets which show *solid crust*. In fact these events may be attributed to the same cause found analysing the Dansgaard-Oeschger events. Firstly observed by drilling two Ice cores in Greenland (Stuiver & Grootes, 2000) these phenomena revealed large and rapid warmings on both hemispheres at *regular* interval around 1470 years. At a first time, this regularity was attributed to some astronomical events, but the analysis carried out by S.Ramstorf on the D-O events between 11,500 and 45,000 years B.P. (Ramstorf, 2003) showed that actually the standard deviation from the most

probable period was about 120 years. This result ruled out any possible astronomical influence. Taking in mind that the release of energy from micro-quanta collisions on the Earth mass amounts to a thermal power around 2.6 $x10^{15}$ watt, I put forward the hypothesis (Michelini, 2011) that the *quasi-regular* D-O rapid warming events may be triggered by a low increase of the internal temperature producing a thermal expansion of the mass able to produce an increase of the planet radius (some metres) sufficient to induce tensile stresses on the solid crust surpassing the elastic limit of the rocks. This produces fractures through which the fluid magma penetrates across the crust, giving rise to orogenesis, to large earthquakes and to the continuos volcano activities. In the D-O events the fracturing process regarded two hemispheres (Raisbeck, 2007). When the snow cup and the clouds mantle became so thick to prevent the solar energy might reach the surface, the global temperature was so low that no external phenomenon couldn't warm the planet. What gave the thermal energy that put Glacial Eras to an end? Probably it was the periodic heating of the surface produced by the magma escaping through fractures open on the stressed crust by thermal *expansion* of internal mass due to power generated by micro-quanta collisions.

During this research I was encouraged by the rising of new problems put on the table of scientific community by the Neutrino research, whose detectors require specific locations, such as old mines of coal and other natural or artificial shields against the radioactive cosmic rays. Such rough materials, disregarded by the classical physics, became the key for detecting the advanced physics of neutrinos,, The widely use by theorists of the classical astronomic observations, to proof their theories, inaugurated by Einstein at beginning of XX century, was definitely set.

2. Characteristics of Micro-quanta paradigm versus Special Relativity

Since *Quanta of energy* are defined ($E = h\nu$) independently of their size, then micro-quanta interact with particles in the same way as photons (Compton's equation). The micro-quanta , filling the space, act as interaction waves of the *Inertia* of particles. The momentum of particles was defined by classical physics $\mathbf{q}_i = m_o\mathbf{v}$ in the *empty* space. Now this quantity comes out in a proper form when the space is filled by micro-quanta with energy $E_o = h_o\nu_o$ which transmit power to the particles through the Doppler frequencies (ν_f, ν_b) whose definition can be derived from Micxro-quanta paradigm. These values are linked to the relative velocity of the micro-quanta incident *forward* (c+v) or *behind* (c - v) the particle. The old bargain required by S.R. for summing or detracting high velocities can be now dropped since in the case of collisions between micro-quanta and particles these ones are described with proper kinematical characteristics. The mathematical proof (M.Michelini, Nov.2010) shows simply that each particle receives the momentum

$$| \mathbf{q} | = (h_o/c)\,(\nu_b - \nu_f)\,N_i = (E_o/c\nu_o)\,(\nu_b - \nu_f)\,N_i$$

where $N_i = \sigma_t\,\phi_o\,\tau_o$ is the number of incident micro-quanta during the time τ_o of each *collective* collision. Substituting and performing the calculation one obtains

$$\mathbf{q}_t = \sigma_t\,(E_o\,\phi_o\,\tau_o/c^2)\,\mathbf{v} / (1 - v^2/c^2)^{1/2}.$$

This equation reproduces the relativistic formalism of momentum

$$\mathbf{q}_t = m_i\,\mathbf{v} / (1 - v^2/c^2)^{1/2}$$

with a new term that transfors the particle cross section in the rest-mass

$$m_i = \sigma_t\,[p_o\,\tau_o/c] \tag{2}$$

where $p_o = E_o\,\phi_o/c$ is the energy density of micro-quanta in space. The term in brackets is constant for all particles because it depends on micro-quanta constants, so that the ratio

$$A_o = \sigma_t / m_i = c / p_o\,\tau_o \tag{2a}$$

represents a fundamental result that gives the cross section encountered by micro-quanta incident on a particle with mass m_i. In other words the present approach, based on *dynamical* quantities, shows that the particle mass *originates* from interaction of micro-quanta on the charges. This fulfils in principle the mechanism originally suggested by P. Higgs in 1964. On the contrary, Special Relativity obtained the "relativistic" formalism assuming an *empty space* and using *kinematical* equations that produced *erroneous* predictions, such as the well known paradoxes, the "transverse" mass and the Fitzgerald's contraction. Micro-quanta do collective collisions on the cross section σ_t $o\phi$ particles during the time τ_o.. Since the *average density* of micro-quanta in space equals $n_o = \phi_o/c$, the average distance between two micro-quanta is $x_o = (1/n_o)^{1/3}$. We assume that the duration of collision $\tau_o = x_o/c$ equals the time necessary to cover the average distance x_o between two adjacent micro-quanta travelling on the same beam, so hitting the particle at any average interval τ_o. Now we use (to continue

the present reasoning) the numerical values given in par.5 after the calculations of the micro-quanta constants performed by implementing the preceding paragraphs. So, using the value $x_o = 4.526x10^{-32}$ resulting from eq(5a) we obtain the duration of the *collective* collision

$$\tau_o = 1{,}508x10^{-40}\ \text{sec.} \tag{2}$$

To verify this result we recall that the energy ΔE released by each quantum colliding on the particle is fixed by the *Conpton's equation*. Let's recall that each incident micro-quantum release also to the particle a momentum that is statistically balanced by the action of its diametrically opposite momentum, preserving the total momentum of any free particle. In the case of micro-quanta ΔE satisfies the ratio

$$\Delta E = E_o\,(E_o / m_i c^2)$$

which, adopting the value $E_o = 1.289x10^{-32}$ resulting from eq(5b), gives us the ratio $(E_o / m_i c^2)$ for any particle. For instance, nucleons (that constitute 99,95% of the neutral masses) take the value

$$E_o / m_n c^2 = 8.5933x10^{-23}. \tag{2a}$$

The total energy $N_i \Delta E$ released by a *collective* collision with generic duration τ, corresponds to

$$N_i = \sigma_\iota\, \phi_o\, \tau$$

which is the number of colliding micro-quanta in the Compton's equation

$$N_i \Delta E = E_o\,(E_o / m_i c^2)\,(\sigma_\iota\, \phi_o\, \tau)\,. \tag{2b}$$

The energy ΔE released by each micro-quantum is a small fraction of the energy E_o. We observe that in the preceding equation both sides result equal to E_o when the number $N_i = (\sigma_\iota\, \phi_o\, \tau)$ equals

$$(\sigma_\iota\, \phi_o\, \tau) = (m_i c^2 / E_o). \tag{2c}$$

This gives a correlation between the number of micro-quanta of a collective collision (duration τ) and the mass-energy $m_i c^2$ of any particle. To this aim we rearrange eq(2c) in the form

$$\sigma_\iota / m = A_o = (c^2 / E_o\, \phi_o\, \tau) = (c / p_o\, \tau) \tag{2d}$$

which confirms eq(1a) implying that $\tau = \tau_o$ as expected. Some trouble arises from the relative increase of mass of particles at any collective collision $Y = \Delta m_i / m_i = \Delta E / m_i c^2 = (E_o / m_i c^2)^2$. In the case of nucleons the velocity of increment is

$$\Delta Y / \tau_o = (E_o / m_i c^2)^2 / \tau_o$$

which is troubling. However we don' forget that the Inertial Model of particle have to g ive answers to the still hidden process of rapid collapses shown by instable particles., which may grow or disappear.
Let's now show what happens to the duration of collision τ derived from eq(2d)

$$\tau = (c^2 / A_o\, \phi_o\, E_o) \tag{2e}$$

when we assume the value $A_o \approx 1.43x10^{-14}$ coming from an experimental result of the Neutrino research described in parag. 4. Substituting the numerical values of ϕ_o and E_o found in parag. 5 in conjunction with the assumed value of A_o, we calculated $\tau = 1.506x10^{-40}$ sec. Comparison with $\tau_o = 1.508x10^{-40}$ sec given by eq(2) shows a little difference that may depend on the assumed A_o. Considering that τ_o has been calculated through a radically different procedure (based on the average distance x_o between two adjacent micro-quanta travelling on the same beam) τ_o might be in principle *very different* from τ. This did not happen, supporting our theory.. Another point to be enlightened is the existence of a value of A_o derived directly from theoretical way.

3. The Inertial Model of particles

The fundamental time interval τ_o scans the rhythm of collisions of micro-quanta upon matter in the universe. Notice that their average distance x_o is much smaller than the "size" of elementary particles. For instance the "radius" of a nucleon r_n is about 10^{-20}. The energy of the particle is given multiplying the energy E_o by the number N_i of micro-quanta in a collective collision $N_i E_o = \sigma_i \phi_o E_o \tau_o = \sigma_i p_o x_o$. Recalling the electromagnetic energy $m_i c^2$ of particles, the balance of these quantities gives

$$m_i c^2 = N_i E_o = \sigma_i\, p_o x_o\,. \tag{3}$$

which expresses the Inertial Model of stable particles. Resuming , this model presents shell-particles with cross

section σ_i and thickness x_o much less than radius,. In fact eq(3) can be interpreted as the product of the particle volume ($\sigma_i x_o$) of thin shells multiplied by the energy density $p_o = \phi_o E_o/c$ of micro-quanta in space. In other words, the colliding micro-quanta are scattered by the *repulsive* forces between the uniformly charged micro-particles that constitute the charge and the mass confined within a sphere whose surface represents the cross section of particles. In other words, the flux of recoiling micro-quanta act the confinement of the repulsive micro-charges constituting the elementary charge. In practice the repulsive electric force is balanced by the newtonian force of inertia $F_{in} = - m^*(\Delta v/\Delta t)$ due to each scattered micro-quantum (mass $m^* = E_o/c^2$) that undergoes the re-direction ($\Delta \mathbf{v}/\Delta t$) of the velocity **c**. The statistical distribution of the collisions generates the "compression" p_o upon the micro-charges Δe that repel each other. Taking in mind the reasoning given in parag.6 (substantially affirming that $\Delta t = \tau_o$) we may affirm that the Inertial model of particles is based on Newton's concept that mass of particles *is generated by the momentum re-direction* of an isotropic flux of incident micro-quanta. Rearranging eq(3) gives us the ratio

$$A_o = \sigma_i / m_t = c^2 / p_o x_o = c^3 / \phi_o E_o x_o \tag{3a}$$

which confirms eq(1a) stating the *uniformity* of this ratio : a fundamental result of the Micro-quanta paradigm. This fact is not present in Special Relativity because it assumed the concept of "*empty*" space, widely accepted at beginning of XX century, that ignored other physical realities possibly present in space.

4. An experimental result coming from Neutrino research

Let's analyse the structure of eq(3a): we don't know all micro-quanta constants, so we have to find the value of A_o from the experience. To this aim we recall that between single Micro-quantum and Neutrino (Michelini, 2012) there is a relationship: both show a particular attitude of ignoring matter. The Micro-quanta flux is also involved in generating the mass of particles, as shown by the Inertial model. Low energy solar neutrinos show a little interaction with particles, differently from high energies neutrinos around 30-50 *Gev***.** Then I made the hypothesis that Neutrinos are *directional waves* constituted of very high number of Micro-quanta packaged without forming elementary charges in their interior. So they differ from the high energy γ-rays containing a rotating pair electron-positron.

In January 2012 at LNGS laboratories, the Borexino Experiment measured a very low *day-night* asymmetry in neutrino flux, that is a low interaction with matter of solar neutrinos observed at midnight, i.e. after travelling across the diameter of the Earth mass. (Borexino collaboration, 2912). The scattered neutrinos resulted a fraction around 0.001 of the total flux, showing a neutrino mean free path of the order $l \approx 10^3(2R) = 1.27 \times 10^{10}$. This result may be introduced in the formula of Micro-quanta paradigm

$$\boldsymbol{l} = 1/(A_o \delta_{m,}) \tag{4}$$

where δ_m is the average density of the tested mass. This equation is valid when the cross section of the exploring Quanta is negligible compared to the cross section σ_n of nucleons (as it happens for solar neutrinos). Solving for the unknown A_o one obtains $A_o = (\sigma_n / m_n) \approx 1.43 \times 10^{-14}$ for particles constituting the Earth mass, in practice nucleons. This ratio obtained by solar ^{7}Be neutrino measurements may be assumed also for micro-quanta.

Substituting in eq(3a) it appears that a second equation is necessary to obtains the distance x_o and the micro-quanta energy E_o. This require to write the equation of Quantum Pushing of gravitation.

5. *Origin of the Gravitational Pushing force*

Micro-quanta show very small energy E_o and wavelength λ_o of the order of the Planck's length $l_p = 4.05 \times 10^{-35}$, so they pertain to the class of physical objects introduced by micro-quanta and characterised by the second Planck's constant $h_o = E_o \lambda_o / c$. The energy E_o can be calculated assuning the *experimental* Gravitational force numerically equal to Newton's gravity $G m_n^2 / r^2$ adopting the *measured* G. This force is the Quantum *Pushing* gravity expressed in terms of Micro-quanta collisions on nucleons representing 99.95% of the masses

$$F_{gr} = (2E_o/c)(\phi_o \Delta\sigma)(\Delta\sigma/2\pi r^2) = p_o \Delta\sigma^2/\pi r^2 = G m_n^2 / r^2 \tag{5}$$

where $(2E_o/c)$ is the momentum released by each *recoiling* micro-quantum. The mutual shielding between particles reduces the quantum flux incident on the *shaded side* of each particle. For theoretical reasons the *central* tubular beam (cross section equal to $\Delta\sigma$), placed along the line joining the centres of two particles, shows *zero* quanta (*missing* beam). The beam $(\phi_o \Delta\sigma)(\Delta\sigma/2\pi r^2)$ is the real beam diametrically *opposite* to the *missing* beam, so the gravitational *Pushing* force drives any pair of facing particles. For the sake of simplicity, the total flux reduction on the *shaded* face may be concentrated on a central beam with a small area $\Delta\sigma$. So we have to calculate $\Delta\sigma$ in order to respect the *equivalence* with the actual shielding effect on the shaded side. Recalling eq(2a), the value

$\Delta\sigma = \sigma_t / N_t = x_o^2$ appears to depend on the characteristics of the flux, as expected.

Let's substitute $\Delta\sigma = x_o^2$ in eq(5) obtaining $(E_o \phi_o / c)\, x_o^4 = E_o x_o = \pi G m_n^2$, from which one obtains the equation

$$x_o E_o = 5.837\text{x}10^{-64} \quad \text{(Joule metre).} \tag{5a}$$

Rearranging eq(3a) and substituting eq(5a), one gets

$$A_o = c^2 x_o^2 / E_o = c^2 x_o^3 / 5.837\text{x}10^{-64}$$

which, adopting the experimental $A_o \approx 1.43\text{x}10^{-14}$ and solving respect to x_o, gives

$$x_o = (1.43\text{x}10^{-14}\,\text{x}\,5.837\text{x}10^{-64} / c^2)^{1/3} \approx 4.526\text{x}10^{-32} \quad \text{(metres.)} \tag{5b}$$

Notice that from this result we may correctly derive the flux

$$\phi_o = c / x_o^3 \approx 3.2347\text{x}10^{102} \qquad \text{(quanta / m}^2\text{ sec).}$$

At the same time from eq (5a) we obtain

$$E_o \approx 5.837\text{x}10^{-64} / x_o \approx 1.289\text{x}10^{-32} \quad \text{Joule.} \tag{5c}$$

These equations made firstly possible to express (Michelini, 2012) the gravitational constant G in terms of the constants of micro-quanta and nucleons constituting 99.95% of the ordinary mass

$$G = (E_o / \pi m_n^2)(c / \phi_o)^{1/3} \tag{5d}$$

showing that G vary slowly throughout the universe since the flux ϕ_o may undergo sensible increments in presence of concentrated large masses (dense stars, galactic nuclei, etc).

6. Analysis of Newton's Dynamical Law of Inertia

An unexpected support to the Micro-quanta paradigm came from the analysis of the Newton's Law of inertia which, after more than three centuries, works still well . Contrary to the classical pulling gravity whose "universal" constant G assumes the role of a statistical parameter. Newton's equation of dynamics $F_{in} = - m_i\, \Delta v/\Delta t$ assumes that the force *braking* the motion of some mass (accelerated by known forces) or *accelerating* the motion of another mass (braked by known forces) is *proportional* to the mass *acceleration*. To which reference system has the acceleration be considered? Newton showed courage in stating that inertial forces are only apparently generated by the "void" interplanetary space. Did he use the somewhat obscure locution "*absolute space*" to indicate some physical reality? Questioned on this point, he replayed correctly "*Hypotheses non fingo*". Does the accuracy of the incremental ratio $(\Delta v/\Delta t)$ requires more and more tight time intervals, as require mathematicians? We think not, because physical phenomena refer to objects having *always finite size*. In this case the time interval might be found through some experimental apparatus.

We believe that the "*absolute"* space hides *a physical* reality (Michelini M. 2016) that compels *free* bodies to travel in *strait line* (Principle of Inertia). In this case the physical reality can be a homogeneous flux of micro-quanta which *collide on particles,* but *do not practically collide* between them. The mean free path of micro-quanta in cosmic space due to their own cross section is enormous and equals the Hubble's radius $L_o = 1.3\text{x}10^{26}$. The Hubble's redshift is due to Compton' collisions of micro-quanta upon photons, so reducing their energy along their travel. This redshift happens *without any cosmic removal* of far galaxies (Michelini M. 2016).

Let's now consider a particle with velocity v under action of an accelerating force. The particle collides with beams of micro-quanta (having velocity c and the same direction), which hit *forward* and *behind* the cross section σ_t at any collision time statistically equal to $\tau_o = x_o/c$. So the accelerated particle shows, in the time τ_o, an increase of velocity Δv whose direction may be *different* from the velocity v, for instance in central motions where the Inertial force becomes the centrifugal force. The change of particle velocity Δv during the time τ_o gives the collision rates : *forwards* $R_f = \sigma_t\,(\phi_o/2)\,(c + \Delta v)/c$ and *behind* $R_b = \sigma_t\,(\phi_o/2)\,(c - \Delta v)/c$. The inertial force exerted by micro-quanta delivering on the average the momentum (E_o/c), is

$$F = (E_o/c)\,(R_b - R_f) = - \sigma_t\,(\phi_o E_o/c)\,(\Delta v/c) = - \sigma_t\, p_o\, (\Delta v/c). \tag{6}$$

Recalling the fundamental eq(1a) one has $\sigma_t = A_o m_i = (c / p_o \tau_o)\, m_i$ which, by substitution in eq(6), gives finally the Newton's Law of the inertial forces

$$F_{in} = - m_i \Delta v/\tau_o \tag{6a}$$

referred to the fundamental time interval $\tau_o = x_o/c = 1.508x10^{-40}$ sec. This shows that the *physical* origin of Newton's inertial force, acting upon an accelerating particle, depends on receiving *more* collisions on *forward* side than on *behind* side. Since the momentum released by each incident micro-quantum is the same on each side, the force unbalance depends on the different number of collision upon the two sides. This is confirmed by the Principle of Inertia stating that the *uniform strait motion* of a free particle continues indefinitely. In the language of micro-quanta this means that the flux upon particles at *uniform motion* is absolutely isotropic, that is the collision rate upon *forward* side equals that upon *behind* side. Concluding, Newton's inertial force depends on the *collision anisotropy* originated by the change Δv of particle velocity.

Speaking of acceleration respect to some *external* inertial system of reference (as stated by classical physics) is misleading because what matters is the *local generation* of the inertial force upon particles in accelerated motion directly "observed" by the micro-quanta.

Let's consider the new technology of Accelerometers, whose detector is contained within a strong black box, which transmits the accelerations due to accidents.by through the ratio between the *measured* inertial force and the test mass. Many types of detectors are used in terrestrial and spatial vehicles for recording shocks happened at any place of universe. No recourse to an inertial frame of reference is needed. Newton guessed the quantum character of the Law of inertia notwithstanding that Quantum concept were ignored at his time. On the contrary Newton failed in defining the Law of *pulling* gravitation because nature is capricious and hides the *Quantum pushing* gravity under the classical *pulling* gravity. Of course Newton didn't have at his disposal the concept of Quantum, which was attaint after more than two centuries, when Planck defined the quantum of light and Einstein gave the quantum explanation of the photovoltaic effect. It is worth noticing that the first introduction in 1748 of the *pushing* gravity concept (based on very small ultra-mundane corpuscules, due to George Louis Lesage) failed for the absence of Quantum concept.

References

Augustin, L., Barbante, C., Barnes, P. R., & Barnola, J. M. (2004). Eight glacial cycles from an Antarctic ice core. (Epica). *Nature*, *429*, 623-628

Bellini, G., Benziger, J., Bick, D., Bonetti, S., Bonfini, G., Avanzini, M. B., ... Cavalcante, P. (2012). Absence of a day–night asymmetry in the 7 Be solar neutrino rate in Borexino. *Physics Letters B*, *707*(1), 22-26.

Loinger, A. (2006). *Gravitational collapses to bodies of finite volume*. arXiv **:** physics//0612160

Michelini, M. (Jan. 2010). Major gravitational phenomena explained by the Micro-quanta paradigm. *Progress in Physics*, *1*, L19.

Michelini, M. (Nov. 2010). Physical Phenomena and Theoretical Problems Explained by the Micro-Quanta Paradigm. *Applied Physics Research*, *2*(2), 90.

Michelini, M. (2011). The Gravitational power originating the Earthquakes and the Dansgaard-Oeschger catastrophic Events. *Applied Physics Research*, *3*(1), 76.

Michelini, M. (2012). Beyond the Special and General Relativity Theories. *Applied Physics Research*, *4*(2), 210.

Michelini, M. (2016). Discussion on Fundamental Problems of Physics Hidden in Cosmology. *Applied Physics Research*, *8*(5), 19.

NIST Institute. (2014). *DATA 2014*. *Fundamental Physical constants.*

Petit, J. R., Jouzel, J., Raynaud, D., Barkov, N. I., Barnola, J. M., Basile, I., ... & Delmotte, M. (1999), Climate and atmospheric history of the past 420,000 years from the Vostok ice core, Antarctica. *Nature*, *399*(6735), 429-436.

Rahmstorf, S. (2003). Timing of abrupt climate change: A precise clock. *Geophysical Research Letters*, *30*(10).

Stuiver, M., & Grootes, P. M. (2000). GISP2 oxygen isotope ratios. *Quaternary Research*, *53*(3), 277-284.

Copyrights

Applied Physics Research; Vol. 9, No. 6; 2017
ISSN 1916-9639 E-ISSN 1916-9647
Published by Canadian Center of Science and Education

Solution of a Spherically Symmetric Static Problem of General Relativity for an Elastic Solid Sphere

Valery V. Vasiliev[1] & Leonid V. Fedorov[1]

[1] Institute of Problems in Mechanics , Russian Academy of Sciences, 101 Vernadskogo, Moscow 119526, Russia

Correspondence: Valery V. Vasiliev, Institute of Problems in Mechanics, Russian Academy of Sciences, 101 Vernadskogo, Moscow 119526, Russia. Tel: 7-916-607-1281. E-mail: vvvas@dol.ru

Received: September 12, 2017 Accepted: September 22, 2017 Online Published: October 19, 2017

doi:10.5539/apr.v9n6p8 URL: https://doi.org/10.5539/apr.v9n6p8

Abstract

The paper is concerned with the spherically symmetric static problem of the General Relativity Theory (GRT). The classical interior solution of this problem found in 1916 by K. Schwarzschild for a fluid sphere is generalized for a linear elastic isotropic solid sphere. The GRT equations are supplemented with the equation for the stresses which is similar to the compatibility equation of the theory of elasticity and is derived using the principle of minimum complementary energy for an elastic solid. Numerical analysis of the obtained solution is undertaken.

Keywords: general relativity theory, theory of elasticity, spherically symmetric static problem

1. Introduction. Theory of Elasticity Solution

To introduce the proposed approach to GRT problem for elastic solid, consider the problem of the classical theory of elasticity for a sphere whose gravitational field is described by the Newton theory. For a solid sphere with constant density μ and radius R, the Newton gravitational potential ϕ is the solution of the Poisson equation

$$\frac{1}{r^2}\left(r^2\phi'\right)' = 4\pi G\mu \tag{1}$$

Here, r is the radial coordinate $(0 \le r \le R)$, $(\cdots)' = d(\cdots)/dr$ and G is the classical gravitational constant. For the external $(r \ge R)$ space, $\mu = 0$ and Equation (1) has the following well known solution:

$$\phi_e = -\frac{Gm}{r} \tag{2}$$

Where index "*e*" corresponds to the external space and

$$m = \frac{4}{3}\pi\mu R^3 \tag{3}$$

is the mass of a homogeneous solid sphere whose internal space is Euclidean. For the internal $(0 \le r \le R)$ space the solution of Equation (1) which satisfies the regularity condition at the sphere center is

$$\phi_i = \frac{2}{3}\pi\mu G r^2 + C_1 \tag{4}$$

Here, index "*i*" corresponds to the internal space. The integration constant C_1 is determined from the boundary condition on the sphere surface according to which $\phi_e(R) = \phi_i(R)$. Using Equation (2), we can present Equation (4) in the following final form:

$$\phi_i = -\frac{Gm}{2R}\left(3 - \frac{r^2}{R^2}\right) \tag{5}$$

The gravitational body forces which act inside the sphere are

$$f_g = -\mu\phi_i' = -kr\,, \qquad k = \frac{4}{3}\pi G\mu^2 \tag{6}$$

Then, the theory of elasticity equilibrium equation for the sphere element can be presented as

$$r\sigma_r' + 2(\sigma_r - \sigma_\theta) - kr^2 = 0 \tag{7}$$

Here, σ_r and σ_θ are the radial and the circumferential stresses which are accompanied by the corresponding elastic strains following from Hooke's law, i.e.

$$\varepsilon_r = \frac{1}{E}(\sigma_r - 2\nu\sigma_\theta), \qquad \varepsilon_\theta = \frac{1}{E}\left[(1-\nu)\sigma_\theta - \nu\sigma_r\right] \tag{8}$$

in which E and ν are the elastic modulus and the Poisson's ratio of the sphere material. The strains are expressed in terms of the radial displacement u as

$$\varepsilon_r = u', \qquad \varepsilon_\theta = u/r \tag{9}$$

Substituting u from the second of these equations in the first one, we arrive at the following compatibility equation for the strains:

$$r\varepsilon_\theta' + \varepsilon_\theta - \varepsilon_r = 0$$

Using Equations (7), we can write this equation in terms of stresses, i.e.

$$r(1-\nu)\sigma_\theta' - r\nu\sigma_r' + (1-\nu)(\sigma_\theta - \sigma_r) = 0 \tag{10}$$

Thus, we have two equations, Equations (7) and (10), for two unknown stresses. To reduce these equations to one equation with respect to the radial stress, express σ_θ using Equation (7), i.e.

$$\sigma_\theta = \sigma_r + \frac{r}{2}(\sigma_r' - kr) \tag{11}$$

and substitute it in Equation (10) to get

$$r\sigma_r'' + 4\sigma_r' - \frac{3-\nu}{1-\nu}kr = 0 \tag{12}$$

The solution of this equation must satisfy the following boundary conditions:

$$\sigma_r(r=0) = \sigma_\theta(r=0), \qquad \sigma_r(r=R) = 0 \tag{13}$$

Using Equation (11), we can transform the first of these conditions to $\sigma_r'(r=0) = 0$. The final solution for the stresses is

$$\sigma_r = -\frac{(3-\nu)k}{10(1-\nu)}\left(R^2 - r^2\right), \qquad \sigma_\theta = -\frac{(3-\nu)k}{10(1-\nu)}\left(R^2 - \frac{1+\nu}{3-\nu}r^2\right) \tag{14}$$

Having in mind to obtain the solution of the problem under study within the framework of GTR, we should take into account the GRT equations are formulated in the Riemannian space in which the displacement u, as well as the strain-displacement equations, Equations (9), do not exist. Thus, we cannot derive the compatibility equation, Equation (10) using the traditional approach. However, theory of elasticity provides another way to obtain this equation not attracting Equations (9). As known, the compatibility equation formulated in stresses follows from the principle of minimum of the complementary energy under the condition that the stresses satisfy the equilibrium equations. The elastic energy of the solid sphere is

$$U = 4\pi\int_0^R wr^2 dr \tag{15}$$

where

$$w = \frac{1}{2}(\sigma_r\varepsilon_r + 2\sigma_\theta\varepsilon_\theta)$$

is the elastic potential. Substituting the strains from Hooke's law, Equations (8), in Equation (15), expressing σ_θ in terms of σ_r with the aid of Equation (11) and thus satisfying the equilibrium equation, we can reduce the complementary energy to the following functional:

$$U = \frac{2\pi}{E}\int_0^R F(r, \sigma_r, \sigma_r')dr \tag{16}$$

where

$$F=(1-2\nu)(3\sigma_r^2+2r\sigma_r\sigma_r'-2kr^2\sigma_r)r^2+\frac{1-\nu}{2}\left[(\sigma_r')^2-2kr\sigma_r'+k^2\right]r^4 \tag{17}$$

The Euler equation which provides the minimum value of the complementary energy is

$$\frac{\partial F}{\partial \sigma_r}-\frac{d}{dr}\left(\frac{\partial F}{\partial \sigma_r'}\right)=0 \tag{18}$$

Substituting F from Equation (17), we arrive at the compatibility equation, Equation (12).

In conclusion, transform the obtained results introducing the following dimensionless parameters:

$$\bar{\sigma}=\frac{\sigma}{\mu c^2},\qquad \bar{r}=\frac{r}{R},\qquad \bar{r}_g=\frac{r_g}{R} \tag{19}$$

Here, c is the velocity of light and

$$r_g=\frac{2mG}{c^2} \tag{20}$$

is the so-called gravitational radius. Using Equations (3) and (6) for m and k and applying Equations (19), we can present the compatibility equation, Equation (12) in the following form:

$$\bar{r}\frac{d^2\bar{\sigma}_r}{d\bar{r}^2}+4\frac{d\bar{\sigma}_r}{d\bar{r}}=\frac{(3-\nu)\bar{r}_g\bar{r}}{2(1-\nu)} \tag{21}$$

The normalized stresses become

$$\bar{\sigma}_r=-\frac{(3-\nu)\bar{r}_g}{20(1-\nu)}(1-\bar{r}^2),\qquad \bar{\sigma}_\theta=-\frac{(3-\nu)r_g}{20(1-\nu)}\left(1-\frac{1+\nu}{3-\nu}\bar{r}^2\right) \tag{22}$$

2. Spherically Symmetric Static Problem of General Relativity for an Elastic Sphere

For a spherically symmetric static problem, the line element is traditionally taken in the following form corresponding to the classical Schwarzchild solution:

$$ds^2=g_{11}dr^2+r^2(d\theta^2+\sin^2\theta d\phi^2)-g_{44}c^2dt^2 \tag{23}$$

Here r,θ,ϕ and t are space spherical and time coordinates, g_{ij} are the metric coefficients that depend on the radial coordinate r only. For the spherically symmetric static problem and the line element in Equation (23), the conservation equation which is analogous to the equilibrium equation, Equation (7) of the theory of elasticity, is (Synge, 1960)

$$\sigma_r'-\frac{2}{r}(\sigma_\theta-\sigma_r)+\frac{g_{44}'}{2g_{44}}(\sigma_r-\mu c^2)=0 \tag{24}$$

Here, the stresses and the density are expressed in terms of the metric coefficients with aid of Einstein's equations which can be presented as (Synge, 1960)

$$\chi\sigma_r=\frac{1}{r^2}-\frac{1}{rg_{11}}\left(\frac{g_{44}'}{g_{44}}+\frac{1}{r}\right) \tag{25}$$

$$\chi\sigma_\theta=-\frac{1}{2g_{11}}\left[\frac{g_{44}''}{g_{44}}-\frac{1}{2}\left(\frac{g_{44}'}{g_{44}}\right)^2+\frac{1}{r}\left(\frac{g_{44}'}{g_{44}}-\frac{g_{11}'}{g_{11}}\right)-\frac{g_{11}'g_{44}'}{2g_{11}g_{44}}\right] \tag{26}$$

$$\chi\mu c^2=\frac{1}{r^2}-\frac{1}{rg_{11}}\left(\frac{1}{r}-\frac{g_{11}'}{g_{11}}\right) \tag{27}$$

where

$$\chi=8\pi G/c^4 \tag{28}$$

is the GRT gravitational constant. As known, substitution of Equations (25)-(27) in Equation (24) identically satisfies this equation.

Perform some transformations. First, consider Equation (27). The solutions of this equation for the external $(r \geq R, \mu = 0)$ and internal $(0 \leq r \leq R, \mu = const)$ spaces are specified by the well known exterior and interior Schwarzchild solutions which have the form (Synge, 1960)

$$g_{11}^{e} = \frac{1}{1 - r_g / r}, \qquad g_{11}^{i} = \frac{1}{1 - r_g r^2 / R^3} \tag{29}$$

Here, indices "e " and "i" correspond to external and internal spaces, whereas r_g is the gravitational radius specified by Equation (20). Second, introduce function $f(r)$ as

$$\frac{g_{44}'}{g_{44}} = f, \qquad \frac{g_{44}''}{g_{44}} = f' + f^2 \tag{30}$$

Finally, substituting the second of Equations (29) and Equations (30) in Equations (25) and (26), we arrive at

$$\chi\sigma_r = \frac{r_g}{R^3} - \left(\frac{1}{r} - \frac{r_g r}{R^3}\right) f \tag{31}$$

$$\chi\sigma_\theta = \frac{r_g}{R^3} - \frac{1}{2}\left(1 - \frac{r_g r^2}{R^3}\right)\left(f' + \frac{f^2}{2}\right) - \left(\frac{1}{2r} - \frac{r_g r}{R^3}\right) f \tag{32}$$

Following the approach described in Section 1, express f in terms of σ_r using Equation (31)

$$f = \frac{r}{1 - r_g r^2 / R^3}\left(\frac{r_g}{R^3} - \chi\sigma_r\right)$$

and substitute this result in Equation (32), i.e.

$$\sigma_\theta = \frac{1}{4(1 - r_g r^2 / R^3)}\left[2r\left(1 - \frac{r_g r^2}{R^3}\right)\sigma_r' + 4\sigma_r - \chi r^2 \sigma_r^2 - \frac{3 r_g^2 r^2}{R^6 \chi}\right] \tag{33}$$

According to the basic idea of GRT, the stresses specified by the Einstein equations, Equations (31) and (32), identically satisfy the equilibrium equation, Equation (24). Transforming this equation with the aid of Equations (3), (20) and (28) for m, r_g, χ and substituting σ_θ from Equation (33), we can readily prove that the equilibrium equation is satisfied. Thus, to determine σ_r, we can apply the principle of minimum of the complementary energy discussed in Section 1. In the Riemannian space, Equation (15) for the complementary energy is generalized as

$$U = 4\pi \int_0^R w \sqrt{g_{11}}\, r^2 dr$$

Using Equation (32), we can reduce it to the functional in Equation (16). Omitting the explicit expression for the function F which is rather cumbersome, present the Euler equation, Equation (18), which takes the following final form:

$$2\bar{r}(1-\nu)(1-\bar{r}_g\bar{r}^2)^2 \frac{d^2\bar{\sigma}_r}{d\bar{r}^2} + 2(1-\nu)(1-\bar{r}_g\bar{r}^2)(4-3\bar{r}_g\bar{r}^2)\frac{d\bar{\sigma}_r}{d\bar{r}} + \bar{r}_g\bar{r}\left[4(2+\nu) - \bar{r}_g\bar{r}^2(7+5\nu)\right]\bar{\sigma}_r$$

$$+3\bar{r}_g\bar{r}\left[1 - 7\nu + 2\bar{r}_g\bar{r}^2(1+2\nu)\right]\bar{\sigma}_r^2 - 9\bar{r}_g^2\bar{r}^3(1-\nu)\bar{\sigma}_r^3 - \bar{r}_g\bar{r}(3 - \nu - 2\bar{r}_g\bar{r}^2) = 0 \tag{34}$$

To simplify this equation, we use dimensionless parameters in Equations (19) and Equations(3), (21) and (28) for m, r_g and χ. Neglecting the terms with $\bar{r}_g$ in comparison with unity and omitting nonlinear terms, we arrive at equation (21) of the theory of elasticity.

3. Numerical Analysis

For the numerical analysis, we take $\nu = 0$ and reduce Equation (34) to

$$2\bar{r}(1-\bar{r}_g\bar{r}^2)^2\frac{d^2\bar{\sigma}_r}{d\bar{r}^2}+2(1-\bar{r}_g\bar{r}^2)(4-3\bar{r}_g\bar{r}^2)\frac{d\bar{\sigma}_r}{d\bar{r}}+\bar{r}_g\bar{r}(8-7\bar{r}_g\bar{r}^2)\bar{\sigma}_r+3\bar{r}_g\bar{r}(1+2\bar{r}_g\bar{r}^2)\bar{\sigma}_r^2$$

$$-9\bar{r}_g^2\bar{r}^3\bar{\sigma}_r^3=\bar{r}_g\bar{r}(3-2\bar{r}_g\bar{r}^2) \tag{35}$$

This equation is numerically integrated under the boundary conditions that follow from Equations (13), i.e. $\bar{\sigma}_r'(\bar{r}=0)=0$ and $\bar{\sigma}_r(\bar{r}=1)=0$. The circumferential stress is found from Equation (33) which can be transformed to

$$\bar{\sigma}_\theta=\frac{1}{4(1-\bar{r}_g\bar{r}^2)}\left[2\bar{r}(1-\bar{r}_g\bar{r}^2)\frac{d\bar{\sigma}_r}{d\bar{r}}+4\bar{\sigma}_r-3\bar{r}_g\bar{r}^2\bar{\sigma}_r^2-\bar{r}_g\bar{r}^2\right] \tag{36}$$

It is interesting to compare the results that follow from Equations (35) and (36) with the theory of elasticity solution specified by Equations (22) and with the interior Schwarzchild solution obtained for a sphere of perfect incompressible fluid. This solution has the following form (Synge, 1960):

$$\bar{p}=\frac{p}{\mu c^2}=-\frac{\sqrt{1-\bar{r}_g\bar{r}^2}-\sqrt{1-\bar{r}_g}}{\sqrt{1-\bar{r}_g\bar{r}^2}-3\sqrt{1-\bar{r}_g}} \tag{37}$$

and demonstrates a specific behavior. Taking $\bar{r}=0$ in Equation (37), determine the pressure at the sphere center, i.e.

$$\bar{p}_0=-\frac{1-\sqrt{1-\bar{r}_g}}{1-3\sqrt{1-\bar{r}_g}} \tag{38}$$

The denominator of this expression is zero for the sphere with radius $\bar{r}_g=8/9=0.8888,$ and the pressure becomes infinitely high at the sphere center. This result is sometimes used to support the existence of the objects referred to as the Black Holes (Thorne, 1994).

The results of the numerical analysis are presented in Figures 1, 2. Figure 1 demonstrates the distributions of the normalized radial (solid lines) and circumferential (dashed lines) stresses over the radial coordinate for $\bar{r}_g=0.2,0.4,0.6,0.8,0.99.$

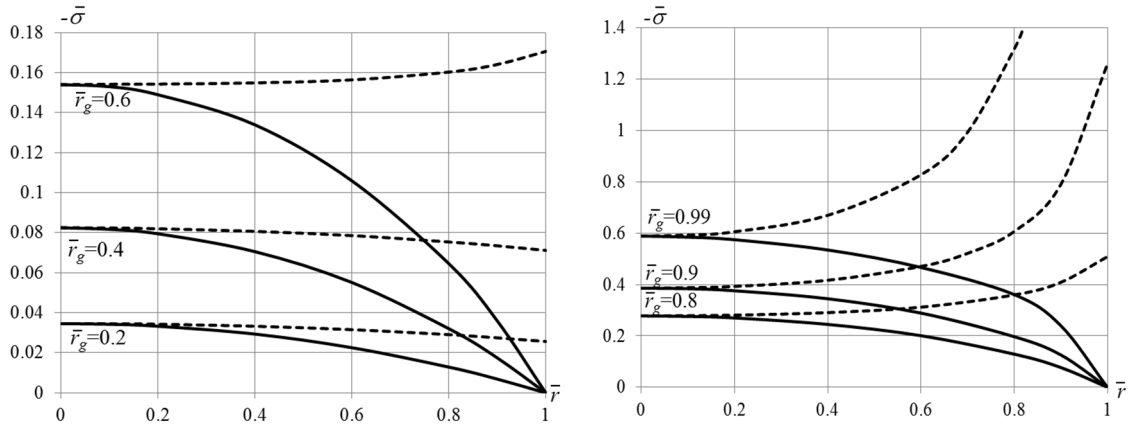

(a) (b)

Figure 1. Distributions of the normalized radial (solid lines) and circumferential (dashed lines) stresses over the radial coordinate for (a) $\bar{r}_g=0.2,0.4,0.6$ and (b) $\bar{r}_g 0.8,0.9,0.99$

Figure 2 shows the normalized stresses at the sphere center as functions of the normalized gravitational radius.

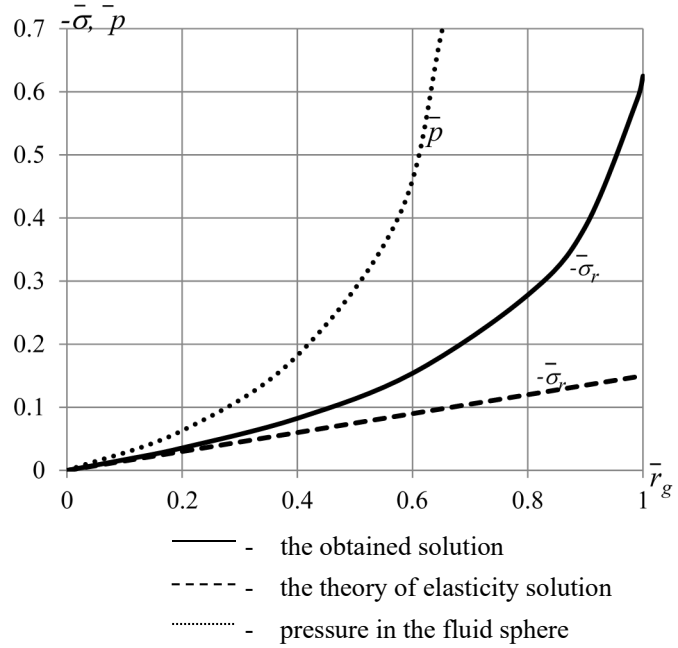

Figure 2. Dependences of the normalized stresses at the sphere center on the radial coordinate

As can be seen, in contrast to the pressure specified by Equation (38) which becomes infinitely high at $\bar{r}_g = 8/9$, the stresses are finite for the sphere with the radius $R = 9/8r_g$. For $\bar{r}_g = 1$, the numerical solution does not converge. However, it does not look like the stresses are singular in this case. It seems that the tolerance of the applied numerical procedure is not as high as should be. The last result $\bar{\sigma} = -0.5886$ is obtained for $\bar{r}_g = 0.99$. Dashed line in Figure 2 corresponds to the theory of elasticity solution specified by Equations (22).

4. Conclusion

The solution of the Schwarzchild spherically symmetric static problem for a fluid sphere is generalized for a linear elastic sphere. The equation for the stresses missing in GRT is derived using the minimum complementary energy principle of the theory of elasticity. In contrast to the singular Schwarzchild solution for the pressure in the fluid, the stresses do not demonstrate singular behavior for the elastic sphere whose radius is equal to the gravitational radius.

References

Synge, J. L. (1960). *Relativity: the General Theory.* Amsterdam, North Holland.

Thorn, K. S. (1994). *Black Holes and Time Warps – Einstein's Outrages Legacy.* New York, London, W.W. Norton and Company.

Copyrights

Applied Physics Research; Vol. 9, No. 6; 2017
ISSN 1916-9639 E-ISSN 1916-9647
Published by Canadian Center of Science and Education

The Dark Matter and Dark Energy in Cosmic Evolution

Bin Liang[1]

[1] College of Science, Chongqing University of Posts and Telecommunication, Chongqing 400065, China

Correspondence: Bin Liang, College of Science, Chongqing University of Posts and Telecommunication, Chongqing 400065, China. E-mail: liangbin@cqupt.edu.cn

Received: October 21, 2017 Accepted: October 29, 2017 Online Published: November 1, 2017

doi:10.5539/apr.v9n6p14 URL: https://doi.org/10.5539/apr.v9n6p14

Abstract

This article is on an in-depth study of the relationship between the dark matter, dark energy, radiation field and gravitation field, based on the standard cosmic model and the principle that dark energy is originated from the destructive interference of electromagnetic radiation field. It explains the dynamic mechanism of cosmic expansion and contraction, and calculates the densities of dark matter, dark energy, radiation field and gravitation field.

Keywords: Gravitation field, radiation field, dark matter, dark energy, cosmic expansion and contraction

1. Introduction

In Liang (2015) we proved that the dark energy is originated from the destructive interference of electromagnetic radiation field, and that the increase of dark energy makes the universe expand. At the same time, the energy level of matter reduces, more and more matter becomes the dark matter with the dissipation of electromagnetic radiation field. The universe stops expanding and starts to contract in the action of gravity when the energy density of radiation field becomes small enough.

But the paper does not directly involve Einstein's equation of gravitational field. And this article will deeply study the relationship between dark matter, dark energy, radiation field and gravitation field, explain the dynamic mechanism of cosmic expansion and contraction, and calculate the densities of dark matter, dark energy, radiation field and gravitation field.

For ease of discussion, we need firstly to emphasize two basic concepts of the standard cosmic model: (1) the gravitational source is the massive matter and includes the dark matter; (2) the cosmic space is a finite space without boundary with the curvature $k = 1$.

We know that Einstein's equation of gravitational field (Weinberg, 1972) is

$$R_{\mu\nu} = -8\pi G\left(T_{\mu\nu} - \frac{1}{2}g_{\mu\nu}T\right), \tag{1}$$

it degenerates into Newton's gravitational equation on the condition of static weak field, and Newton's gravitational equation is one about the massive matter, so, the pressure p and density ρ in the energy-momentum tensor

$$T_{\mu\nu} = pg_{\mu\nu} + (\rho + p)U_{\mu}U_{\nu} \tag{2}$$

should be the pressure and density of the massive matter, and they are functions of the cosmic time t.

The massive matter could be divided into two classes: visible matter and dark matter. Visible matter radiates the electromagnetic wave, and dark matter does not, like neutrinos and other massive particles in the quantum ground state. So

$$\rho = \rho_m + \rho_{Dm}, \tag{3}$$

where ρ_m is the mass density of visible matter, ρ_{Dm} is that of dark matter.

Using Robertson-Walker metric (Weinberg, 1972)

$$d\tau^2 = dt^2 - R^2(t)\left[\frac{dr^2}{1-kr^2} + r^2 d\theta^2 + r^2 \sin^2\theta d\varphi^2\right] \quad (4)$$

and Einstein's equation of gravitational field gives

$$3\ddot{R} = -4\pi G(\rho + 3\mathrm{p})R\,, \quad (5)$$

and

$$R\ddot{R} + 2\dot{R}^2 + 2k = 4\pi G(\rho - \mathrm{p})R^2\,. \quad (6)$$

Eliminating $\ddot{R}$ from the two equations above gives the Friedmann equation:

$$\dot{R}^2 + \mathrm{k} = \frac{8\pi G}{3}\rho R^2\,. \quad (7)$$

Suppose there is $\dot{R} = 0$ at some moment t_0, then

$$\mathrm{k} = \frac{8\pi G}{3}\rho(t_0)R^2(t_0) > 0\,. \quad (8)$$

Since the curvature k is a constant, the equation above shows that it is impossible the curvature k equals 0 or -1. And since there is $\mathrm{k} = 1$ for $\rho R^2 = 3/8\pi G$, so the cosmic space is a finite space without boundary with the curvature $\mathrm{k} = 1$, and this means the universe experiences the lengthy expansion after the initial big bang, and then will experience a lengthy contraction and brew the next big bang, as is usually understood.

2. Dark Matter Density

The Friedmann equation (7) could be rewritten as

$$\rho = \frac{3}{8\pi G}\left(\mathrm{H}^2 + \frac{\mathrm{k}}{R^2}\right), \quad (9)$$

where the Hubble constant $H \equiv \dot{R}/R$. Substituting the equation above into equation (6) gives

$$p = -\frac{1}{3}\rho + \frac{2}{3}q_0\rho_c\,, \quad (10)$$

where

$$\rho_c = \frac{3H^2}{8\pi G} \quad (11)$$

is usually called the critical mass density, and

$$q_0 \equiv -R\ddot{R}/\dot{R}^2 \quad (12)$$

is called the deceleration parameter. Substituting the present Hubble constant (Hinshaw et al., 2009) $H_0 = 74.3 km/(s \cdot Mpc)$ into equation (11) gives

$$\rho_c = \frac{3H_0^{\,2}}{8\pi G} = 1.1\times 10^{-26} kg/m^3\,. \quad (13)$$

Suppose the matter in the gravitational source is non-relativistic, the pressure $p \ll \rho$, take $q_0 \approx 1$, the equation (10) gives

$$\rho = 2\rho_c\,. \quad (14)$$

According to the astronomical observation (Weinberg, 1972), the mass density in a galaxy, i.e. that of visible matter

$$\rho_m = 0.028\rho_c\,, \quad (15)$$

so, the equation above and equation (3) give the mass density of dark matter:

$$\rho_{Dm} = 1.972\rho_c \gg \rho_m\,. \quad (16)$$

The most direct evidence of existence of dark matter is the measurement of rotation speed of vortex galaxy (Li & Xiao, 2000). Suppose the matter density is $\rho(\mathrm{r}) \approx B\frac{\rho_{Dm}}{r^2}$ due to the gravitation in a vortex galaxy, where r is the radius from the galaxy center, and B is an undetermined constant，so the mass within the scope of r is

$$M(r)=\int_0^r \rho(r)4\pi r^2 dr = 4\pi\rho_{Dm}Br\ , \tag{17}$$

and the rotation speed of the star at position r is a constant independent of r:

$$\upsilon(r)=\sqrt{G\frac{M(\mathrm{r})}{r}}=\sqrt{4\pi GB\rho_{Dm}}\ . \tag{18}$$

This is in line with astronomical observation and provides a way to determine the constant B. For example, if $\upsilon = 150km/s$ (Weinberg, 1972) then there is

$$B=\frac{\upsilon^2}{4\pi G\rho_{Dm}}=1.24\times10^{45}/m\ . \tag{19}$$

3. Dark Energy Density

In the standard cosmic model the energy conservation equation is (Weinberg, 1972)

$$\dot{p}R^3=\frac{d}{dt}\left[R^3(\rho+p)\right], \tag{20}$$

i.e.

$$\dot{\rho}=-3(\rho+p)\frac{\dot{R}}{R}\ . \tag{21}$$

This shows that the source density decreases with cosmic expansion and increases with cosmic contraction. However, the equation above is obtained on the condition that galaxies neither are created nor disappear (Weinberg, 1972), and the actual situation is different.

In the cosmic lengthy evolution, the total energy should be conserved, although various kinds of energy wane and wax. At any time, if the universe doesn't expands, there should be

$$\frac{d}{dt}(\rho+\rho_e+\rho_G+\rho_d)=0\ , \tag{22}$$

where ρ is the energy density of the gravitational source as mentioned before, ρ_G is the energy density of the gravitational field, and ρ_d is the dark energy density. Since the radiation field in the cosmic evolution is equivalent to the blackbody radiation field (Weinberg, 1972), the energy density of radiation field is $\rho_e = 4\sigma T^4/c$.

Without dissipation of the radiation field translating into dark energy due to destructive interference, radiation and absorption of electromagnetic waves is a conservative process, and $\frac{d}{d}(\rho+\rho_e)=0$. But because of the dissipation process of the radiation field translating into dark energy, there is

$$\frac{d}{d}(\rho+\rho_e)=-\eta\rho_e\ , \tag{23}$$

where η is the conversion rate from radiation field into dark energy per unit time (Liang, 2015).

Substituting the equation (23) into the equation (22) gives

$$\eta\rho_e=\frac{d\rho_d}{dt}+\frac{d\rho_G}{dt}\ . \tag{24}$$

This shows that a part of the dissipated energy of radiation field is translated into the dark energy and other is translated into the gravitational field.

Writing $f\equiv\frac{d\rho_G}{dt}$, the equation above can be rewritten as

$$\frac{d\rho_d}{dt} = \eta\rho_e - f\,, \tag{25}$$

This is the equation (8) in the Liang (2015), but derived in a different way here.

Using $H \equiv \dot{R}/R$ the equation (11) in the paper can be rewritten as

$$\frac{1}{R}\frac{\mathrm{d}R}{\mathrm{d}t} = \frac{1}{\rho_d}\frac{\mathrm{d}\rho_d}{\mathrm{d}t}\,. \tag{26}$$

The two equations above show that when $\eta\rho_e > f$, dark energy increases and the universe expands; when $\eta\rho_e < f$, dark energy decreases and the universe contracts. This is the dynamical mechanism of cosmic expansion and contraction. From the equation above we know

$$\rho_d = c_d R\,, \tag{27}$$

where the proportional constant c_d is determined by the latter equation (35).

4. The Conversion Rate of Radiation Field and the Proportion of Dark Matter

As shown in equation (3), the source of gravitational field includes visible and dark matter. On the cosmic time-space background, we can consider that the increase of dark matter equals the decrease of visible matter:

$$\frac{d\rho_{Dm}}{dt} = -\frac{d\rho_m}{dt}\,. \tag{28}$$

Substituting the equation above and equation (3) into equation (23) gives

$$\frac{d\rho_e}{d} = -\eta\rho_e\,. \tag{29}$$

Suppose the conversion rate η is a constant independent of time and integrating the equation above gives

$$\eta = \frac{1}{\Delta t}\ln\left(\frac{\rho_e(t_0)}{\rho_e(t)}\right), \tag{30}$$

where $\Delta t \equiv t - t_0 > 0$. Substituting $\rho_e = 4\sigma T^4/c$ into the equation above gives

$$\eta = \frac{4}{\Delta t}\ln\left(\frac{T(t_0)}{T(t)}\right). \tag{31}$$

For instance, if $T(t_0) = 4000K$ (Weinberg, 1972), $T(t) = 2.73K$, $\Delta t = 131.348\times10^8\,y$, then

$$\eta = 2.52\times10^{-9}/\,y = 0.7984\times10^{-16}/\,s\,. \tag{32}$$

The reason why the value above is different from that in Liang (2015) is that the calculation cited the equation $\rho_d = 0.683\rho_c c^2$ in the paper, but the equation is inaccurate.

As shown in equation (18), the rotation speed υ of a star at the position r in a vortex galaxy is a constant independent of r, so the pressure of gravitation force is

$$\rho_{Dm}\frac{\upsilon^2}{r}\,, \tag{33}$$

and the work of dark energy to resist the gravitation force per unit time, i.e. the rate of change of gravitational energy is

$$f = \frac{d\rho_G}{dt} = \rho_{Dm}\frac{\upsilon^2}{R}\dot{R} = \rho_{Dm}\upsilon^2 H\,. \tag{34}$$

Substituting the equation above and equation (27) into equation (25) gives

$$c_d = \frac{1}{\dot{R}}\left(\eta\rho_e - \rho_{Dm}\upsilon^2 H\right). \tag{35}$$

Thus the density of dark energy can be written as

$$\rho_d = \frac{\eta\rho_e}{H} - \rho_{Dm}v^2 . \quad (36)$$

The present density of dark energy is

$$\rho_d = \frac{\eta\rho_e}{H_0} - \rho_{Dm}v^2 \approx \frac{\eta\rho_e}{H_0} = 1.42\times10^{-12} J/m^3 = 1.43\times10^{-3}\rho_c c^2 . \quad (37)$$

where $\rho_e = 4.28\times10^{-14} J/m^3 = 4.32\times10^{-5}\rho_c c^2$.

If we define the energy density of gravitational field as

$$\rho_G \equiv \rho_{Dm}v^2 = 4.61\times10^{-16} J/m^3 = 4.95\times10^{-7}\rho_c c^2 , \quad (38)$$

from the three equations above we know that that ρ_d, ρ_e and ρ_G are negligible, and the total energy density of the universe can be written approximately as

$$\rho_0 \approx \rho_m + \rho_{Dm} \approx 2\rho_c . \quad (39)$$

So there is

$$\Omega_m + \Omega_{Dm} \approx 1 , \quad (40)$$

where

$$\Omega_m = \rho_m / \rho_0 \approx 1.4\%,$$
$$\Omega_{Dm} = \rho_{Dm} / \rho_0 \approx 98.6\%. \quad (41)$$

Obviously, the density of dark matter is far greater than that of visible matter in the present universe.

Reference

Bartelmann, M. (2010). The dark universe. *Reviews of Modern Physics*, *82*(1), 331-382.

Bennett, C. L., Larson, D., Weiland, J. L., Jarosik, N., Hinshaw, G., Odegard, N., ... & Komatsu, E. (2013). Nine-year Wilkinson Microwave Anisotropy Probe (WMAP) observations: final maps and results. *The Astrophysical Journal Supplement Series*, *208*(2), 20. http://dx.doi.org/10.1088/0067-0049/208/2/20

Friedman, A. (1999). On the curvature of space. *General Relativity and Gravitation*, *31*(12), 1991-2000. http://dx.doi.org/10.1007/BF01332580

Hinshaw, G., Weiland, J. L., Hill, R. S., Odegard, N., Larson, D., Bennett, C. L., ... & Komatsu, E. (2009). Five-year wilkinson microwave anisotropy probe* Observations: data processing, sky maps, and basic results. *The Astrophysical Journal Supplement Series*, *180*(2), 225.

Li, Z. W., & Xiao, X. H. (2000). *Astrophysics*. Beijing: Higher Education Press.

Liang, B. (2015). The Origin of Dark Energy and Cosmic Expansion and Contraction. *Applied Physics Research*, *7*(6), 134.

Peacock, J. A. (1999). *Cosmological Physics*. Cambridge: Cambridge University Press.

Peebles, P. J. E., & Ratra, B. (2003). The cosmological constant and dark energy. *Reviews of modern physics*, *75*(2), 559-606.

Perlmutter, S., Aldering, G., Goldhaber, G., Knop, R. A., Nugent, P., Castro, P. G., ... & Hook, I. M. (1999). Measurements of Ω and Λ from 42 high-redshift supernovae. *The Astrophysical Journal*, *517*(2), 565-586. http://dx.doi.org/10.1086/307221

Riess, A. G., Filippenko, A. V., Challis, P., Clocchiatti, A., Diercks, A., Garnavich, P. M., ... & Leibundgut, B. R. U. N. O. (1998). Observational evidence from supernovae for an accelerating universe and a cosmological constant. *The Astronomical Journal*, *116*(3), 1009-1038. http://dx.doi.org/10.1086/300499

Weinberg, S. (2008). *Cosmology*. New York: Oxford University Press.

Weinberg, S. (1972). Gravitation and cosmology. *John Wiley and Sons, New York*.

Applied Physics Research; Vol. 9, No. 6; 2017
ISSN 1916-9639 E-ISSN 1916-9647
Published by Canadian Center of Science and Education

Rapid Laser Direct Writing of Plasmonic Components

G. Amoako[1,2], W. Zhang[1], M. Zhou[1], S. S. Sackey[2] & P. Mensah-Amoah[2]

1. Center for Photon Manufacturing Science and Technology, Jiangsu University, Zhenjiang, Jiangsu, P. R. China

2. Department of Physics, University of Cape Coast, Cape Coast, Ghana

Correspondence: G. Amoako, Center for Photon Manufacturing Science and Technology, Jiangsu University, Zhenjiang, Jiangsu, 212013, P. R. China. Tel: 233-505-300-062. E-mail: gamoako@ucc.edu.gh

Received: October 21, 2017 Accepted: October 29, 2017 Online Published: November 7, 2017

doi:10.5539/apr.v9n6p19 URL: https://doi.org/10.5539/apr.v9n6p19

Abstract

A new device named technology-plasmonics has recently emerged and can be used to manipulate light at the nano-scale level. Here, we report the method of two-photon photopolymerization for rapid laser direct writing of plasmonic components. The characterization of these components is performed by a leakage radiation microscope, which has the same system construction as the two-photon photopolymerization micro-fabrication system except the laser pattern. The dielectric structures covered with gold proved to be very efficient for the excitation of surface plasmon polaritons in this system and can achieve different plasmon fields.

Keywords: plasmonic, surface plasmons, thin films, numerical aperture, waveguide

1. Introduction

The current trend towards miniaturization of optical components and devices require methods of observation with high spatial resolutions in the micron or sub-micron optical region. However, conventional optics is diffraction-limited to about half of the optical wavelength (Barnes et al., 2003). Surface plasmon polaritons (SPPs) excited on nanostructured metal-dielectric interfaces turn out to be the promising candidate to overcome the classical diffraction limit (Raether, 1988). SPPs are surface electromagnetic waves that propagate at a metal-dielectric interface and exhibit a strong coupling to the free electrons in the metal. Their electromagnetic field intensity is highest at the surface and decays exponentially away from the interface. If the interface is nanostructured, the spatial dimension of the new structures will determine the distribution of the SPPs field. SPP optical devices built at such an interface includes nanostructures like mirrors, beam splitters and quantum dots (Barnes et al., 2003; Drezet et al., 2005; Evlyukhin, Bozhevolnyi, Stepanov, & Krenn, 2006; González et al., 2006).

Two-photon photopolymerization (TPP) of femtosecond laser is a rapid, cheap and flexible method to fabricate different microstructures such as three-dimensional woodpile photonic crystals with good quality (Sun, Matsuo, & Misawa, 1999; Kaneko, Sun, Duan, & Kawata, 2003; Qi, Lidorikis, & Rakich, 2004; Deubel & Freymann, 2004; Zhou, Kong, Yang, Yan, & Cai, 2007) and plasmonic components (Reinhardt et al., 2006). In this paper we use TPP to fabricate different microstructures in the photosensitive resin of ORganically MOdified CERamic (ORMOCER) as the dielectric structure, which is covered with gold thin film to form the metal-dielectric interface for localization and guiding of SPPs.

We apply the far-field technique to SPP imaging by leakage radiation microscopy (LRM) (Hecht, Bielefeldt, Novotny, Inouye, & Pohl, 1996; Bouhelier et al., 2001; Stepanov et al., 2005; Yang & Zhou, 2013), which simplifies the experiment and accelerates the formation of the SPP intensity images. The leakage radiation relies on the light emitted by the SPPs and can radiate into leaky electromagnetic waves in the substrate based on the asymmetric environment (metal/dielectric). The dielectric structure can be designed to suppress the strong leakage radiation to reduce the SPP losses. Such a far-field optical method allows a direct quantitative imaging and analysis of SPP propagation on the metal-dielectric interfaces.

In this work we combine the TPP micro-fabrication system with the LRM system in the same experimental setup except the laser pattern. Based on such simplified setup, SPPs are excited and observed in different plasmonic components fabricated by TPP. The plasmonic component consisting of gold/ORMOCER/glass structure is shown in Figure 1.

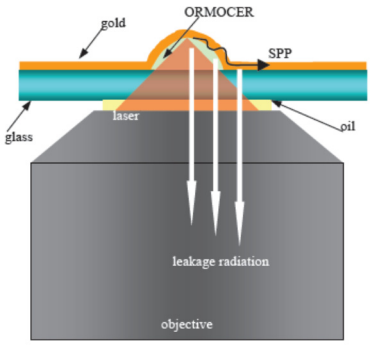

Figure 1. A sketch of the combination of the TPP micro-fabrication system and the LRM system

2. Experiment

For the fabrication of a structure as shown in Figure 1, the ORMOCER is first spun on the cover glass; the laser beam is focused on the ORMOCER to form the surface polymer structure by TPP and finally 50 nm-thin gold films are deposited on the washed samples. The method of finite difference time domain (FDTD) is used to investigate the SPPs distribution in the formed structure (Müller, Ropers, & Lienau, 2004; Chang & Gray, 2005). In Figure 2, the left image is the gold/ORMOCER/glass structure with gold in the top layer, the ORMOCER is in the middle layer and the glass in the bottom layer. The system is irradiated with 800 nm femtosecond laser from the bottom. Simulation results, as shown in the right image of Figure 2, shows that SPPs are excited in the structure, with the strongest intensity in the interface between gold and ORMOCER.

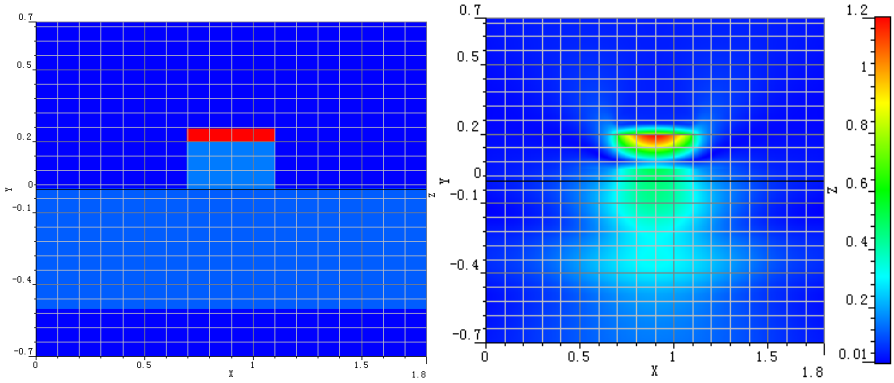

Figure2. A sketch of the Au / resin / glass structure (left) and a simulated distribution of the SPPs in the Au / resin / glass structure (right)

In the TPP micro-fabrication system, the femtosecond laser pulses (30 fs, 82 MHz, 800 nm) are tightly focused into the volume of the photosensitive resin ORMOCER with a high numerical aperture (NA = 1.35) oil immersion objective, while in the LRM system, the femtosecond laser is a continuous laser with the wavelength of 800 nm. The combined system acts like an inverted microscope with a laser source. A charge-coupled device (CCD) camera mounted behind a dichroic mirror in the system is used for online monitoring of the TPP process (Zhou, Kong, Yang, Yan, & Cai, 2007) and excitation collection of the leakage radiation.

An atomic force microscope (AFM) is used for the visual inspection of the ORMOCER structure samples fabricated with TPP. Figure 3 and Figure 4 show AFM images of the micro-grating template and micro-crater template structures respectively. Such templates have good qualities and smooth surfaces and have the potential possibility for localization and guiding of SPPs.

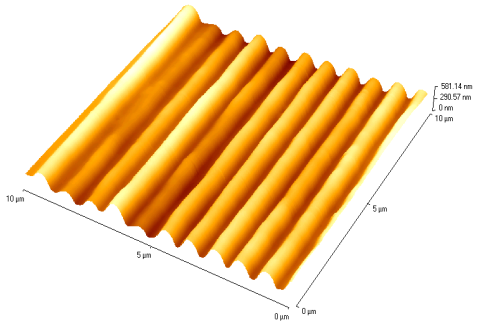

Figure 3.The micro-grating template

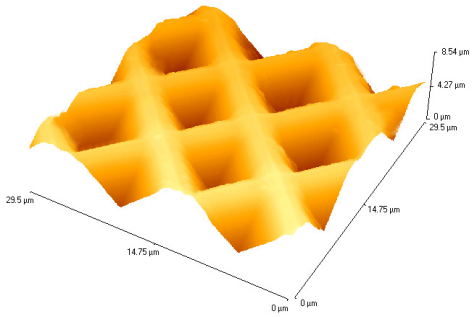

Figure 4.The micro-crater template

3. SPP Excitation and Observation

In the TPP process, the fabrication parameters are controlled using a numerical aperture 1.35, laser power of 60 mW and the scanning speed of 80 μm/s. For such arrangement the lateral rod diameters of the fabricated rods are typically in the range of 800 nm to 1000 nm. The dielectric structures can be used to guide the SPPs. The structure under investigation is a straight waveguide with a rod diameter of about 3000 nm. SPPs can be excited at a wavelength of 800 nm using a laser beam focused on one port (marked with a broken circle in Figure 5) of the waveguide while the propagation of the SPPs is observed on the other port, as shown in Figure 5. For such arrangement the non-radiative SPPs have not been blocked inside the waveguide structure with a relatively high intensity on the exit port due to the confinement and guiding of the ORMOCER waveguide. When the exciting laser beam is focused on the edge of the waveguide, the SPPs will spread across the waveguide and propagate forward as shown in Figure 6, where the SPPs are excited on the edge of the structure with a height of 4000 nm and a rod diameter of about 4000 nm. They propagate over the smooth surface of the structure. This result clearly indicates that SPPs can propagate on smoothly curved surfaces with curvatures larger than the SPP wavelength. The distribution situation in Figure 5 and Figure 6 shows that excitation on different parts of the structure can produce different SPPs.

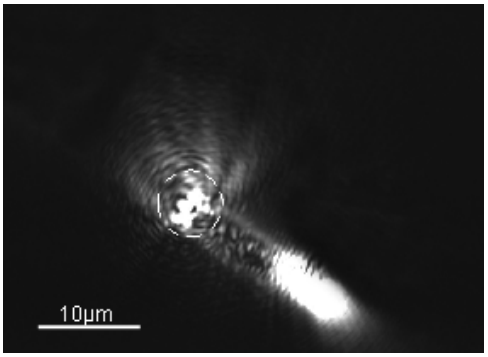

Figure 5. SPPs excited on one port of the waveguide

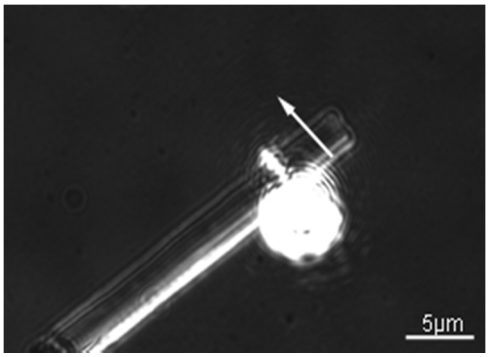

Figure 6. SPPs excited on the edge of the waveguide

We focus on different plasmonic components with right-angled and crossed-waveguide structures and discuss the excitation and transmission of the SPPs in such structures. Two right-angled waveguides are fabricated with side lengths of 10 μm and 20 μm, as shown in Figure 7 and Figure 8 respectively. SPPs excited on one port of the right-angled waveguide propagate forward along the waveguide and weaken as the side lengths increase. There is a large loss of the SPPs in the corner of the right-angled waveguide. The loss increases further at the shorter side length. The regular distribution of SPPs can be observed on the other port of the right-angled waveguide. In Figure 7 and Figure 8, the correct images are the partially enlarged view of the ones in the frames of the left images, which show the SPPs distribution near the exit port in detail. In the side near the exit port of the waveguide, the stripes of SPPs are parallel to each other in the vertical direction to the transmission path. In the other part of the exit port, the SPPs are regular dot patterns due to electromagnetic interference. The stripes can be used to deduce the wavelength of the SPP, which is twice the length of the adjacent two-stripes. The transmission distance of the SPPs is at least 40 μm long, as shown in Figure 8. If we continue to increase the length of the right-angled waveguide, the transmission distance of the SPPs may be longer.

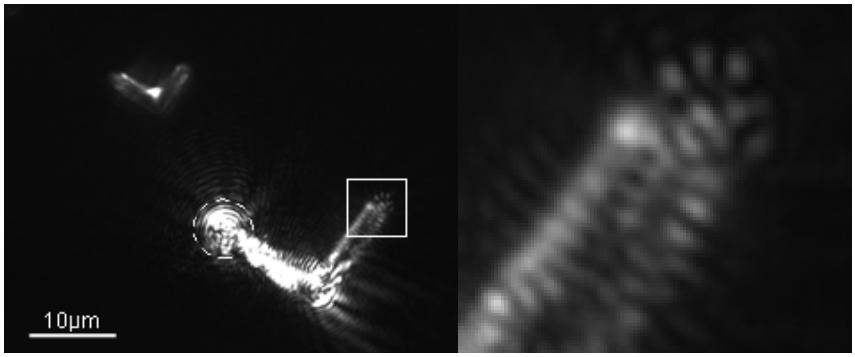

Figure 7. SPPs excited on one port of the right-angled structure with the side length of 10 μm (left) and the partially enlarged view of the one in the frame of the left image (right)

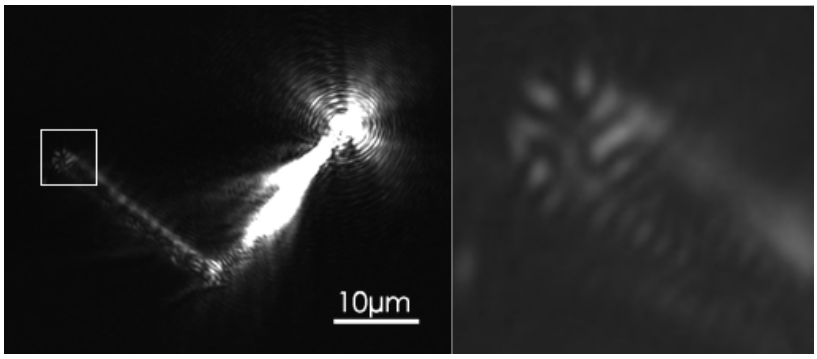

Figure 8. SPPs excited on one port of the right-angled structure with the side length of 20 μm (left) and the partially enlarged view of the one in the frame of the left image (right)

The SPPs can also be excited on the corner of the right-angled waveguide, as shown in Figure 9 and Figure 10. The parallel stripes of the SPPs appear and propagate forward along the waveguide and weaken as the transmission distance increases. The 10 μm-long right-angled structure has a stronger SPPs distribution than the 20 μm-long one as shown in the right images in Figure 9 and Figure 10. The SPPs have the tendency to transmit forward after leaving the waveguide structure as shown in Figure 9 and Figure 10, while they do not show this trend to move forward as shown in Figure 7 and Figure 8. The results show that this structure can be used to control the localization and guiding of SPPs.

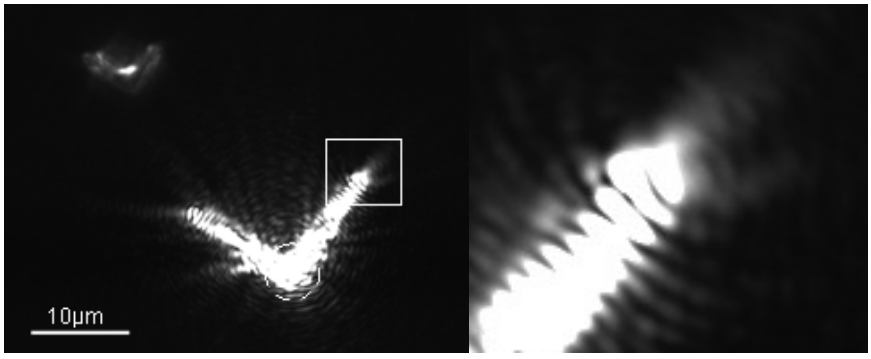

Figure 9. SPPs excited on the corner of the right-angled structure with the side length of 10 μm (left) and the partially enlarged view of the one in the frame of the left image (right)

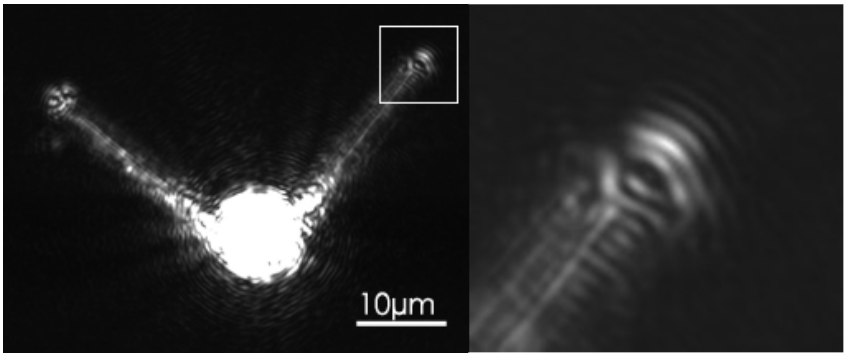

Figure 10. SPPs excited on the corner of the right-angled structure with the side length of 20 μm (left) and the partially enlarged view of the one in the frame of the left image (right)

If the laser beam is focused on the crossed section of the crossed-waveguide, the excited SPPs will transmit forward along the four sides of the structure, as shown in the left image of Figure 11. When focused on one port of the crossed-waveguide, the SPPs will transmit forward along one side, past the cross, and spread to the other three sides, as shown in the right image of Figure 11. Excitation on different sections of the structure can produce different SPPs and different transmission trends. This allows us to design and fabricate different plasmonic components to control the SPP distribution in different parts of the components.

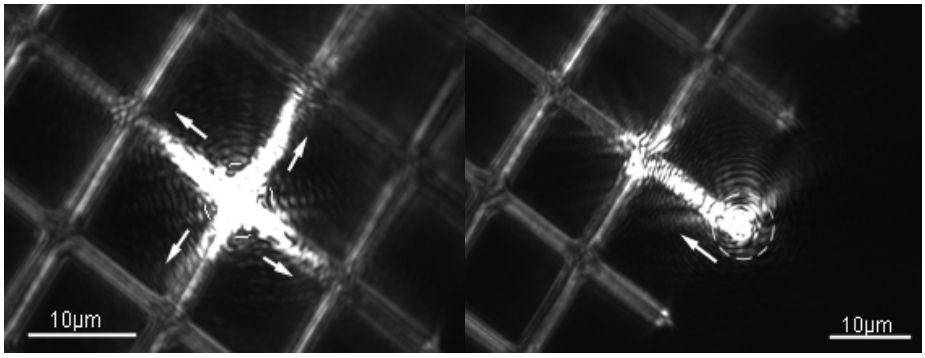

Figure 11. SPPs excited on the crossed part of the crossed-waveguide structure (left), SPPs excited on one port of the crossed-waveguide structure (right). The left image shows SPPs transmitted along the four sides of the structure while the right shows SPPs spreading to the other three sides after excitation on one port

We also fabricated circular structures using TPP with a line width of 800 nm and diameter of 20μm, as in Figure 12. Focusing the laser on different sites on the circle excited different SPPs as shown in the left, middle, and right images in Figure 12. These correspond to the laser position inside, on, and outside of the circle. When the laser position is inside the circle, the SPPs are almost in the inner circle with a short transmission distance in anti-clockwise direction; with the laser on the circle, the SPPs are almost evenly distributed on both sides with the anti-clockwise transmission in the inner and the clockwise transmission in the outer; with the laser outside the circle, the SPPs localize in good condition and almost concentrate in the outer circle with anti-clockwise transmission. With the SPPs excited in the outer circle, we can focus the plasmons by changing the position of the laser beam focus. Placing the laser beam focus below or above the gold/ORMOCER interface will change the intensity of SPPs to adjust the plasmon focus distance. The exciting laser spot indicated by the dashed circles in Figure 12 is about 4μm. If the spot decreases, the SPP focusing effect becomes less pronounced, since the interface area excited by the laser beam decreases. The results show that the circular structure can be used to control the distribution and transmission of SPPs as long as the structure of the component and the excitation location of the laser are well designed.

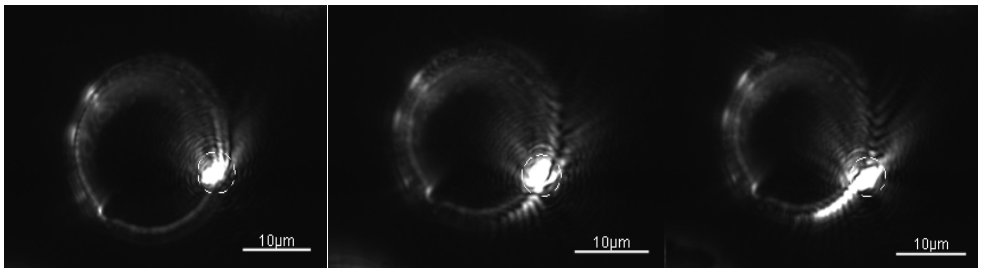

Figure 12. SPPs excited inside the 20 μm diameter circular structure (left), SPPs excited on the circular structure (middle), and SPPs excited outside the circular structure (right)

4. Conclusion

The combination of the fabrication system and the probe system in the same experimental setup has been studied. With the combination system, different micro and nano ORMOCER structures covered by gold have been fabricated by TPP with the femtosecond laser and the properties of the plasmon components with the structured interfaces have been investigated from excitation to observation. The fabricated plasmonic components show good quality and the excited SPPs show effective excitation and focusing. The results on the ease of fabrication of components, the excitation and manipulation of SPPs and the simplicity of the fabrication system and the probe system provide good references for further studies on plasmon components.

Acknowledgement

This work was supported by the Jiangsu Natural ScienceFoundation under Grant CX10B_258Z, China Postdoctoral Science Foundation funded project 20100481093, National Natural Science Foundation of China under Grant No. 50975129.

References

Barnes, W. L., Dereux A., & Ebbesen T. W. (2003). Surface plasmon sub-wavelength optics. *Nature, 424*, 824-830. https://doi.org/10.1038/nature01937

Bouhelier, A., Huser, Th., Tamaru H., Guentherodt, H. J., Pohl, D. W., Baida, F. I., & Van- Labeke, D. (2001). Plasmon optics of structured silver films. *Physics Review B, 63*, 155404. https://doi.org/10.1103/PhysRevB.63.155404

Chang, S. H., & Gray, S. K. (2005). Surface plasmon generation and light transmission by isolated nanoholes and arrays of nanoholes in thin metal films. *Optics Express, 13*, 3150-3165. https://doi.org/10.1364/OPEX.13.003150

Deubel, M., & Freymann, G. V. (2004). Direct laser writing of three-dimensional photonic-crystal templates for telecommunications. *Nature, 3*, 444-447. https://doi.org/10.1038/nmat1155

Drezet, A., Stepanov, A. L., Ditlbacher, H., Hohenau, A., Steinberger, B., Aussenegg, F. R., Leitner, A., & Krenn, J. R. (2005). Surface plasmon propagation in an elliptical corral. *Applied Physics Letters, 86*, 209901-10. https://doi.org/10.1063/1.1870107

Evlyukhin, A. B., Bozhevolnyi, S. I., Stepanov, A. L., & Krenn, J. R. (2006). Splitting of a surface plasmonpolariton beam by chains of nanoparticles. *Applied Physics B, 84*, 29-34. https://doi.org/10.1007/s00340-006-2163-8

González, M. U., Weeber, J.-C., Baudrion, A.-L., Dereux, A., Stepanov, A. L., Krenn, J. R., Devaux, E., & Ebbesen, T. W. (2006). Design, near-field characterization, and modeling of 45° surface-plasmon Bragg mirrors. *Physics Review B, 73*, 155 416. https://doi.org/10.1103/PhysRevB.73.155416

Hecht, B., Bielefeldt, H., Novotny, L., Inouye, Y., & Pohl, D. W. (1996). Local Excitation, Scattering, and Interference of Surface Plasmons. *Physics Review Letters, 77*, 1889-1892. https://doi.org/10.1103/PhysRevLett.77.1889

Kaneko, K., Sun, H. B., Duan, X. M., & Kawata, S. (2003). Two-photon photoreduction of metallic nanoparticle gratings in a polymer matrix. *Applied Physics Letters, 83*, 1426-1428. https://doi.org/10.1063/1.1601302

Müller, R., Ropers, C., & Lienau, C. (2004). Femtosecond light pulse propagation through metallic nanohole arrays: The role of the dielectric substrate. *Optics Express, 12*. 5067-5081. https://doi.org/10.1364/OPEX.12.005067

Qi, M., Lidorikis, E., & Rakich, P. T. (2004). A three-dimensional optical photonic crystal with designed point defects. *Nature, 429*, 538-542. https://doi.org/10.1038/nature02575

Raether, H., (1988). Surface Plasmons on Smooth and Rough Surfaces and on Gratings. Springer Tracts in Modern Physics, Springer, Berlin. https://doi.org/10.1007/BFb0048317

Reinhardt, C., Passinger, S., Chichkov, B. N., Marquart, C., Radko, I. P., & Bozhevolnyi, S. I.(2006). Laser-fabricated dielectric optical components for surface plasmonpolaritons. *Optics Letters, 31*, 1307-1309. https://doi.org/10.1364/OL.31.001307

Stepanov, A. L., Krenn, J. R., Ditlbacher, H., Hohenau, A., Drezet, A., Steinberger, B, Leitner, A., & Aussenegg, F. (2005). Quantitative analysis of surface plasmon interaction with silver nanoparticles. *Optics Letters, 30*, 1524-1526. https://doi.org/10.1364/OL.30.001524

Sun, H. B., Matsuo, S., & Misawa, H. (1999). Three-dimensional photonic crystal structures achieved with two-photon-absorption photopolymerization of resin. *Applied Physics Letters, 74*, 786-788. https://doi.org/10.1063/1.123367

Yang, G., & Zhou, J. (2013).The annealing effect on optical properties of silver copper alloy films. *Applied Mechanics and Materials, 320*, 329-335. https://doi.org/10.4028/www.scientific.net/AMM.320.329

Zhou, M., Kong, J. J., Yang, H. F., Yan, F., & Cai, L. (2007). Rapid Fabrication of Three-Dimensional Woodpile Photonic Crystals by Means of Two-Photon Photopolymeization. *Chinese Physics Letters, 24*, 3164-3167.https://doi.org/10.1088/0256-307X/24/11/040

Applied Physics Research; Vol. 9, No. 6; 2017
ISSN 1916-9639 E-ISSN 1916-9647
Published by Canadian Center of Science and Education

Photoluminescence Characterization of Cadmium Sulphide (CdS) Nanowires for Polarization Studies

Shripriya Poduri[1], Mitra Dutta[1,2] & Michael Stroscio[1,2,3]

[1] Department of Electrical and Computer Engineering, University of Illinois at Chicago, Chicago, IL 60607, USA

[2] Department of Physics, University of Illinois at Chicago, Chicago, IL 60607, USA.

[3] Department of Bioengineering, University of Illinois at Chicago, Chicago, IL 60607, USA

Correspondence: S. Poduri, Department of Electrical and Computer Engineering, University of Illinois at Chicago, Chicago, IL 60607, USA. E-mail: shripriyapoduri@gmail.com

Received: September 30, 2017 Accepted: October 20, 2017 Online Published: November 10, 2017

doi:10.5539/apr.v9n6p26 URL: https://doi.org/10.5539/apr.v9n6p26

Abstract

In this paper, the polarizing properties for CdS nanowire arrays were explored for their potential use in the design of nanowire based polarizers and optical switches. These free standing cadmium sulphide (CdS) nanowires were grown in anodized aluminum oxide (AAO) template via dc electrodeposition. Raman and photoluminescence (PL) measurements were investigated for parallel and perpendicular polarization with two orientations of the sample having light propagating parallel to the nanowire axis in one orientation and light propagating perpendicular to the nanowire axis in other orientation. Polarization-sensitive measurements show strong polarization anisotropy in the photoluminescence (PL) intensity measurements observed in parallel and perpendicular orientation to the long axis of a nanowire. The measured PL ratio, ρ, for parallel to perpendicular orientation was around 0.80- 0.85 which shows strong polarization anisotropy for the grown CdS nanowires. Strong peaks of A1 (TO) at 235 cm^{-1}, E2 mode at 255 cm^{-1} along with 1 LO (longitudinal optical) at 303 cm^{-1}, 2 LO peak at 604 cm^{-1} of the CdS nanowires were seen with different polarizations for Raman spectral studies. These polarization studies show that these dc electrodeposited grown CdS nanowire arrays are well suited for uses in polarization-based nanoscale devices such as in optical switches, and high performance photodetectors.

1. Introduction

With the advent and rapid development of nanotechnology, semiconductor nanowires (NWs) have become essential components for future “nano-devices”. Semiconductor nanoscale structures have generated a great deal of interest owing to their strong confining potentials for electrons and holes and the associated quantum effects (Dutta et al., 2014; Morales & Lieber, 1998; Seminario, 2014; K. Xu et al., 2014). Therefore, semiconductor nanowire devices are being widely used as photo-detectors (Gu et al., 2005; Qian, Gradecak, Li, Wen, & Lieber, 2005), sensors (Brenneman, Poduri, Stroscio, & Dutta, 2013; S. D. Poduri, 2010; Souvik Mukherjee, 2015), lasers (Agarwal, Barrelet, & Lieber, 2005; Duan, Huang, Agarwal, & Lieber, 2003), transistors (Farid et al., 2015; Xiang et al., 2006), optical switches (Kind, Yan, Messer, Law, & Yang, 2002), etc. Recent research in the field of semiconductor nanowires have revealed a lot of interesting properties such as polarization sensitivity (Z. Y. Fan et al., 2004; Shan, Liu, & Hark, 2006), size-dependent photoluminescence (S. Poduri & Stroscio, 2015; Samuelson et al., 2004), quantum dots in nanowires for LEDs (light emitting diodes) (Gudiksen, Wang, & Lieber, 2002), etc. These interesting properties of semiconductor nanowire devices are being employed in both scientific and industrial applications. One of the most important II-IV semiconductor compounds, cadmium sulphide (CdS) was selected because it is used widely in optoelectronic devices due to its direct band gap of 2.42 eV and its excellent semiconducting properties.

Cadmium sulphide nanowires have significant advantages such as high aspect ratio, huge surface to volume ratio leading to higher sensitivity of excitons to surface states and defects as compared to their bulk counterpart, and excellent electron emission or absorption property in optoelectronic applications(Mazouchi, Poduri, & Dutta, 2014; Poduri, Dutta, & Stroscio, 2014). But the current understanding of using grown CdS nanowires as polarizers is limited and therefore the polarizing properties of grown CdS nanowires have been explored as reported in this paper to demonstrate their potential uses in polarization-based nanoscale devices. DC

electrodeposition of CdS nanowires is not very commonly done for samples with very narrow pore diameters. However, in this paper CdS nanowires were grown by using a simple dc electrodeposition process into the narrow pores of 10-60 nm diameters by overcoming the challenges faced during the growth of CdS nanowires. The challenge faced during the growth of electrodeposited CdS nanowires is barrier layer removal which leads to poor crystalline structure of nanowires. The growth of decent quality CdS nanowires was achieved, even though it has been stated in (Routkevitch, Bigioni, Moskovits, & Xu, 1996) that DC electrodeposition was not an easy process for growing nanowires in narrow pores. The method of barrier layer removal is also discussed in this paper. Polarization studies with DC electrodeposited grown CdS nanowires has not been performed so far.

The polarization anisotropy feature employed in high performance nanowire polarizers can be explained in terms of the large dielectric difference between these freestanding nanowires and the surrounding environment. This property of polarization anisotropy is employed here to demonstrate its potential use in the application of high performance polarization-based sensitive nanoscale based optical switches, and polarizers (Wang, Gudiksen, Duan, Cui, & Lieber, 2001).

2. Experimental Details

2.1 Growth of Anodized Alumina Templates and Nanowires

Recently, a lot of research has been done in growing free standing nanowires on a substrate in a controlled fashion (Anyebe et al., 2015; Taşaltın, Öztürk, Kılınç, Yüzer, & Öztürk, 2010; Zhou et al., 2009). Growing free standing nanowires has always been a challenge but the easiest and most economical way to grow free standing nanowires is through self assembly of electrodeposited CdS nanowires in an anodized alumina template. CdS nanowires were grown in anodized aluminum sheet metal of thickness of 500 μm. The anodized template was prepared using the protocol given in Routkvitch et al. (1996). The aluminum (Al) metal sheet (99.9 % purity) of 2” × 0.5” × 0.020” dimensions was cleaned by ultrasonication in acetone for 1 hour followed by ultrasonication in methanol for 1 hour. These Al metal sheets were then electropolished in perchloric acid and ethanol solution having volume ratio of 1:5 at 0 °C for 15 minutes. After electro-polishing, the templates were anodized at a potential of 40 V for a minimum of 16 hours and the temperature was maintained at 10 °C throughout the process. After the first anodization step, the oxide layer was removed by immersing the sample in a solution of 1.8 % wt chromic acid and 6 % wt phosphoric acid at 60 °C for 4-5 hours. The second anodization was performed with the same conditions as that of the first anodization step but the time of the anodization this time was only 20 minutes. The barrier layer was removed by dipping the anodized template in 0.5 M phosphoric acid for 75 minutes at room temperature. The electrolyte for CdS electrodeposition was a solution of dimethyl sulfoxide (DMSO) comprising of 0.055 M CdCl2 and 0.19 M elemental sulfur (Xu et al., 2000; Yang et al., 2002). The temperature of the electrolyte was 120-150 °C during the electrodeposition growth and current density of 15 mA/cm2 was applied for 7-10 s. The deposition rate was 25-30 nm/s. After the DC electrodeposition, the sample was rinsed in hot DMSO followed by acetone and cleaned in deionized water. The AAO template was dissolved in 1 M NaOH solution at room temperature for 8 min to liberate the CdS nanowires.

2.2 Photoluminescence and Raman Experimental Set Up

To study the polarization anisotropy, PL studies were performed with the continuous wave He-Cd laser of wavelength 441 nm for parallel and perpendicular polarization with two orientations of the sample having light propagating parallel to the nanowire axis in one orientation as shown in Figure 1 and light propagating perpendicular to the nanowire axis in other orientation as shown in Figure 2. The PL and Raman intensities were recorded at room temperature using He-Cd laser of wavelength 441 nm and Acton 2500i spectrometer. The polarization filter used was LPVISE100 purchased from Thor labs Inc. For measuring Raman spectra, holographic notch filters were used to do the Raman measurements, and the Raman system was calibrated by measuring the phonon peak on silicon first. PL and Raman intensities were recorded five times for parallel and perpendicular polarization with two orientations of the sample having light propagating parallel to the nanowire axis in one orientation and light propagating perpendicular to the nanowire axis in other orientation.

The phononic modes of these polarizations were also studied to investigate further the anisotropy present in the CdS nanowires. Therefore, Raman characteristics were recorded for two orientations of the sample with light propagating parallel (||) to the nanowire axis in one orientation as shown in Figure 1 and light propagating perpendicular (⊥) to the nanowire axis in other orientation as shown in Figure 2. Raman intensities were recorded for both parallel Z(XX)Z and perpendicular polarization Z(XY)Z of the laser. The notations Z(XY)Z described in this paper are to designate the directions. The directions inside the parentheses denote the polarizations of the incident and scattered beams, respectively. The directions preceding and following outside

the parentheses indicate the respective directions of the incident beam and scattered beams (Arguello, Rousseau, & Porto). In addition, the electron phonon coupling interactions were studied by performing Raman spectroscopy at different angles of laser polarization with the same Raman experiment set up.

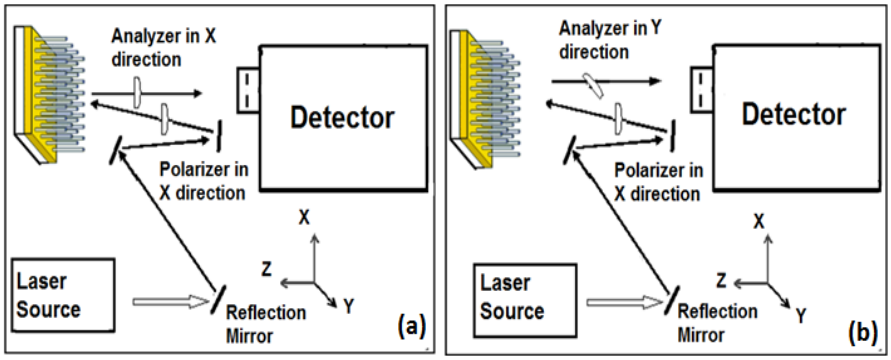

Figure 1. (a) Parallel and (b) perpendicular polarization with light propagating parallel to the nanowire axis

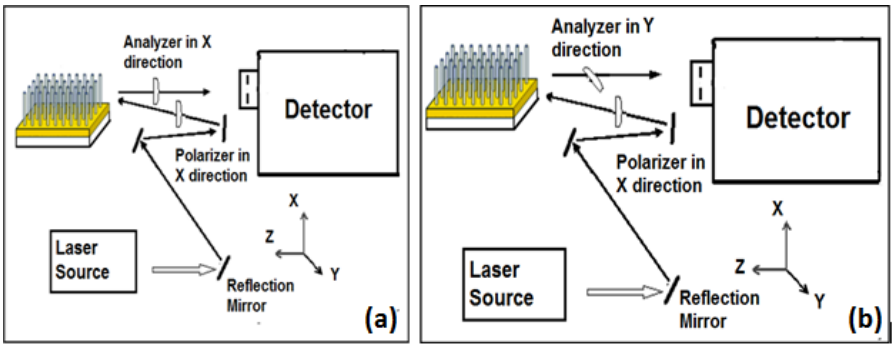

Figure 2. (a) Parallel and (b) perpendicular polarization with light propagating perpendicular to the nanowire axis

3. Results and Discussions

3.1 PL Measurements Results

The polarization anisotropy in PL measurements between the free standing nanowires and their surrounding environment can be explained by a model where the nanowire can be assumed as an infinitely long dielectric cylinder in vacuum or air, since the wavelength of the exciting light is much greater than the wire diameter. When the incident field is polarized parallel to the cylinder, the electric field inside the cylinder is not attenuated. But, when polarized perpendicular to the cylinder, the electric field amplitude is attenuated (Ruda & Shik, 2005) according to (1)

$$E_i = \frac{2\varepsilon_0}{\varepsilon+\varepsilon_0} E_e \tag{1}$$

where Ei is the electric field inside the cylinder, Ee the excitation field, and ε is the dielectric constant of the cylinder (which is nanowire in our case) and ε_0 is the dielectric constant of the surrounding (air). For $\varepsilon > \varepsilon_0$, the incident light in the direction of polarization parallel to the nanowire axis creates an electric field of high frequency in the nanowire. The PL spectra can be recorded from a number of individual wires as a function of excitation or emission polarization (Ils et al., 1995; Vouilloz et al., 1998). On average, the excitation and emission polarization ratio is given by (2):

$$\rho = \frac{I_{||} - I_{\perp}}{I_{||} + I_{\perp}} \quad (2)$$

The intensities parallel ($I_{||}$) and perpendicular ($I_{\perp}$) to the wire can be measured with the PL measurements at different angles of orientation. The anisotropy in the photoluminescence when a nanowire array is excited with a beam polarized parallel and perpendicular to its long axis has been explained theoretically by Ruda and Shik (2005). They considered an array of dipoles randomly oriented in a dielectric cylinder and calculated the Poynting vector outside the cylinder resulting from the incoherent dipole emission. Ruda and Shik found that under this assumption the anisotropy contrast of the emission is given by

$$\frac{I_{||}}{I_{\perp}} = \frac{(\varepsilon+\varepsilon_0)^2 + 2\varepsilon_0^2}{6\varepsilon_0^2} \quad (3)$$

The large polarization response is due primarily to the large dielectric difference between the nanowire and its air or vacuum surroundings. Calculating the polarization anisotropy, ρ, using this equation for the CdS nanowires gives 0.87 (0.89) using dielectric constant $\varepsilon_{\perp}(\varepsilon_{||})$ of CdS as 8.5 (9.25) from Table 1 (Lee, Kim, Dutta, & Stroscio, 1997). Therefore, to study the polarization anisotropy, PL studies were done with and without the polarization filter and PL intensity were recorded for parallel and perpendicular polarization with two orientations of the sample having light propagating parallel to the nanowire axis in one orientation and light propagating perpendicular to the nanowire axis in other orientation.

Table 1. Parametric constants of CdS (Lee et al., 1997)

Parameter	Value
Band gap (eV)	2.42
Dielectric constant at low frequency along z ($\boldsymbol{\varepsilon}_{||}$)	9.25
Dielectric constant at low frequency perpendicular to z ($\boldsymbol{\varepsilon}_{\perp}$)	8.7
Dielectric constant at high frequency along z ($\boldsymbol{\varepsilon}_{\infty||}$)	5.5
Dielectric constant at low frequency perpendicular to z ($\boldsymbol{\varepsilon}_{\infty\perp}$)	5.53

The CdS nanowires were grown in AAO templates and were examined under JEOL 7500 Scanning Electron Microscope (SEM) to ascertain the growth of CdS nanowire. The SEM micrograph of the CdS nanowires is shown in Figure 3.

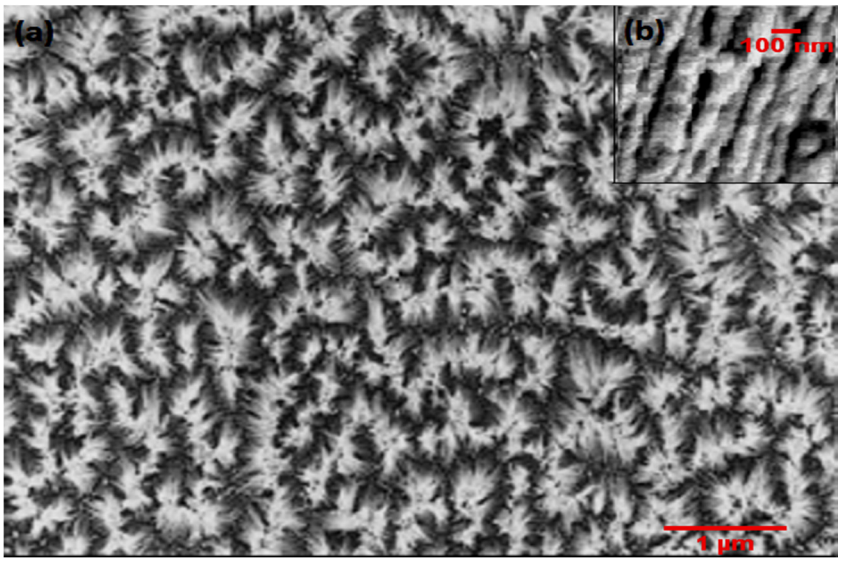

Figure 3. (a) Top view SEM of CdS nanowires grown in anodized alumina sheet of 500 μm. (b) SEM micrograph of tilted side view of CdS nanowires at a higher magnification

Raman and PL intensities were recorded for parallel and perpendicular polarization with two orientations of the sample as shown in Figure 1 and 2. The measured PL with and without the polarization filter for parallel and perpendicular polarization is shown in Figure 4. Therefore, the measured polarization ratio, ρ , is given by

equation (3) by taking the intensity values from Figure 4 (a) is 0.85 when light is propagating along the length of the nanowire and 0.80 when light is propagating perpendicular to the length of the nanowire. The measured PL ratio which is 0.80 or 0.85 is in agreement with our calculated PL ratio 0.87. Therefore, it can be said that the CdS nanowires would be suitable for polarized based applications. The reported phonon frequencies observed for CdS wurtzite crystal in (Arguello et al.) are given in Table II. Furthermore, to evaluate the crystal quality for structural distortions, the photoluminescence power dependence was investigated for the determination of underlying excitonic emission or recombination methods, PL was performed after annealing with different neutral density filters (purchased from Thorlabs Inc.) (Schmidt, Lischka, & Zulehner, 1992). The PL spectral intensity for various transmission laser power density percentages after annealing has been shown in Figure 5(a) and the plot for the PL intensity with respect to various transmission laser power density percentages is in Figure 5 (b). The plot of PL intensity area under the curve with respect to different excitation power is a near linear plot with a positive slope which proves that the emission was mainly from excitons and the recombination were mostly from band to band and there were minimal structural distortions as well. Also, to study more about the structural distortions and phononic structure, Raman spectroscopy studies were performed in different angles of laser polarization. All the modes were seen in Raman spectroscopy which is in agreement with CdS nanowires structures attributing to decent quality CdS nanowires with minimal structural defects.

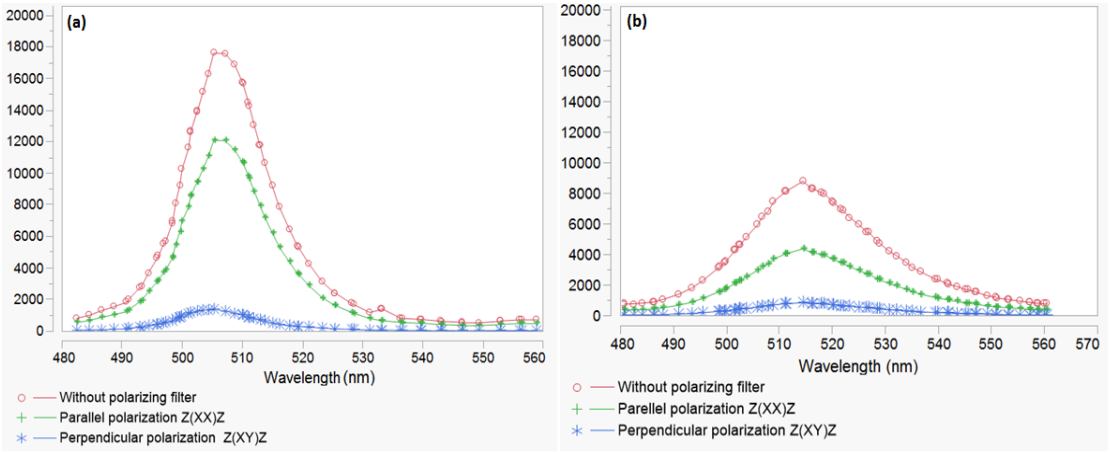

Figure 4. (a) PL peak intensity variation measured when light is propagating along the length of the nanowire along Z. (b) PL peak intensity variation measured when light is propagating along Z but perpendicular to the length of the nanowire. The measured PL ratio is 0.80

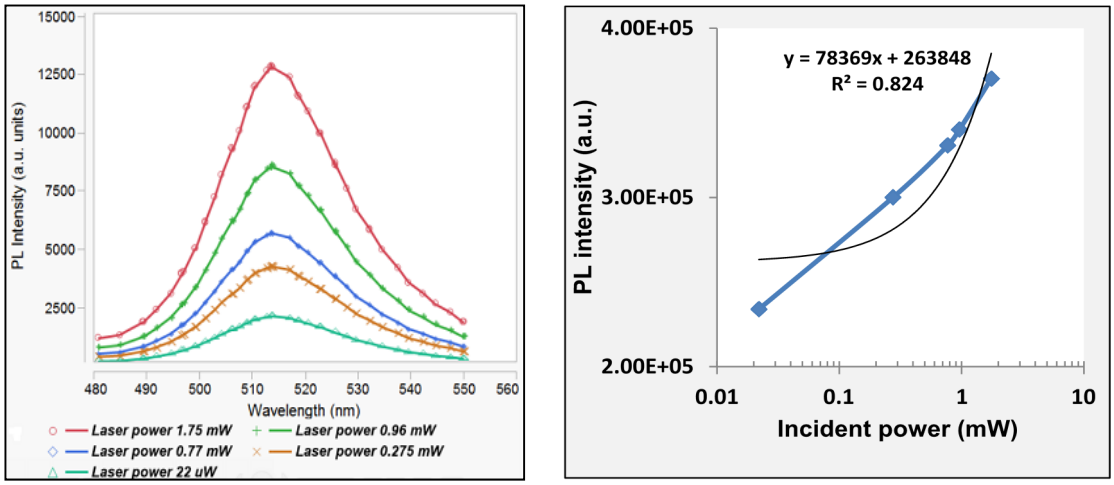

(a) (b)

Figure 5. (a) PL spectra of CdS nanowires with different laser excitation power using neutral density filters (b) PL intensity area variation vs. different laser excitation power using neutral density filters

Figure 5 shows the Raman spectra of CdS nanowires using the polarization filter when light is propagating along the length of the wire along Z. Peaks in intensity were observed at A1 (TO) at 235 cm-1 for parallel polarization and at E2 at 258 cm-1 for perpendicular polarization along with 1 LO, 2 LO at 309 and 607 cm-1 respectively. These peaks are in accordance with the CdS values of transverse and longitudinal mode peaks (Fan et al., 2007). Also, Raman spectral studies were performed with the polarization filter when light was propagating perpendicular to the length of the wire. The peaks were found at peak at E1 (transverse) at 243 cm-1 for parallel polarization of incident light as shown Figure 6 (a) and at quasi A1 (transverse) at 239 cm-1 for perpendicular polarization as shown in Figure 6 (b) along with 1 LO, 2 LO at 310 and 604 cm-1 , respectively.

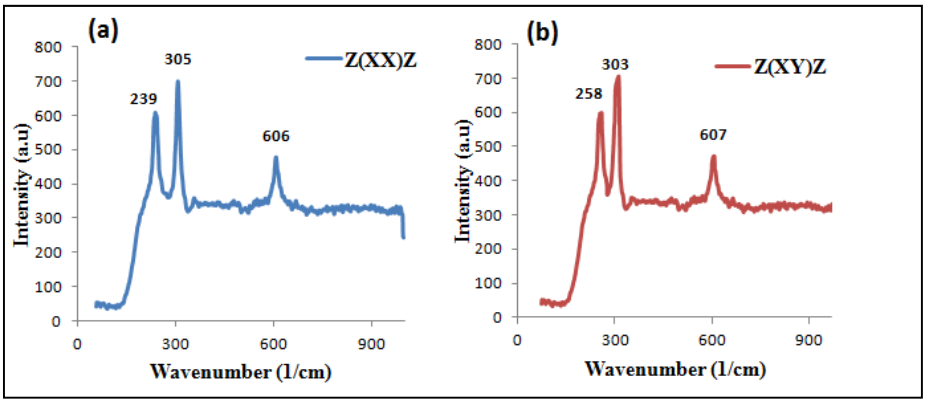

Figure 6. Raman using the polarization filter with peak at A1 (TO) at 239 cm^{-1} for parallel polarization in (a) and at E2 at 258 cm^{-1} for perpendicular polarization in (b) along with 1 LO, 2 LO at 305 and 607 cm^{-1} respectively when light is propagating along the length of the wire along Z

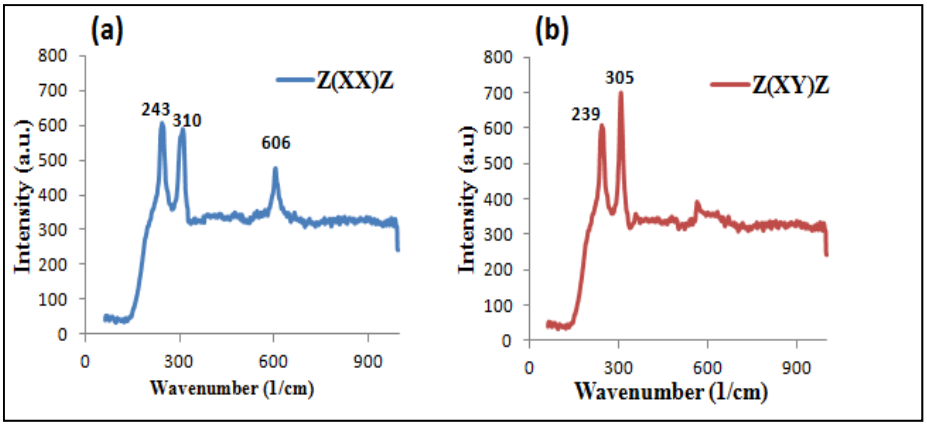

Figure 7. Raman using the polarization filter with peak at E1 (transverse) at 243 cm^{-1} for parallel polarization in (a) and at quasi A1 (transverse) at 239 cm^{-1} for perpendicular polarization in (b) along with 1 LO, 2 LO at 310 and 606 cm^{-1}, respectively when light is propagating along Z but perpendicular to the length of the wire

The observed peaks were slightly different for CdS NWs than the reported frequencies of CdS bulk crystals given in Table 2. It was observed experimentally that the magnitude of Huang Rhys factor, which signifies the electron phonon coupling strength, decreases with the increasing angles of laser polarization. The Huang Rhys factor is the ratio of normalized Raman intensity of 2 LO peak with respect to 1 LO peak and is computed from the experimental data of Raman spectrum shown in Figure 6. The electron phonon coupling strength S is estimated by measuring the Raman intensity of the 2 LO phonon with respect to that of the LO phonon (Fan et al., 2008) where S is the Huang Rhys factor. The calculation of the Huang Rhys factor for the experimental data shown in Figure 8 is given in Table 3.

Table 2. Optical phonon modes of wurtzite CdS crystal (cm^{-1}) (Lee et al., 1997)

Optical mode	CdS
E2	43
E2	256
A1	234
Quasi- A1 (transverse)	240
Quasi- E1 (transverse)	239
E1 (transverse)	243
A1 (longitudinal)	305
Quasi- A1 (longitudinal)	306
Quasi- E_1 (longitudinal)	306
E_1 (longitudinal)	307

Table 3. Huang Rhys factor values computed from experimental data given in Figure 6

Angle θ in degrees	**Huang Rhys parameter, S**
0	1.1
30	0.88
60	0.78
90	0.67

It is observed that the Raman intensity is dependent on the angle of the laser polarization, the orientation of the nanowires and also the electron phonon interaction in the nanowires. Also, with polarization anisotropy present in the nanowires, the symmetry of the phonon modes is still in agreement with the phononic structure of CdS nanowires with minimal local structural distortions.

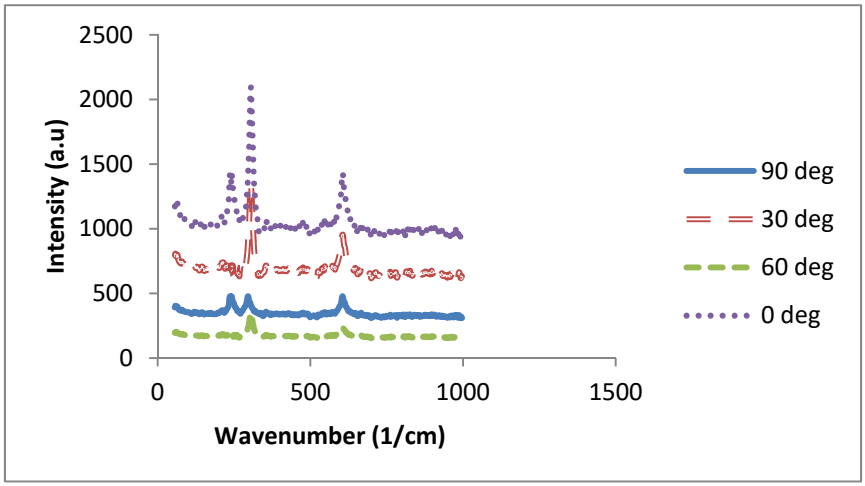

Figure 8. Experimental data for Raman spectra with different angles. $\boldsymbol{\theta}$ denotes the angle between the long axis of the nanowire (z axis) and the laser polarization

4. Conclusion

There are many ways to grow CdS nanowires but growing vertically aligned nanowires has always been a challenge. This paper discusses about the most economical way is to grow vertically aligned nanowires in a nanoporous template through dc electrodeposition by overcoming the bottlenecks of barrier layer removal during the growth of CdS nanowires which can sometimes lead to poor crystallinity of grown CdS nanowires. CdS nanowires were self assembled in an anodized aluminum sheet metal of thickness of 500 µm. The polarization properties of the CdS nanowires were investigated for their use in polarization sensitive optoelectronic devices. Also, the PL peaks were in accordance to the bandgap of CdS nanowires showing good crystalline growth of CdS nanowires via dc electrodeposition. Polarization-sensitive measurements reveal a striking anisotropy in the

PL intensity recorded parallel and perpendicular to the long axis of a nanowire. The measured PL ratio, ρ, is around 0.80-0.85 indicating very good polarization anisotropy for CdS nanowires. The highest polarization ratio observed previously for CdS nanowires is only 0.78 (Acharya, Patla, Kost, Efrima, & Golan, 2006; Robert et al., 2014) (H. M. Fan, Ni, Feng, Fan, Shen, et al., 2007). These nanowire arrays can be used as optical switches as a result of their polarization anisotropy properties. This research may pave the way for an economical fabrication of polarization sensitive nanoscale devices with high performance. The observed peaks were slightly different for CdS NWs than the reported frequencies of CdS bulk crystals given in Table 2. The 1 LO phonon energy has been observed more for CdS NWs as compared to CdS bulk. The same behavior with the increase in 1 LO phonon energy was also reported in Refs. (Fu, Li, & Tang; Pan et al.). Also, good crystallinity enhances multiphonon responses due to well-defined phonons in the material. The optical properties of CdS nanowires are also influenced greatly by orientation and polarization angle as seen in the paper. Hence, CdS nanowires with good crystallinity can be grown using simple methods such as dc electrodeposition making it possible to use them for its use in high performance nanowire polarizer application.

Acknowledgments

We gratefully acknowledge that anodized alumina templates were grown in Brown University by one of us (S.D.) under the supervision of Prof. Jimmy Xu and this work was partially supported by AFOSR FA9550-11-1-0271.

References

Acharya, S., Patla, I., Kost, J., Efrima, S., & Golan, Y. (2006). Switchable Assembly of Ultra Narrow CdS Nanowires and Nanorods. *Journal of the American Chemical Society, 128*(29), 9294-9295. https://doi.org/10. 1021/ja062404i

Agarwal, R., Barrelet, C. J., & Lieber, C. M. (2005). Lasing in single cadmium sulfide nanowire optical cavities. *Nano Letters, 5*(5), 917-920. https://doi.org/10.1021/Nl050440u

Anyebe, E. A., Sanchez, A. M., Hindmarsh, S., Chen, X., Shao, J., Rajpalke, M. K., . . . Zhuang, Q. (2015). Realization of Vertically Aligned, Ultrahigh Aspect Ratio InAsSb Nanowires on Graphite. *Nano Letters, 15*(7), 4348-4355. https://doi.org/10.1021/acs.nanolett.5b00411

Arguello, C. A., Rousseau, D. L., & Porto, S. P. S. (1969). First-Order Raman Effect in Wurtzite-Type Crystals. *Physical Review, 181*(3), 1351-&. https://doi.org/10.1103/Physrev.181.1351

Brenneman, K. L., Poduri, S., Stroscio, M. A., & Dutta, M. (2013). Optical detection of lead (II) ions using DNA-based nanosensor. *IEEE Sensors Journal, 13*(5), 1783-1786.

Duan, X. F., Huang, Y., Agarwal, R., & Lieber, C. M. (2003). Single-nanowire electrically driven lasers. *Nature, 421*(6920), 241-245. https://doi.org/10.1038/Nature01353

Dutta, M., Stroscio, M. A., Qian, J., Wu, T.-C., Sen, B., Zhang, N., . . . Shukla, P. (2014). Semiconductor Quantum Dots: Nanosensors Based on DNA and RNA Aptamers *Dekker Encyclopedia of Nanoscience and Nanotechnology, Third Edition* (pp. 4383-4389). CRC Press.

Fan, H. M., Fan, X. F., Ni, Z. H., Shen, Z. X., Feng, Y. P., & Zou, B. S. (2008). Orientation-dependent Raman spectroscopy of single wurtzite CdS nanowires. *Journal of Physical Chemistry C, 112*(6), 1865-1870. https://doi.org/10.1021/Jp7096839

Fan, H. M., Ni, Z. H., Feng, Y. P., Fan, X. F., Kuo, J. L., Shen, Z. X., & Zou, B. S. (2007). Anisotropy of electron-phonon coupling in single wurtzite CdS nanowires. *Applied Physics Letters, 91*(17). https://doi.org/10. 1063/1.2805380

Fan, H. M., Ni, Z. H., Feng, Y. P., Fan, X. F., Shen, Z. X., & Zou, B. S. (2007). High-pressure Raman and photoluminescence of highly anisotropic CdS nanowires. *Journal of Raman Spectroscopy, 38*(9), 1112-1116. https://doi.org/10.1002/jrs.1724

Fan, Z. Y., Chang, P. C., Lu, J. G., Walter, E. C., Penner, R. M., Lin, C. H., & Lee, H. P. (2004). Photoluminescence and polarized photodetection of single ZnO nanowires. *Applied Physics Letters, 85*(25), 6128-6130. https://doi.org/10.1063/1.1841453

Farid, S., Meshik, X., Choi, M., Mukherjee, S., Lan, Y., Parikh, D., . . . Wang, Y. Y. (2015). Detection of Interferon gamma using graphene and aptamer based FET-like electrochemical biosensor. *Biosensors and Bioelectronics, 71*, 294-299.

Fu, X. L., Li, L. H., & Tang, W. H. (2006). Preparation and characterization of CdS/Si coaxial nanowires. *Solid State Communications, 138*(3), 139-142. https://doi.org/10.1016/J.Ssc.2006.02.015

Gu, Y., Kwak, E. S., Lensch, J. L., Allen, J. E., Odom, T. W., & Lauhon, L. J. (2005). Near-field scanning photocurrent microscopy of a nanowire photodetector. *Applied Physics Letters, 87*(4). https://doi.org/10.1063/1.1996851

Gudiksen, M. S., Wang, J., & Lieber, C. M. (2002). Size-Dependent Photoluminescence from Single Indium Phosphide Nanowires. *The Journal of Physical Chemistry B, 106*(16), 4036-4039. https://doi.org/10.1021/jp014392n

Ils, P., Greus, C., Forchel, A., Kulakovskii, V. D., Gippius, N. A., & Tikhodeev, S. G. (1995). Linear-Polarization of Photoluminescence Emission and Absorption in Quantum-Well Wire Structures - Experiment and Theory. *Physical Review B, 51*(7), 4272-4277. https://doi.org/10.1103/Physrevb.51.4272

Kind, H., Yan, H., Messer, B., Law, M., & Yang, P. (2002). Nanowire Ultraviolet Photodetectors and Optical Switches. *Advanced Materials, 14*(2), 158-160. https://doi.org/10.1002/1521-4095(20020116)14:2<158::AID-ADMA158>3.0.CO;2-W

Lee, B. C., Kim, K. W., Dutta, M., & Stroscio, M. A. (1997). Electron-optical-phonon scattering in wurtzite crystals. *Physical Review B, 56*(3), 997-1000. https://doi.org/10.1103/Physrevb.56.997

Mazouchi, M., Poduri, S., & Dutta, M. (2014). Growth and Characterization of Indium Oxide, Zinc Oxide and Cadmium Sulfide Nanowires by Vapor-Liquid-Solid Growth Technique. *Applied Physics Research, 6*(6), 55.

Morales, A. M., & Lieber, C. M. (1998). A laser ablation method for the synthesis of crystalline semiconductor nanowires. *Science, 279*(5348), 208-211. https://doi.org/10.1126/Science.279.5348.208

Mukherjee, S., Meshik, X., Choi, M., Farid, S., Datta, D., Lan, Y., ... & Wang, Y. Y. (2015). A graphene and aptamer based liquid gated FET-like electrochemical biosensor to detect adenosine triphosphate. *IEEE transactions on nanobioscience*, *14*(8), 967-972.

Pan, A. L., Liu, R. B., Yang, Q., Zhu, Y. C., Yang, G. Z., Zou, B. S., & Chen, K. Q. (2005). Stimulated emissions in aligned CdS nanowires at room temperature. *Journal of Physical Chemistry B, 109*(51), 24268-24272. https://doi.org/10.1021/Jp055164m

Poduri, S. D. (2010). Theoretical Modeling and Analysis of Ammonia Gas Sensing Properties of Vertically Aligned Multiwalled Carbon Nanotube Resistive Sensors and Enhancing Their Sensitivity.

Poduri, S., Dutta, M., & Stroscio, M. (2014). Characterization of CdS Nanowires Self-Assembled in a Nanoporous Alumina Template. *Journal of Electronic Materials, 43*(11), 3979-3983. https://doi.org/10.1007/S11664-014-3305-0

Qian, F., Gradecak, S., Li, Y., Wen, C. Y., & Lieber, C. M. (2005). Core/multishell nanowire heterostructures as multicolor, high-efficiency light-emitting diodes. *Nano Letters, 5*(11), 2287-2291. https://doi.org/10.1021/Nl051689e

Robert, R., Daniel, P., Arian, K., Robert, B., Sebastian, G., Ulf, P., & Carsten, R. (2014). Polarization features of optically pumped CdS nanowire lasers. *Journal of Physics D: Applied Physics, 47*(39), 394012.

Routkevitch, D., Bigioni, T., Moskovits, M., & Xu, J. M. (1996). Electrochemical Fabrication of CdS Nanowire Arrays in Porous Anodic Aluminum Oxide Templates. *The Journal of Physical Chemistry, 100*(33), 14037-14047. https://doi.org/10.1021/jp952910m

Routkevitch, D., Bigioni, T., Moskovits, M., & Xu, J. M. (1996). Electrochemical fabrication of CdS nanowire arrays in porous anodic aluminum oxide templates. *Journal of Physical Chemistry, 100*(33), 14037-14047. https://doi.org/10.1021/Jp952910m

Ruda, H. E., & Shik, A. (2005). Scanning capacitance microscopy of nanostructures - art. no. 075315. *Physical Review B, 71*(7). https://doi.org/10.1103/Physrevb.71.075316

S. Poduri, M. S. C., Mitra Dutta, & Stroscio, M. (2015). *Numerical analysis of electric field enhancement in ZnO film with plasmonic au quantum dots.* Paper presented at the IEEE International Workshop Conference of Computational Electronics.

Samuelson, L., Bjork, M. T., Deppert, K., Larsson, M., Ohlsson, B. J., Panev, N., . . . Wallenberg, L. R. (2004). Semiconductor nanowires for novel one-dimensional devices. *Physica E-Low-Dimensional Systems & Nanostructures, 21*(2-4), 560-567. https://doi.org/10.1016/J.Physe.2003.11.072

Schmidt, T., Lischka, K., & Zulehner, W. (1992). Excitation-power dependence of the near-band-edge photoluminescence of semiconductors. *Physical Review B, 45*(16), 8989-8994.

Seminario, J. M. (2014). *Design and Applications of Nanomaterials for Sensors* (Vol. 16): Springer.

Shan, C. X., Liu, Z., & Hark, S. K. (2006). Photoluminescence polarization in individual CdSe nanowires. *Physical Review B, 74*(15). https://doi.org/10.1103/Physrevb.74.153402

Taşaltın, N., Öztürk, S., Kılınç, N., Yüzer, H., & Öztürk, Z. (2010). Fabrication of vertically aligned Pd nanowire array in AAO template by electrodeposition using neutral electrolyte. *Nanoscale Research Letters, 5*(7), 1137-1143. https://doi.org/10.1007/s11671-010-9616-z

Vouilloz, F., Oberli, D. Y., Dupertuis, M. A., Gustafsson, A., Reinhardt, F., & Kapon, E. (1998). Effect of lateral confinement on valence-band mixing and polarization anisotropy in quantum wires. *Physical Review B, 57*(19), 12378-12387. https://doi.org/10.1103/Physrevb.57.12378

Wang, J. F., Gudiksen, M. S., Duan, X. F., Cui, Y., & Lieber, C. M. (2001). Highly polarized photoluminescence and photodetection from single indium phosphide nanowires. *Science, 293*(5534), 1455-1457. https://doi.org/ 10.1126/Science.1062340

Xiang, J., Lu, W., Hu, Y., Wu, Y., Yan, H., & Lieber, C. M. (2006). Ge/Si nanowire heterostructures as high-performance field-effect transistors. *Nature, 441*(7092), 489-493. https://doi.org/10.1038/nature04796

Xu, D. S., Xu, Y. J., Chen, D. P., Guo, G. L., Gui, L. L., & Tang, Y. Q. (2000). Preparation and characterization of CdS nanowire arrays by dc electrodeposit in porous anodic aluminum oxide templates. *Chemical Physics Letters, 325*(4), 340-344. https://doi.org/10.1016/S0009-2614(00)00676-X

Xu, K., Purahmad, M., Brenneman, K., Meshik, X., Farid, S., Poduri, S., . . . Dutta, M. (2014). Design and Applications of Nanomaterial-Based and Biomolecule-Based Nanodevices and Nanosensors. In J. M. Seminario (Ed.), *Design and Applications of Nanomaterials for Sensors* (pp. 61-97). Dordrecht: Springer Netherlands.

Yang, Y., Chen, H. L., Mei, Y. F., Chen, J. B., Wu, X. L., & Bao, X. M. (2002). Anodic alumina template on Au/Si substrate and preparation of CdS nanowires. *Solid State Communications, 123*(6-7), 279-282. https://doi.org/S0038-1098(02)00304-6 Doi 10.1016/S0038-1098(02)00304-6

Zhou, W., Zhang, J., Li, X., Liu, Y., Min, G., Song, Z., & Zhang, J. (2009). Replication of mold for UV-nanoimprint lithography using AAO membrane. *Applied Surface Science, 255*(18), 8019-8022. https://doi.org/10.1016/j.apsusc.2009.05.006

Applied Physics Research; Vol. 9, No. 6; 2017
ISSN 1916-9639 E-ISSN 1916-9647
Published by Canadian Center of Science and Education

Microbial Purification in Well-Water Using UV-Vis LEDs and Monitoring Using Laser-Induced Fluorescence

Samuel Sonko Sackey[1], Baah Sefa-Ntiri[1], Patrick Mensah-Amoah[1], Jonathan Ntow[2], Michael Kwame Vowotor[3], Andrew Huzortey[1] & Angela Akyea[1]

[1] Laser and Fibre Optics Centre, Department of Physics, University of Cape Coast, Ghana

[2] Department of Laboratory Technology, University of Cape Coast, Ghana

[3] Department of Physics, University of Cape Coast, Ghana

Correspondence: Samuel Sonko Sackey, Laser and Fibre Optics Centre, Department of Physics, University of Cape Coast, Ghana. E-mail: samuel.sackey@ucc.edu.gh

Received: October 3, 2017 Accepted: October 20, 2017 Online Published: November 10, 2017

doi:10.5539/apr.v9n6p36 URL: https://doi.org/10.5539/apr.v9n6p36

Abstract

Well-water contaminated by microbial bacteria has been purified using LEDs radiating in the ultra-violet and visible spectral regions. The contaminated water sample was exposed to the LEDs in specially constructed chambers and the purification process carried on for 3 days. The efficiency of the process was determined using a 445 nm diode laser to induce fluorescence (LIF) and the monitoring of coliform bacteria count (Total coliform, Fecal coliform and *Escherichia coli*) as well as Total Heterotrophic Bacteria (THB). The LIF peak fluorescence intensities at 526 nm (Raman water peak) and dissolved organic matter fluorescence intensity at 550 nm were determined. Using the fluorescence intensity of purified drinking water as reference, a fluorescence intensity ratio was calculated. A decrease in this ratio with time, at the two wavelengths indicated a proof of purification. Using the values of the slopes, the red and green LEDs proved most efficient while the UV was the least. From the counts of coliform bacteria and THB, the light sources registered zero after the first day of purification, but counts were recorded thereafter for some of the bacterial for some light sources. This may be attributable to bio-films formation on internal surfaces of the purification chamber due to excessive temperatures. A reduction in fluorescence intensity observed in the sample stored in dark environment could be attributed to the stationary and logarithmic-decline phases of the growth curve of bacterial population. This purification technique is inexpensive and can easily be adapted for domestic water purification for reducing waterborne bacteria.

Keywords: coliform bacteria, *Escherichia coli*, laser induced fluorescence, microbial purification, total heterotrophic bacteria, ultra-violet and visible spectral regions

1. Introduction

Water is associated with life, and indeed needed by all living things for survival. Its deficiency in active cells results in dehydration and has caused many deaths and adverse health situations. Its quality is a powerful determinant of good health, and has therefore gained a critical attention. This is because it is often contaminated by micro-organisms such as pathogenic enteric bacteria, viruses, intestinal parasites and other unwanted chemical substances leading to a reduction in its quality. Water of poor quality is a health hazard, with the most predominant waterborne disease, diarrhea, having an estimated annual incidence of 4.6 billion episodes and causing 2.2 million deaths every year. It results in malnutrition, weakness, and an increase in vulnerability to diseases which can be life threatening. In Africa, about 42% of healthcare providers do not have access to clean water, while globally, 663 million people (about 10%) do not have access to safe drinking water (WHO/UNICEF JMP Report, 2015). If authorities do not take measures to resolve such fundamental human need for safe and portable water, about 135 million people will die from water-related diseases by 2020 (Gleick, 2002).

The wholesomeness of water means absence of suspended solids, inorganic solids and pathogens which are disease-causing organisms. Ideally, water must contain only its molecules without any contaminants. The Safe Drinking Water Act defined contaminant as any physical, chemical, biological, or radioactive substance or matter present in water (Contaminant Candidate List, 2016). The exponential growths in the population of most

developing countries have put pressure on the quality of water sources due to the rise in waste production without the requisite increase in waste management techniques and facilities to handle the situation.

Ghana is endowed with water resources from rainfall, surface water (rivers, lakes, ponds and streams) and groundwater sources (springs and wells), but the latter has proved to be cost-effective and a long-lasting source of water supply. This has led to the drilling of over 10,000 boreholes and over 45,000 hand-dug wells in the country. 50% of the entire population use water from groundwater sources while the rural communities, which form about 70% of the total population, rely mostly on groundwater source for all chores (ISODEC, 2011).

One way of assessing the quality of groundwater is by monitoring dissolved organic matter (DOM) as its concentration can reflect the possibility of contamination (Leenheer et al., 1974; Barcelona, 1984). Humic and fulvic acids of DOM affect the solubility of organic pollutants in groundwater and can contribute to the long-range transport of harmful chemicals (Chiou et al., 1986) which in groundwater can lead to production of carcinogenic disinfection byproducts (DBPs) during drinking water treatment (Singer, 1994; Chomycia et al., 2008). According to Tebbute (1992), traces of pathogenic organisms are found in groundwater as a result of poor well-construction techniques which are associated with bedrock aquifers in which large openings afford direct connection between the surface and groundwater

Poorly constructed, cracked or unsealed wells can provide an avenue for coliform bacteria to enter groundwater. Coliform bacteria are a group of microorganisms found in soils, surface water and on plants, but can be washed into groundwater by rain. Such bacteria are used as pointers in water tests as their presence indicates that pathogens could also be in the water. Analysis is conducted for three different groups of coliform bacteria, with each having a well-defined level of risk to human health. Total coliform bacteria are generally harmless and may have the environment as its source. Fecal coliform bacteria (sub-group of total coliform bacteria) appear in great quantities in the feces of people and animals. *Escherichia coli* (*E. coli*) are found in great quantities in the intestines of warm-blooded animals including humans. Some strains can cause illness, and their detection indicates fecal contamination of a well and poses a high risk for illness from disease-causing organisms (Coliform Bacteria, 2016; Water Fact Sheet, 2009). The regular monitoring and testing for coliform bacteria in groundwater is necessary to ensure the supply of safe water to consumers.

Another quality assessment considered an accessory indicator in the measurement of coliform in water is the heterotrophic plate count (HPC). This is an aerobic-anaerobic bacteria test used for monitoring general bacteriological water quality, but cannot be used in fecal contamination test (Hsu et al., 1995). Heterotrophic bacteria are not indicators of pathogenic conditions, but can cause infections in skin, lung and gastroenteritis (Bartram et al., 2003; Chopra & Houston, 1999, Helmer et al., 1997). Heterotrophic bacteria are present in all water types (Foulquier et al., 2011; Griebler & Lueders, 2009) and drinking water treatment does not remove or inactivate all heterotrophic organisms. Some are resistant because they may be in a spore or vegetative form with an impervious membrane, or may be protected from treatment as part of an aggregate (Geldreich, 1996). Their concentration in water varies from less than 1 CFU/ml (colony forming unit per milliliter) to over 10000 CFU/ml (Payment, 1999; Pepper et al., 2004; Stine et al., 2005) and depends on temperature and the amount of absorbable organic material. The maximum permissible level of heterotrophic bacteria in potable water is 500 CFU/ml (Amanidaz et al., 2015). In groundwater, under the direct influence of surface water, their concentrations can be highly variable. Such variations can be sudden or gradual over time and may indicate a change in water quality.

Water purification techniques which aim at removing all contaminants in order to make it safer for use have existed, while new and more efficient ones have recently been discovered and employed. Some basic purification methods in use include filtration (eliminates most of suspended particles), oxygenation (allows atmospheric oxygen to dissolve in the water killing microbes), solar disinfection, chlorination and reverse osmosis. Some of these techniques may be expensive and saddled with disadvantages. Chlorination water treatment, for instance, leaves behind disinfection by-products (DBPs) which may have adverse birth defects and outcomes and causes bladder cancer (Villanueva et al., 2006).

Purification using light sources involves exposing organism in contaminated water to radiations mainly within the ultra-violet (UV) and visible (Vis) parts of the electromagnetic spectrum. This results in inactivating both pathogenic and non-pathogenic bacteria (Hamamoto et al., 2007) as the rays strike and penetrates the outer cell membrane, going through the cell body and disrupting the DNA -preventing reproduction (Here, nothing is being added except the energy which does the killing). Such radiation has the potential of causing destruction to a lot of bacteria species; mold spores, algae, virus, and yeast based on the dose of energy delivered to the organism by the radiation and do not form any significant DBPs (Oppenheimer et al., 1997). With respect to the use of light sources, LEDs are preferred and have been receiving tremendous attention amongst researchers over the past few years.

They use electricity more efficiently, do not require any warm up-period and it is possible to adjust their wavelengths to supply desirable radiations (Jo, 2013; Nelson et al., 2013; Crook, 2011; Vilhunen et al., 2011). UV LEDs in particular are used to inactivate chlorine-resistant pathogens within a relative short contact time without producing undesirable DBPs during water treatment (Ibrahim et al., 2013; Bowker et al., 2011; Crawford et al., 2005).

Simple and non-destructive spectroscopic methods using various light sources have been shown to be useful in the structural and functional studies of DOM (Chin et al., 1994). Lasers and LEDs have been used for disinfection in water (Adeboye, 2014; Gondal et. al., 2009; Copa & Gitchel, 1981) while induced fluorescence using these same sources (LIF for lasers) have been used to estimate water pollution and probe the composition of DOM in watersheds (Sharikova, 2009).

The objective of this study is to assess the efficiency of purification in groundwater harvested from a heavily patronized hand-dug well located near the University of Cape Coast by determining its fluorescence spectra and measuring the count of coliform bacteria (Total coliform, Fecal coliform and *Escherichia coli*) and Total Heterotrophic Bacteria (THB) before and after treating with different LED sources within the UV-Vis spectral regions. The extent of purification using each source is also analyzed.

2. Materials and Methods

2.1 Study Area

The University of Cape Coast is located in the Central Region of Ghana (05°06′00″N, 01°15′00″W) with no elevation above sea level. Within the immediate environs of the University is Amamoma, a settlement where a large number of the students of the university live. Availability of water is usually a problem in Cape Coast and its environs and therefore most inhabitants tend to rely on hand-dug wells for their daily chores. Figure 1 is a composite figure in which (a) is a map of Ghana highlighting the Central Region, (b) shows the study area Amamoma and (c) shows area details within Amamoma indicating the investigated well.

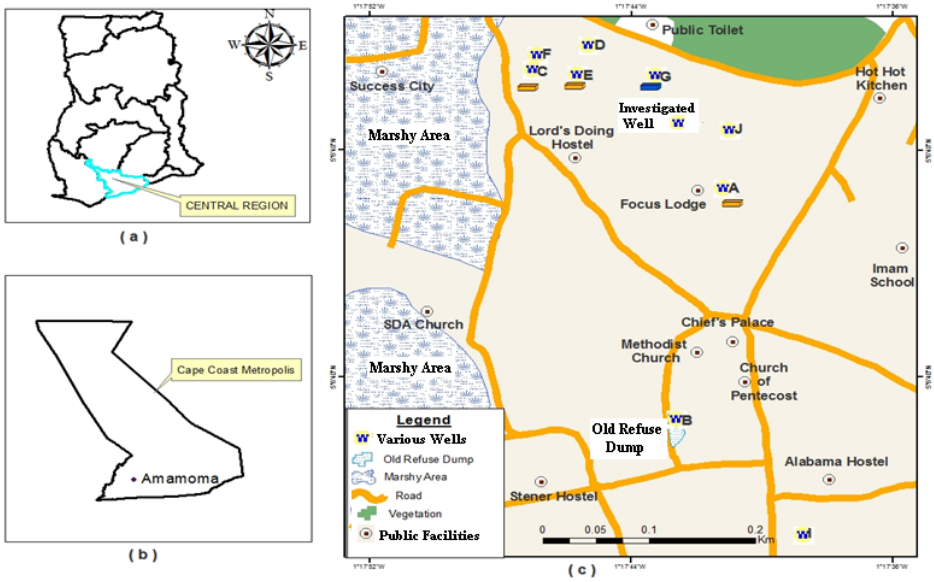

Figure 1. (a) Map of Ghana highlighting the Central Region, (b) Study area Amamoma, (c) Details within Amamoma showing the investigated

2.2 Microbiological Experimental Procedure

Using the Ghana Standards Authority guidelines (Ghana Standards Authority, 2009), the pour-plate technique was used to analyse the sample for coliform bacteria (Total coliform, Fecal coliform and *Escherichia coli*) and Total Heterotrophic Bacteria (THB) all in CFU per mL. The samples were collected into sterilized plastic containers before noon, kept under ice and transported to the laboratory for processing within a few hours of collection. Culture media (Plate Count Agar [Oxoid Ltd., Hampshire, England] and Eosin Methylene Blue Agar [Oxoid Ltd., Hampshire, England]) were prepared according to the manufacturer's instructions and sterilized at 121°C, 15 psi for 15 minutes. Each sample was shaken vigorously and the area around the lid of the bottle wiped with clean tissue soaked with 70% ethanol (Aseptic technique).

Duplicate dilutions of 0.1 mL and 1 mL of each sample were inoculated on plate count agar using the spread and pour plate technique respectively and incubated at 37°C for 48 hours. All colonies were counted, and an average of duplicate samples recorded as THB counts/mL (CFU/milliliter) for the sample.

Similarly, 2 duplicate dilutions of 0.1 mL and 1 mL of each sample were plated on Eosin Methylene Blue agar and one incubated at 37°C for 48 hours to observe for TC and the other duplicate incubated at 44°C for 48 hours to observe for FC. All purple colonies were counted, and an average of duplicate samples recorded as TC and FC counts/mL (CFU/mL), respectively for the sample.

For *Escherichia coli* each of the presumptive colonies (metallic green sheen colonies on the FC) was sub-cultured in 10 mL of Peptone Water (Oxoid) for biochemical testing. Each colony was grown in peptone water and incubated at 44°C for 24 hours. A drop of Kovac's reagent was then added to the tube of peptone water. All the tubes showing a red ring color development after gentle agitation indicated the presence of indole and recorded as a confirmation of *Escherichia coli.* All colonies of that morphological type were then enumerated and recorded.

2.3 Overview of Construction of Purification Chamber and Optical System Used

2.3.1 Purification Chamber

A vacuum thermos flask (1 liter volume) was used as the purification chamber and was chosen because it could provide and ensure an efficient and easily-maintained system. A glass tube was driven through a rubber cork and LED arranged on strips wound round the tube. The terminals of the LED were passed through the rubber cork. A specially fabricated white glass tube made of quartz was then lowered to the base of the cork to serve as an outer shield to protect the LED. This is as shown in Figures 2a and 2b. The shielded LED on the glass tube was then lowered into a flask, which served as the purification chamber, as shown in Figure 2c. The material used to protect the LED needed to be transparent in the UV-Vis spectral regions. A white quartz glass, which is transparent in the visible region, was therefore used as a previous study had confirmed its transparency in the UV region (Sackey et. al., 2015).

2.3.2 Design Involving LEDs

Five different LEDs (green, red, ultra-violet, white and blue) along with five flasks respectively were used. The reflecting inner surface of the flask ensured an even distribution of light while at the same time confining the heat generated within the purification environment. The LEDs were powered by a 12 V DC supply. Figure 2b shows the powered LEDs.

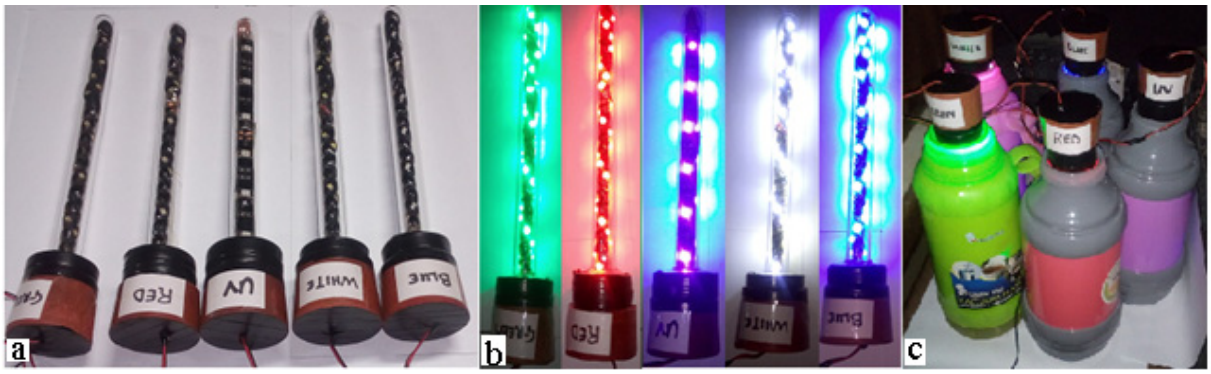

Figure 2: (a) Fabricated tube showing the LED's housed and protected within the quartz glass material. (b) The various LED's powered. (c) The individual purification chambers for the various LED's

2.4 Laser Induced Fluorescence (LIF) Set-up

A Laser induced fluorescence (LIF) set-up was used to monitor and analyze the DOM content of the water samples (the well-water and natural drinking water used as reference) before and after exposure, which was carried out for a period of three (3) days, with measurements being carried out after every 24 hours. The experimental set-up is as shown in Figure 3. It consists of a diode laser source emitting at 445 nm, a detector mounted perpendicular to the laser and an optical fiber cable that couples light from the detector into the spectrometer. A computer was used for data collection and analysis.

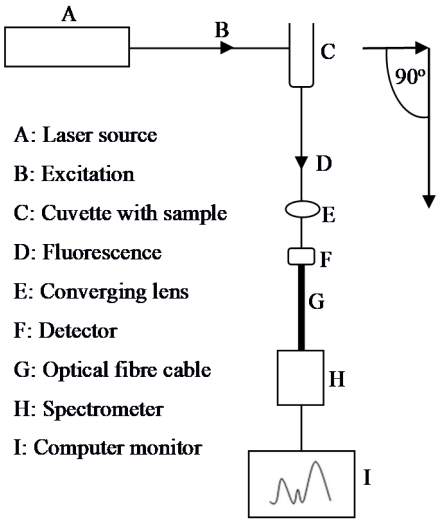

Figure 3. LIF setup for DOM measurements

3. Results and Discussions

The spectra of the LEDs used were first taken using a USB 4000 spectrometer to determine the wavelength at which they each exhibited their maximum intensities. The graphs for their normalized spectra are shown in Figure 4.

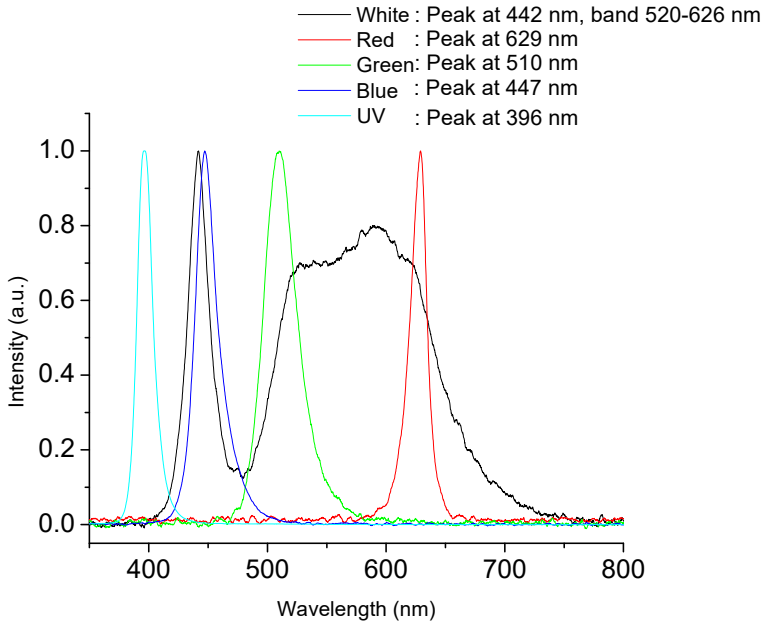

Figure 4. Normalized spectral emissions of the different LED sources used

3.1 Temperature Analysis on Purification Chamber

Two distinctive analyses involving temperature were carried out on each of the purification chambers. The first was a study conducted before the commencement of the purification process to determine the rate of heat loss from each flask. This was done by filling each flask with water at a temperature of 95^0C, and the temperature measured after every hour for 4 hours. The temperature variations, which are represented in the vertical column graph in Figure 5, indicate a similar rate of heat loss for all 5 purification chambers. The second analysis involved a determination of the temperature within the purification chamber each time data was to be collected. As expected, the LEDs warmed-up with time; therefore this measurement provided the temperature of the sample at each time of measurement. The findings of these measurements for each LED are represented in Figure 6. The initial temperature reading for all the samples was 27^0C.

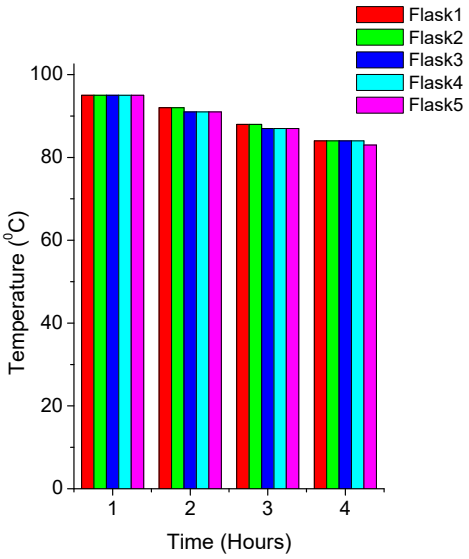

Figure 5. Temperature variations with time within each purification chamber indicating similar rate of heat loss for all 5 flasks from an initial temperature of 95^0C

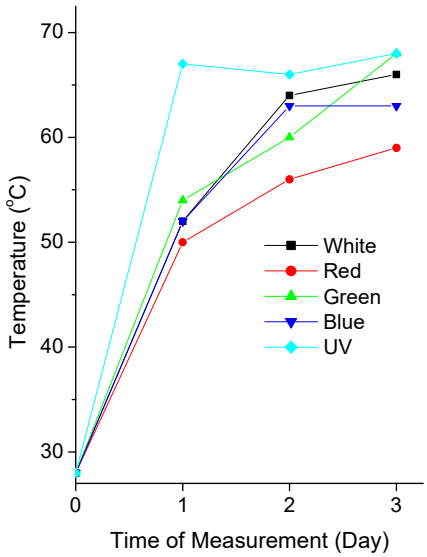

Figure 6. Variations in temperature within the purification chamber for the various LEDs each time data was collected

3.2 LIF DOM Measurements

The LIF from the samples were determined for each light source used and for the 3 days of purification. Figure 7 is a composite graph showing the LIF after each day of purification. For each plot, a comparison is made with the natural drinking mineral water (represented as 'purified') and the original non-purified water sample (represented by 'NT'). The plot labeled 'Dark' is for the control untreated sample kept in a completely dark environment throughout the study period.

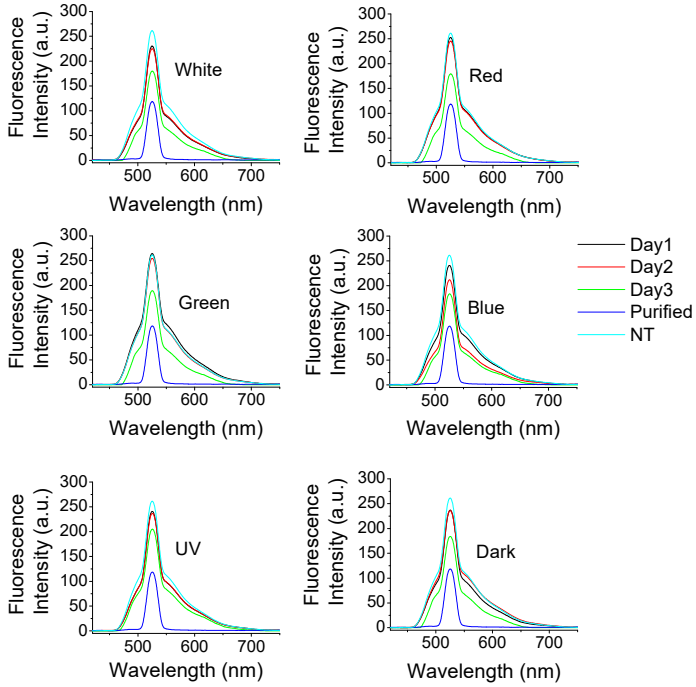

Figure 7. Composite graph showing the LIF of the samples after purification using the various LEDs and comparing with the natural drinking mineral water ('purified') and the original non-treated water sample kept in a completely dark environment ('NT')

Comparing the plots with the plot for natural drinking mineral water (purified), it is noticed that both the peak fluorescence intensity at 526 nm (Raman water peak) and DOM fluorescence intensity at 550 nm reduced from Day 1 to Day 3 for all the LEDs used. This can be assigned to photo-degradation. Additionally, it will be noticed that the fluorescence intensity for the sample stored in the dark environment (control) also decreased with time, meaning that something else aside the photo-degradation was taking place. This observation has been explained under section *3.3: Analysis Based on Colony formation before and after purification.* There was no shoulder observed on the graph for the natural drinking water (purified) at 550 nm and can be assigned to the fact that the natural drinking water has no DOM. DOM are only observed for contaminated water samples and was therefore only observed for the water samples collected from the well.

Using the fluorescence intensity of the purified drinking water as reference, a fluorescence intensity ratio (FIR) was calculated after each day of purification and for each light source at 526 nm and 550 nm. This was calculated using the equation below.

$$FIR = \frac{FI_S}{FI_{NDW}}$$

where FI_S is the fluorescence intensity of the sample at a given time (Day) of purification, for a given LED and emission wavelength (526 nm or 550 nm), and FI_{NDW} is the fluorescence intensity of the natural drinking mineral water which was used as the reference. Figure 8 is a composite graph for the variation of the FIR for the different LEDs with time. Figure 8a represents the ratios at 526 nm while Figure 8b represents the ratios at 550 nm.

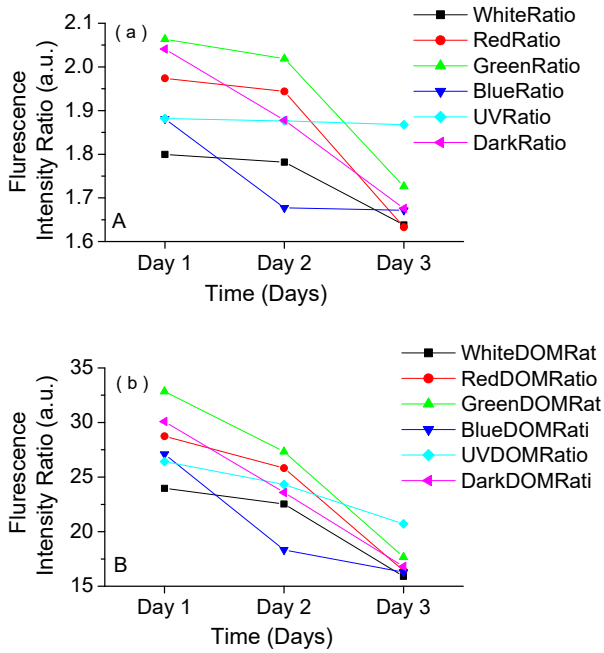

Figure 8. Changes in fluorescence intensity ratios for the different LEDs with time at (a) 526 nm and (b) 550 nm

It is clear from Figure 8 that the DOM substances in the water sample appear to be more sensitive to the visible light sources than the UV light source and therefore photo-degradation was more pronounced with the visible light sources. Generally, the fluorescence intensity ratios (FIR) calculated for the various light sources at 526 nm and 550 nm decreased with time and indicates an improvement in the quality of the water and a confirmation of some purification. Using the data obtained from the FIR, a line of best fit was drawn, a linear equation established for each light source (526 nm and 550 nm) and the slope of each line determined and used as an indicator of the rate and efficiency of purification. Higher slope values indicated a faster and more efficient purification process. Table 1 gives the values of the slopes extracted from Figure 8 and the ranking for the LEDs at 526 nm and 550 nm.

Table 1. Slope values and ranking of the LEDs at 526 nm and 550 nm respectively

Fluorescence Intensity Ratios at 526 nm		
LEDs	Slope	Ranking using slope
White	- 0.08067	4
Red	- 0.17032	1
Green	- 0.16854	2
Blue	- 0.10463	3
UV	- 0.00715	5
Fluorescence Intensity Ratios at 550 nm		
LEDs	Slope	Ranking using slope
White	- 4.02791	4
Red	- 6.16064	2
Green	- 7.58613	1
Blue	- 5.40900	3
UV	- 2.85325	5

It can be deduced that at both 526 nm and 550 nm, the red and green LEDs proved most efficient in the DOM purification process, while the UV was the least efficient. This observation made with respect to the UV conforms to a previous study that drinking water purification using UV LEDs is not an efficient technique (Adeboye, 2014).

3.3 Analysis Based on Colony Formation before and after Purification

There was a count of coliform bacteria (Total coliform, Fecal coliform and *Escherichia coli*) and Total Heterotrophic Bacteria (THB) before purification and a regular periodic count on a daily basis. These counts, as measured in Colony Forming Unit per milliliter CFU/ml, before purification (NT) and for the 3 days of purification using the various light sources, are presented in Table 2. The count for the sample stored in the dark is also presented.

Table 2. Microbial Population (CFU/ml) before and after purification with the various light sources and for the 3 days of treatment

Microbial Population (CFU/ml) after Day 1 purification using the LEDs							
	Raw Sample		LED Treated				
	NT	Dark	White	Red	Green	Blue	UV
TC	1.20×10^3	5.78×10^2	NG	NG	NG	NG	NG
FC	1.60×10^3	8.80×10^1	NG	NG	NG	NG	NG
E.coli	4.90×10^1	NG	NG	NG	NG	NG	NG
THB	2.70×10^3	2.50×10^3	NG	NG	NG	NG	NG
Microbial Population (CFU/ml) after Day 2 purification using the LEDs							
TC	1.20×10^3	1.09×10^2	NG	1.10×10^1	NG	NG	9.80×10^1
FC	1.60×10^3	8.90×10^1	NG	NG	9.00×10^0	NG	4.60×10^1
E.coli	4.90×10^1	2.10×10^1	NG	NG	1.30×10^1	NG	9.00×10^0
THB	2.70×10^3	6.80×10^1	4.00×10^0	5.00×10^0	7.90×10^1	2.00×10^0	1.00×10^0
Microbial Population (CFU/ml) after Day 3 purification using the LEDs							
TC	1.20×10^3	2.10×10^1	NG	NG	NG	NG	NG
FC	1.60×10^3	7.60×10^1	NG	NG	NG	NG	NG
E.coli	4.90×10^1	3.00×10^0	NG	NG	NG	NG	NG
THB	2.70×10^3	3.86×10^2	2.00×10^0	8.00×10^0	NG	NG	2.00×10^0

NT - Counts before purification, TC - Total Coliform, FC - Fecal Coliform, *E.coli* -*Escherichia coli*

THB - Total Heterotrophic Bacteria, NG - No Growth

According to the Canadian Drinking Water Quality Guideline (Facts on Drinking Water, 2016) the maximum acceptable level for fecal coliform, total coliforms and *E.coli* are 'none detectable per 100 mL'. This simply means that for every 100 mL of drinking water tested, no coliforms should be detected. As shown in Table 2, all the light sources registered a reduction to zero (0) count after Day 1 of purification in all the measured coliform and bacteria studied. Some counts were, however, recorded after Day 2 and 3 of purification for some of the light sources for some of the coliform and bacterial studied. It is known that purification effectiveness is a function of the contact time and an increase in temperature beyond the value appropriate for drinking water influences the rate of purification reactions.

Temperatures exceeding the required temperature might have led to the formation of bio-films on internal surfaces (Ainsworth 2004). Bio-films are known to contain several living heterotrophic bacteria, fungi, protozoa, nematodes and crustaceans. It can be deduced from the temperature graph in Figure 6 that the temperature within the purification chamber increased after Day 1 and could be the reason for the observed counts thereafter. Also the microbial re-growth observed at the end of Day 2 may be due to the organic matter present in the water samples (as depicted in Figure 8b).

With respect to the control sample it will be observed that although it was kept in a dark environment there was a reduction in all the counts with time after Day 1. This means that other phenomenon aside photo-degradation might be taking place. According to a study (Tortora, Funke, & Case, 2010), bacterial populations follow a sequential series of growth phases; the lag, exponential growth, stationary and logarithmic-decline. The observed reduction may be attributed to the stationary and logarithmic-decline phases of their growth curve. At the later stage of the stationary phase, increased cell density often causes an accumulation of organic acids and other toxic bio-chemicals as a result of depletion of nutrients and oxygen. In the logarithmic decline phase, limiting factors intensify and the population shows a decline leading to some cells going into dormancy although they remain viable but do not grow. Some cells enter a starvation mode that helps them resist the lack of nutrients (Talaro & Chess, 2015).

4. Conclusion

In this study, the use of LEDs radiating in the ultra-violet and visible spectral regions for the purification of hand-dug well-water samples have been demonstrated to have a great potential. The UV LED radiated at 396 nm while the visible LEDs, blue, green, red and white radiated at peak wavelengths of 447 nm, 510 nm, 629 nm and 442 nm respectively. The white LED also exhibited a broad band ranging from 520 nm and 626 nm. The purification was carried out for three (3) days in specially constructed chambers, and the efficiency and quality of purification periodically monitored using two techniques: laser-induced fluorescence spectroscopy and bacteria and Total Heterotrophic Bacteria count. The laser-induced fluorescence of the samples was determined for each light source and the peak fluorescence intensities at 526 nm (Raman water peak) and DOM fluorescence intensity at 550 nm determined. Using the fluorescence intensity of purified drinking water as reference, the fluorescence intensity ratio was calculated at these two wavelengths after each day of purification and for each light source.

The decrease in the fluorescence intensity ratio with time at the two wavelengths for the various light sources generally indicated the extent of photo-degradation of the water samples, characterized by the slope of the line. The steeper the slope the greater is the rate and extent of photo-degradation. Comparing the values of the slopes at both wavelengths, it was clear that the red and green LEDs proved most efficient in the degradation process, while the UV was the least efficient due to the characteristics of the DOM.

Samples were taken before and after exposure to the LEDs and were analyzed with culture techniques. A reduction in the coliform bacteria and Total Heterotrophic Bacteria counts was observed throughout the study. In particular, counts reduced to zero after the first day of irradiation for all light sources, after which microbial re-growths was observed for some light sources. We posit that this re-growth may be due to the presence of some DOM remaining and subsequent over-heating may have led to the formation of bio-films within the water samples. The sample stored in a dark environment also exhibited a reduction in its fluorescence intensity and coliform bacteria and Total Heterotrophic Bacteria counts with time. The observed reduction may be attributed to the stationary and logarithmic-decline phases of the growth curve of bacterial population where the intensification of limiting factors leads to a population decline.

Light radiation based water purification has a great potential as nothing is added except the energy which does the killing of the bacteria and therefore does not form any purification by-products. This technique is therefore amendable for domestic water purification as it is easy to use, inexpensive and dependable for reducing waterborne pathogens.

References

Adeboye, M. O. (2014). *Disinfection of Escherichia Coli in Water Using Ultraviolet LEDs* (Master thesis, University of Eastern Finland, Finland).

Amanidaz, N., Zafarzadeh, A., & Mahvi, A. H. (2015). The Interaction between heterotrophic bacteria and coliform, fecal coliform, fecal Streptococci bacteria in the water supply networks. *Iranian journal of public health*, *44*(12), 1685-1692.

Barcelona, M. J. (1984). TOC Determinations in Ground Water. *Ground Water, 22*, 18–24. https://doi.org/10.1111/j.1745-6584.1984.tb01471.x

Bartram, J., Cotruvo, J. A., Exner, M., Fricker, C., & Glasmacher, A. (Eds.). (2003). *Heterotrophic plate counts and drinking-water safety*. IWA publishing.

Bowker C., Sain A., Shatalov M., & Ducoste J. (2011). Microbial UV fluence-response assessment using a novel UV- LED collimated beam system. *Water Research, 45*, 2011-2019. https://doi.org/10.1016/j.watres. 2010.12.005

Cape Coast. (2017). In *Wikipedia, the free encyclopedia*. Retrieved June 6, 2017, from https://en.wikipedia.org/wiki/Cape_Coast

Chin, Y. P., Aiken, G. R., & O'Loughlin, E. (1994). Molecular weight, polydispersity and spectroscopic properties of aquatic humic substances. *Environ. Sci. Technol., 28*, 1853-1858. https://doi.org/10.1021/es00060a015

Chiou, C. T., Malcolm, R. L., Brinton, T. I., & Kile, D. E. (1986). Water solubility enhancement of some organic pollutants and pesticides by dissolved humic and fulvic acids. *Environ Sci Technol, 20*(5), 502–508. https://doi.org/10.1021/es00147a010

Chomycia, J. C., Hernes, P. J., Harter, T., & Bergamaschi, B. A. (2008). Land management impacts on dairy-derived dissolved organic carbon in ground water. *J Environ Qual, 37*(2), 333–343. https://doi.org/10. 2134/jeq2007.0183

Chopra, A. K., & Houston, C. W. (1999). Enterotoxins in Aeromonas-associated gastroenteritis. *Microbs Infect., 1*(13), 1129–1137. https://doi.org/10.1016/S1286-4579(99)00202-6

Coliform Bacteria, 2016, DOH 331-181 Revised. (2016). Retrieved from http://www.doh.wa.gov/portals/1/ Documents/Pubs/331-181.pdf

Contaminant Candidate List.（2016). Retrieved from https://www.epa.gov/ccl/definition-contaminant

Copa, W. M., & Gitchel, W. B. (1981). *U.S. Patent No. 4,265,747*. Washington, DC: U.S. Patent and Trademark Office.

Crawford, M. H., Banas, M. A., Rose, M. P., Ruby, D. S., Nelson, J. S., Boucher, R. & Allerman A. A. (2005). *Final LDRD report: ultraviolet water purification systems for rural environments and mobile applications*. Mexico and California: Sandia National Laboratory. SAND2005-7245.

Crook, M. J. (2011). *A comparative study into disinfection efficiency of traditional UV and UV-LEDs*. Cranfield University.

Facts on Drinking Water. (2016). Retrieved from http://www2.gnb.ca/content/dam/gnb/Departments/h-s/pdf/en/HealthyEnvironments/water/Coliforme.pdf

Foulquier, A., Mermillod-Blondin, F., Malard, F. & Gilbert, J. (2011). Response of sediment biofilm to increased dissolved organic carbon supply in groundwater artificially recharged with stormwater. *J. Soils Sediments, 11*, 382-393. https://doi.org/10.1007/s11368-010-0323-2.

Geldreich, E. E. (1996). *Microbial quality of water supply in distribution systems*. Florida: CRC Press, Inc..

Ghana Standards Authority. (2009). *Water Quality Specification for Drinking, GS 175-1:2009*.

Gondal, M. A., Dastageer, M. A., & Khalil, A. (2009). Synthesis of nano-WO 3 and its catalytic activity for enhanced antimicrobial process for water purification using laser induced photo-catalysis. *Catalysis Communications*, *11*(3), 214-219. https://doi.org/10.1016/j.catcom.2009.10.011.

Griebler, C., & Lueders, T. (2009). Microbial biodiversity in groundwater ecosystems. *Freshwater Biol., 54*, 649-677. https://doi.org/10.1111/j.1365-2427.2008.02013.x.

Hamamoto, A., Mori, M., Takahashi, A., Nakano, M., Wakikawa, N., Akutagawa, M., ... & Kinouchi, Y. (2007). New water disinfection system using UVA light-emitting diodes. *Journal of applied microbiology*, *103*(6), 2291-2298.

Hamamoto, A., Mori, M., Takahashi, A., Nakano, M., Wakikawa, N., Akutagawa, M., ... & Kinouchi, Y. (2007). New water disinfection system using UVA light-emitting diodes. *Journal of applied microbiology*, *103*(6), 2291-2298. https://doi.org/10.1111/j.1365-2672.2007.03464.x

Helmer, R., Hespanhol, I., Supply, W., Council, S. C., Organization, W. H., & Press, C. (1997). *Water pollution control: a guide to the use of water quality management principles* (pp. 400–402). https://doi.org/10.4324/ 9780203477540

Hsu, F-C., Shieh, Y., Van-Duin, J., Beekwilder, M., & Sobsey, M. D. (1995). Genotyping male-specific RNA coliphages by hybridization with oligonucleotide probes. *Appl. Environ Microb, 61*, 3960–3966.

Ibrahim, M. A. S., MacAdam, J., Autin O., & Jefferson, B. (2014). Evaluating the impact of LED bulb development on the economic viability of ultraviolet technology for disinfection. *Environmental Technology for Disinfection, 35*(4), 400-406. https://doi.org/10.1080/09593330.2013.829858

Jo, W. K. (2013). Purification of aromatic hydrocarbons via fibrous activated carbon/photocatalytic composite coupled with UV light-emitting diodes. *Environmental Technology, 34*, 1175-1181. https://doi.org/10.1080/09593330.2012.743591. PMid:24191450.

Leenheer, J., Malcolm, R., McKinley, P., & Eccles, L. (1974). Occurrence of dissolved organic carbon in selected ground-water samples in the United States. *J Res US Geol Surv, 2*, 361–369.

Ministry of Health (MOH). (1999). *Medium term Health Strategy towards Vision 2020*. Ministry of Health, Accra, Ghana.

Nelson, K. Y., McMartin, D. W., Yost, C. K., Runtz, K. J., & Ono, T. (2013). Point-of-use water disinfection using UV light-emitting diodes to reduce bacterial contamination. *Environmental Science and Pollution Research*, *20*(8), 5441-5448. https://doi.org/10.1007/s11356-013-1564-6

Oppenheimer, J. A., Jacangelo, J. G., Laine, J-M., & Hoagland, J. E. (1997). Testing the equivalency of ultraviolet light and chlorine for disinfection of wastewater to reclamation standards. *Water Environ. Res., 69*, 14–24. https://doi.org/10.2175/106143097X125137

Payment, P. (1999). Heterotrophic bacteria. In *AWWA manual of water supply practices* (pp. 83-87). AWWA M48. Waterborne pathogens. American Water Works Association, Denver, Colorado.

Pepper, I. L., Rusin, P., Quintanar, D. R., Haney, C., Josephson, K. L., & Gerba, C. P. (2004). Tracking the concentration of heterotrophic plate count bacteria from the source to the consumer tap. *Int. J. Food Microbiol., 92*, 289-295. https://doi.org/10.1016/j.ijfoodmicro.2003.08.021

Piper, A. M. (1994). A graphic procedure in the Geochemical interpretation of water analyses. *Am. Geophys. Un. Trans., 25*, 914–923.

Richard, A. (2004). Safe piped water: Managing microbial water quality in piped distribution systems (pp. 25–130). *World Health Organization (WHO)*.

Sackey, S. S., Vowotor, M. K., Owusu, A., Mensah-Amoah, P., Tatchie, E. T., Sefa-Ntiri, B., Hood, C. O., Atiemo, S. M. (2015). Spectroscopic Study of UV Transparency of Some Materials. *Environment and pollution, 4*(4). https://doi.org/10.5539/ep.v4n4p1

Sharikova, A. V. (2009). UV laser and LED induced fluorescence spectroscopy for detection of trace amounts of organics in drinking water and water sources. Graduate Theses and Dissertations. Retrieved from http://scholarcommons.usf.edu/etd/15

Singer, P. C. (1994). Control of disinfection by-products in drinking water. *J Environ Eng, 120*(4), 727–744. https://doi.org/10.1061/(ASCE)0733-9372(1994)120:4(727)

Stine, S. W., Pepper, I. L., & Gerba, C. P. (2005). Contribution of drinking water to the weekly intake of heterotrophic bacteria from diet in the United States. *Water Res., 39*, 257-263. https://doi.org/10.1016/j.watres.2004.09.010

Tebbute, T. (1992). Sustainable Water Development: Opportunities and Constraints Water Int., 13, 189.

Vilhunen S., Särkkä H., & Sillanpää, M. (2009). Ultraviolet light-emitting diodes in water disinfection. *Environmental Science and Pollution Research, 16*, 439-442. https://doi.org/10.1007/s11356-009-0103-y

Villanueva, C. M., Cantor, K. P., Grimalt, J. O., Malats, N., Silverman, D., Tardon, A., ... & Marcos, R. (2006). Bladder cancer and exposure to water disinfection by-products through ingestion, bathing, showering, and swimming in pools. *American journal of epidemiology*, *165*(2), 148-156. https://doi.org/10.1093/aje/kwj364

WHO/UNICEF. (2015). WHO/UNICEF Joint Monitoring Programme (JMP) Report 2015.

Applied Physics Research; Vol. 9, No. 6; 2017
ISSN 1916-9639 E-ISSN 1916-9647
Published by Canadian Center of Science and Education

The Periodic Table Possible Coincided with an Unfolded Shape of Atomic Nuclei

Jianping Mao[1]

[1] 201-A-22 Qinye Changzhou, Jiangsu 213016, China

Correspondence: Jianping Mao. E-mail: mjp00951@163.com

Received: October 11, 2017 Accepted: October 26, 2017 Online Published: November 10, 2017

doi:10.5539/apr.v9n6p47 URL: https://doi.org/10.5539/apr.v9n6p47

Abstract

The periodic table seems to correspond to folding nuclei, a visible proton (nucleon) distribution, that can grow vertical 4 *a* (representative), 4 *b* (transition), and 8 *c* (inner transition) axes (α-clusters) bound with valence neutrons standing a core (1st period) of likely expanding in Co, Ni, Rh, and Pd, which was naturally within proton and neutron drop lines, and roughly able to fit in with nuclear fission phenomena, including α-cluster decay. It was observed in analysis molecular structures that crosses nuclear, atomic, and molecular three levels, which provides a convenient way that will enable the nature of the periodic table promisingly to become easier understanding.

Keywords: periodic table, proton distribution, valence neutron, folding nuclei, nuclear core, nuclear fission.

1. Introduction

The periodic table with the elements accumulated today is well-known and plays a basic role in physical science. Its nature (shape, *Z*, the atomic number) that is bewildering was traditionally explained by Bohr (1913), an atomic periodicity, though about in the meantime it has been proven to result from the proton number (Moseley, 1913). This seems possible to attribute to that a real cubic distribution of *Z* in a nucleus might have not been revealed (Bohr & Wheeler, 1939), to the author's knowledge. However, it may be a flaw to pay little attention on the proton number that could convey a nuclear periodicity to some extent. For example, magic nuclei 2, 8, 20, 28, 50, 82, and 126 (Haxel, Jensen, & Suess, 1949) are almost inconsistent with noble nuclei (gases) 2, 10, 18, 36, 54, 86, and 118, while noble nuclei appear to close naturally that can display a cubic *Z*.

It was observed in analysis molecular structure starting from a curiosity that whether an atomic mass has an influence upon molecular bond energy about in the summer of 1987. Because an element occurs some isotopes and then had no intention of taking their relative mass what want to see nucleons how to distribute in a molecule (atom), every element is represented by its maximal abundant isotope selected from U.S. *National Nuclear Data Center*, (Nudat 2). Actually, it was an integrative result of atomic dot structure of Lewis, (1916) and nuclear alpha particle model (Hafstod & Teller, 1938) plus valence neutrons (Table 1, Figures 1a-c and 2a-b, most notes in their captions).

To test this there is an attempt to interpret fission, mainly concentrating on fragment origin and yield, as it can direct reflect details of a nuclear structure. Furthermore, it tends to consider that α and cluster (nucleon number, $A > 4$) decay (Rose & Jones, 1984) were similar to fission (like super asymmetric fission) (Poenaru, Ivascu, & Sandulescu, 1979), despite indirect somewhat. Therefore, at this stage that their roots remain poorly understood a brief interpretation may be effectual. In the following, basic, light, mid, and heavy nuclei individually in the 1, 2-3, 4-5, and 6-7 (periods/layers) steps will be illustrated to emerge different shapes and folding.

a)

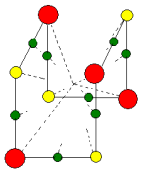

b)

	2B				1C	2C		1A	2A		3C	4C				3B	
1B		112			103	104		87	88		89	90			105		4B
	111		80		71	72		55	56		57	58		73		106	
		79		48				37	38				39		74		
			47		30			19	20			21		40			
16C	102	70		29				11	12				22		59	91	5C
15C	101	69						3	4						60	92	6C
								1									
8A	118	86	54	36	18	10	2	27	28		5	13	31	49	81	113	3A
7A	117	85	53	35	17	9		45	46		6	14	32	50	82	114	4A
										1							
14C	100	68						8	7	2					61	93	7C
13C	99	67		26				16	15	3			23		62	94	8C
			44		25			34	33	4		24		41			
		78		43				52	51	5			42		75		
	110		77		66	65		84	83	6	64	63		76		107	
8B		109			98	97		116	115	7	96	95			108		5B
	7B				12C	11C		6A	5A		10C	9C				6B	

c)

	1A	2A	3B	4B	5B	6B	7B	8B	9B	10B	1B	2B	3A	4A	5A	6A	7A	8A
1	1																	2
2	3	4											5	6	7	8	9	10
3	11	12											13	14	15	16	17	18
4	19	20	21	22	23	24	25	26	27	28	29	30	31	32	33	34	35	36
5	37	38	39	40	41	42	43	44	45	46	47	48	49	50	51	52	53	54
6	55	56	73	74	75	76	77	78			79	80	81	82	83	84	85	86
7	87	88	105	106	107	108	109	110			111	112	113	114	115	116	117	118

3C	4C	5C	6C	7C	8C	9C	10C	11C	12C	13C	14C	15C	16C	1C	2C
57	58	59	60	61	62	63	64	65	66	67	68	69	70	71	72
89	90	91	92	93	94	95	96	97	98	99	100	101	102	103	104

Figure 1. Nuclear folded and unfolded frames. (a) Red, yellow, and green are 4 *a*, 4 *b*, and 8 *c* axes (α-clusters), where are p_l (last proton) locations of representative, transition, and inner transition elements, respectively. (b) Four p_l (Z = 27, 28, 45, and 46) were sunk into the 1st period in old group 8B (American convention; groups 8-10, modern form), which was revised into groups 8-10B. (c) As 8 *c* α-clusters occupy 16 p_l, inner transition elements were suggested to increase from 2×14 to 2×16, then groups 8-10B only leave $_{78}$Pt and $_{110}$Ds. $_{71}$Lu and $_{72}$Hf of groups 1-2C into inner transition is following $_{29}$Cu and $_{30}$Zn of groups 1-2B into transition, though inner transition shell has been closed at $_{70}$Yb in Table 1

2. Nuclear 4 steps and 16 Axes

Basic nuclei ^{1,2,3}H, ^{3,4}He, neutron, and di-neutrons appear in nuclei that can be separated into core, middle, and skin, core + middle = c_m; skin particle, s_p, its particle structures and distributions was called skin configuration. Collectively, c_m is a noble nucleus and core is a ^{4}He in range Z = 3-26, for it will expand in Z = 27. On the other hand, in nuclear growth a nucleon behavior seems to loom up a tetrahedral shape having some "nucleon valence" (~ 4) to bind other nucleons or basic nuclei (Figure 2a) with an explicit direction, suggesting that a molecular bond may result essentially from this character (Figure 2b).

In F_2, O_2, and N_2 molecules, a single, double, and triple bond coincided with a pair of t in $(^{19}F^{4443})_2$, two pairs of d in $(^{16}O^{4242})_2$, and three pairs of d in $(^{14}N^{4222})_2$ suggest that molecular different shapes were rooted in skin configurations. Generally, skin configuration is corresponding to chemical main valence (Table 1), which is nearly the same as Lewis dot structure. For example, in $^{16}O_{c\text{-}2+2}{}^{4242}$, 2 dots and 2 lone pairs of electrons will identify with 2 d and 2 α; if 2 ^{1,2,3}H atoms descended on the 2 d extended lines, it is a $^1H_2{}^{16}O$ (Figure 2b), $^2H_2{}^{16}O$, or $^3H_2{}^{16}O$, providing a possibility to reassess that a reaction was between chemical and nuclear in water (Jones et al., 1989). At near the 2-3 step end, nuclei begin to grow n_v that first clearly to emerge 4 n_v will be in $^{40}Ar_{v\text{-}4}{}^{4444}$ (99.59%; $^{38}Ar_{v\text{-}2}{}^{4444}$, 0.063%; $^{36}Ar^{4444}$, 0.337%) in natural nuclei (~ 300), where the 4 n_v position is to grow 4 *b* α-clusters.

Table 1. A periodic distribution of nucleons for the maximal abundant isotopes

nucleus	nucleon distribution					chemical valence (p, d, t)	grown mass	abundance (%) / half-life
^{1}H	1^{a-1}							99.9
^{4}He	$1^{a+1\underline{1}\underline{1}}$							100
^{7}Li	$^{2}1^{2}$	$2^{a-1\underline{1}\underline{1}}$				1		92.4
^{9}Be	-	$2^{a-2\underline{1}\underline{1}\underline{1}}$				2		100
^{11}B	-	$2^{a-222\underline{1}}$				3		80.1
^{12}C	-	2^{a-2222}				4		98.9
^{14}N	-	2^{a-4222}				3		99.6
^{16}O	-	2^{a-4242}				2		99.7
^{19}F	-	2^{a-4443}				1		100
^{20}Ne	$^{2}1^{2}$	2^{a-4444}				0		90.4
^{23}Na	-	-	$3^{a-1\underline{1}\underline{1}}$					100
^{24}Mg	-	-	$3^{a-1\underline{1}\underline{1}\underline{1}}$				1	78.9
^{27}Al	-	-	$3^{a-222\underline{1}}$				3	100
^{28}Si	-	-	3^{a-2222}				1	92.2
^{31}P	-	-	3^{a-4232}				3	100
^{32}S	-	-	3^{a-4242}				1	94.9
^{35}Cl	-	-	3^{a-4443}				3	75.7
^{40}Ar	$^{2}1^{2}$	2^{a-4444}	$_{4}3^{a-4444}$				5	99.6
^{39}K	-	-	$^{8}3^{8}$	$4^{a-1\underline{1}\underline{1}}$				93.3
^{40}Ca	-	-	-	$4^{a-1\underline{1}\underline{1}\underline{1}}$				96.9
^{45}Sc	-	-	$^{8}_{4}3^{8}$	$4^{b-111\underline{3}}$				100
^{48}Ti	-	-	-	4^{b-2222}				73.7
^{51}V	-	-	-	4^{b-4232}				99.7
^{52}Cr	-	-	-	4^{b-4242}				83.7
^{55}Mn	-	-	-	4^{b-4443}				100
^{56}Fe	-	-	-	4^{b-4444}				91.7
^{59}Co	$^{4}1^{3}$	-	-	4^{-}				100
^{60}Ni	$^{4}1^{4}$	-	-	4^{-}				26.2
^{63}Cu	-	-	-	$4^{-a-1\underline{1}\underline{1}}$				69.1
^{64}Zn	-	-	-	$4^{-a-1\underline{1}\underline{1}\underline{1}}$				49.1
^{69}Ga	-	-	-	$_{4}4^{-a-111\underline{2}}$				60.1
^{74}Ge	-	-	-	$_{4}4^{-a-3232}$				36.5
^{75}As	-	-	-	$_{4}4^{-a-4232}$				100
^{80}Se	-	-	-	$_{8}4^{-a-4242}$				49.6
^{79}Br	-	-	-	$_{4}4^{-a-4443}$				50.6
^{84}Kr	$^{4}1^{4}$	2^{a-4444}	$_{4}3^{a-4444}$	$_{8}4^{b-4444\ a-4444}$				56.9
^{85}Rb	-	-	-	-	5^{a-1}			72.1
^{88}Sr	-	-	-	-	$5^{a-1\underline{1}\underline{1}\underline{1}}$			82.5
^{89}Y	-	-	$^{8}3^{8}$	-	$5^{b-111\underline{2}\ a-1\underline{1}\underline{1}\underline{1}}$			100
^{90}Zr	-	-	-	-	$5^{b-1212\ -}$			51.4
^{93}Nb	-	-	-	-	5^{b-4333}			100
^{98}Mo	-	-	-	-	$5^{b-4343\ a-1\underline{1}\underline{1}\underline{1}}$			24.3
^{99}Tc	-	-	-	-	$5^{b-4443\ -}$			2.1×10^{5} y
^{102}Ru	$^{6}1^{4}$	-	-	-	$5^{b-4444\ -}$			31.5
^{103}Rh	$^{6}1^{5}$	-	-	-	$5^{-\ -}$			100
^{104}Pd	$^{6}1^{6}$	-	-	-	$5^{-\ -}$			11.1
^{107}Ag	-	-	-	-	$5^{-\ a-1\underline{2}\underline{2}\underline{2}}$			51.8
^{114}Cd	-	$^{8}_{4}2^{8}$	$^{8}_{4}3^{8}$	-	$5^{-\ a-11\underline{2}\underline{2}}$			28.7
^{115}In	-	-	-	-	$5^{-\ a-222\underline{1}}$			95.7
^{120}Sn	-	-	-	-	$5^{-\ a-3333}$			32.5
^{121}Sb	-	-	-	-	$5^{-\ a-4333}$			57.2
^{130}Te	-	-	-	-	$_{8}5^{-\ a-4343}$			34.08
^{127}I	-	-	-	-	$_{4}5^{-\ a-4443}$			100
^{132}Xe	$^{6}1^{6}$	$_{4}2^{a4444}$	$_{4}3^{a-4444}$	$_{8}4^{b-4444\ a-4444}$	$_{8}5^{b-4444\ a-4444}$			26.9
^{133}Cs	-	-	-	-	-	6^{a-1}		100
^{138}Ba	-	-	-	-	-	$6^{a-11\underline{2}\underline{2}}$		71.6
^{139}La	-	-	-	-	$^{16}5^{16}$	$6^{c-1\underline{1}\underline{1}\underline{1}-1\underline{1}\underline{1}\ b-1\underline{1}\underline{1}\underline{1}\ a-1\underline{1}\underline{1}\underline{1}}$		99.9
^{140}Ce	-	-	-	-	-	$6^{c-1\underline{1}\underline{1}\underline{1}-1\underline{1}\underline{1}\underline{1}\ -\ -}$		88.4
^{141}Pr	-	-	-	-	-	$6^{c-1\underline{1}\underline{1}\underline{1}-111\underline{2}\ -\ -}$		100
^{142}Nd	-	-	-	-	-	$6^{c-111\underline{2}-111\underline{2}\ -\ -}$		27.1
^{145}Pm	-	-	-	-	-	$6^{c-2121-212\underline{2}\ -\ -}$		17.7 y
^{152}Sm	-	-	-	-	-	$6^{c-3232-3232\ -\ -}$		26.7
^{153}Eu	-	-	-	-	-	$6^{c-4232-3232\ -\ -}$		52.1
^{158}Gd	-	-	-	-	-	$6^{c-4333-4333\ -\ -}$		24.8

^{159}Tb	-	-	-	-	-	$6^{c\text{-}4343\text{-}4333}$	-	-				100
^{164}Dy	-	$^{8}2^{8}$	-	-	$^{16}{}_{8}5^{16}$	$6^{c\text{-}4343\text{-}4343}$	-	-				28.2
^{165}Ho	-	-	-	-	-	$6^{c\text{-}4443\text{-}4343}$	-	-				100
^{166}Er	-	-	-	-	-	$6^{c\text{-}4443\text{-}4443}$	-	-				33.5
^{169}Tm	-	-	-	-	-	$6^{c\text{-}4444\text{-}4443}$	$b\text{-}\underline{1}122$	-				100
^{174}Yb	-	-	-	-	-	$6^{c\text{-}4444\text{-}4444}$	-	-				32.02
^{175}Lu	-	-	-	-	-	6	-	$b\text{-}1\underline{222}$	-			97.4
^{180}Hf	-	-	-	-	-	6	-	$b\text{-}2\underline{222}$	$a\text{-}\underline{2222}$			35.08
^{181}Ta	-	-	-	-	-	6	-	$b\text{-}3\underline{222}$	-			99.9
^{184}W	-	-	-	-	-	6	-	$b\text{-}3333$	-			30.6
^{187}Re	-	-	-	-	-	$_{2}6$	-	$b\text{-}4333$	-			62.6
^{192}Os	-	-	-	-	-	$_{6}6$	-	$b\text{-}4343$	-			40.7
^{193}Ir	-	-	-	-	-	$_{6}6$	-	$b\text{-}4443$	-			62.7
^{194}Pt	-	-	-	-	-	$_{6}6$	-	$b\text{-}4444$	-			32.8
^{197}Au	-	-	-	-	-	$_{10}6$	-	-	$a\text{-}1\underline{222}$			100
^{202}Hg	-	-	-	-	-	$_{16}6$	-	-	$a\text{-}11\underline{22}$			29.8
^{205}Tl	-	-	-	-	-	$_{16}6$	-	-	$a\text{-}3222$			70.4
^{208}Pb	-	-	-	-	-	$_{16}6$	-	-	$a\text{-}3333$			52.4
^{209}Bi	-	-	-	-	-	$_{16}6$	-	-	$a\text{-}4333$			100
^{209}Po	-	-	-	-	-	$_{16}6$	-	-	$a\text{-}4342$			102 y
^{210}At	-	-	-	-	-	$_{16}6$	-	-	$a\text{-}4442$			8.1 h
^{222}Rn	$^{6}{}_{6}1^{6}$	$^{a4444}{}_{4}2$	$^{a\text{-}4444}{}_{4}3$	$^{b\text{-}4444\ a\text{-}4444}{}_{8}4$	$^{b\text{-}4444\ a\text{-}4444}{}_{8}5$	$_{16}6^{c\text{-}4444\text{-}4444}$	$b\text{-}4444\ a\text{-}4444$		7	$b\text{-}\underline{1111}$		3.82 d
^{223}Fr	-	-	-	-	-	-			7	-	$a\text{-}\underline{1}$	22 m
^{226}Ra	-	-	-	-	-	-			7	-	$a\text{-}1\underline{111}$	1600 y
^{227}Ac	$^{6}1^{6}$	-	-	-	-	-			$7^{c\text{-}1\underline{111}\text{-}1\underline{11}}$	-	$a\text{-}\underline{1111}$	21.77 y
^{232}Th	-	-	-	-	-	-			$7^{c\text{-}11\underline{22}\text{-}11\underline{22}}$	-	-	1.4×10^{10} y
^{231}Pa	-	-	-	-	-	-			$7^{c\text{-}11\underline{22}\text{-}1112}$	-	-	3.3×10^{4} y
^{238}U	-	-	-	-	-	-			$7^{c\text{-}33\underline{32}\text{-}33\underline{32}}$	-	-	99.2
^{237}Np	-	-	-	-	-	-			$7^{c\text{-}2223\text{-}222\underline{2}}$	-	-	2.1×10^{6} y
^{244}Pu	-	-	-	-	-	-			$7^{c\text{-}3333\text{-}3333}$	-	-	8.0×10^{7} y
^{243}Am	-	-	-	-	-	-			$7^{c\text{-}4323\text{-}3332}$	-	-	7370 y
^{247}Cm	-	-	-	-	-	-			$7^{c\text{-}4323\text{-}4322}$	$b\text{-}\underline{2222}$	-	1.56×10^{7} y
^{247}Bk	-	-	-	-	-	-			$7^{c\text{-}4242\text{-}4322}$	-	-	1.38×10^{3} y
^{251}Cf	-	-	-	-	-	-			$7^{c\text{-}4343\text{-}4342}$	-	-	898 y
^{252}Es	-	-	-	-	-	-			$7^{c\text{-}4443\text{-}4342}$	-	-	471.7 d
^{257}Fm	-	-	-	-	-	-			$7^{c\text{-}4443\text{-}4442}$	-	$a\text{-}\underline{2222}$	100.5 d
^{258}Md	-	-	-	-	-	-			$7^{c\text{-}4444\text{-}4442}$	-	-	51.5 d
^{259}No	-	-	-	-	-	-			$7^{c\text{-}4444\text{-}4444}$	$b\text{-}\underline{1222}$	-	58 m
^{260}Lr	-	-	-	-	-	-			7	- $b\text{-}\underline{2222}$	-	3 m
^{261}Rf	-	-	-	-	-	-			7	- $b\text{-}3\underline{222}$	-	1.9 s
^{262}Db	-	-	-	-	-	-			7	- $b\text{-}332\underline{2}$	-	35 s
^{265}Sg	-	-	-	-	-	-			$_{1}7$	- $b\text{-}3333$	-	16.2 s
^{272}Bh	-	-	-	-	-	-			$_{7}7$	- $b\text{-}4333$	-	10 s
^{275}Hs	-	-	-	-	-	-			$_{9}7$	- $b\text{-}4343$	-	0.15 s
^{276}Mt	-	-	-	-	-	-			$_{9}7$	- $b\text{-}4443$	-	0.72 s
^{281}Ds	-	-	-	-	-	-			$_{16}7$	- $b\text{-}4444$	$a\text{-}\underline{2111}$	20 s
^{281}Rg	-	-	-	-	-	-			$_{16}7$	- -	$a\text{-}2\underline{111}$	26 s
^{285}Cn	-	-	-	-	-	-			$_{16}7$	- -	$a\text{-}3\underline{222}$	30 s
^{286}113	-	-	-	-	-	-			$_{16}7$	- -	$a\text{-}323\underline{2}$	20 s
^{288}114	-	-	-	-	-	-			$_{16}7$	- -	$a\text{-}3333$	0.52 s
^{289}115	-	-	-	-	-	-			$_{16}7$	- -	$a\text{-}4333$	0.22 s
^{290}116	-	-	-	-	-	-			$_{16}7$	- -	$a\text{-}4343$	15 ms
^{291}117	-	-	-	-	-	-			$_{16}7$	- -	$a\text{-}4443$	
^{292}118	$^{6}1^{6}$	$^{a4444}{}_{4}2$	$^{a\text{-}4444}{}_{4}3$	$^{b\text{-}4444\ a\text{-}4444}{}_{8}4$	$^{b\text{-}4444\ a\text{-}4444}{}_{8}5$	$_{16}6^{c\text{-}4444\text{-}4444}$	$b\text{-}4444\text{-}a4444$		$_{16}7^{c\text{-}4444\text{-}4444}$	$b\text{-}4444$	$a\text{-}4444$	

Subscript, left and right superscript of periodic number are the numbers of n_v, n_p and p_l respectively, and skin is 4 *a*, 4 *b*, and 8 *c* axes in 7 codes: 1, proton (p); 2, deuteron (d); 3, triton (t); 4, alpha particle (α); $\underline{1}$, neutron (n); $\underline{2}$, di-neutrons; $\underline{3}$, ^{3}He ion. Single hyphen (-) is the same as upside. Chemical valence is in the 2nd period and in the 3rd period is grown mass between these nuclei. There will be a fluctuation only if ^{58}Ni (67.88%) and ^{106}Pd (27.33%) in group 10B are listed.

Along with nuclear crystal growing to the 4th layer, its skin area will increase enough to hold another 4 *b* α-clusters in between 4 *a* α-clusters; further, its core will be intensified in old group 8B to support increasing mass. In terms of electron distributions, a proton distribution of $_{21}$Sc is 2 p_l of $_{19}$K and $_{20}$Ca on 2 *a* axes, and p_l of $_{21}$Sc on *b* axis, but it seems to be questionable for nucleon arrangements of subsequent elements; i.e., 3 p_l of $_{19}$K, $_{20}$Ca, and $_{21}$Sc may

simultaneously glide upon *b* axes. In comparison, a pair distributions of electrons and protons is $_{21}$Sc-e(18)ds^2/p(18)d^3 (in proton distributions, *a* = s+p that in range *Z* = 3-26, 2 p and 2 n of basal tetrahedral α-particle that 4 *a* axes stand on have not been distinguished, *b* = d, and *c* = f, respectively). Furthermore, 4 p_l of $_{27}$Co, $_{28}$Ni, $_{45}$Rh, and $_{46}$Pd will sink into the core (Figure 1b), which may be ended that a total of 6 p_l (*Z* = 1, 2, 27, 28, 45, and 46) with 6 n are to form an innermost close-packed core (Figure 2a). However, this performance will enable a nucleus to possess a definite hub, a Coulomb repulsion center, otherwise its shape cannot be opened, like a tiny liquid drop. Parallel to this was that per nucleon binding energy ~ 8.7 MeV is maximal, as nuclear mass increase to *A* ~ 60 (Nudat 2), which would imply that though at Fe-Co-Ni region nuclear core has been intensified immediately, a sharp change of nucleon distributions, its curve remains to fall from Fe, a last element owning c-2+2 that may play a critical role in chemical element distributions of universe. Additionally, ferromagnetic only occurs in Fe, Co, and Ni at room temperature that possibly has a link to a structure and vibratory pattern of their nuclei.

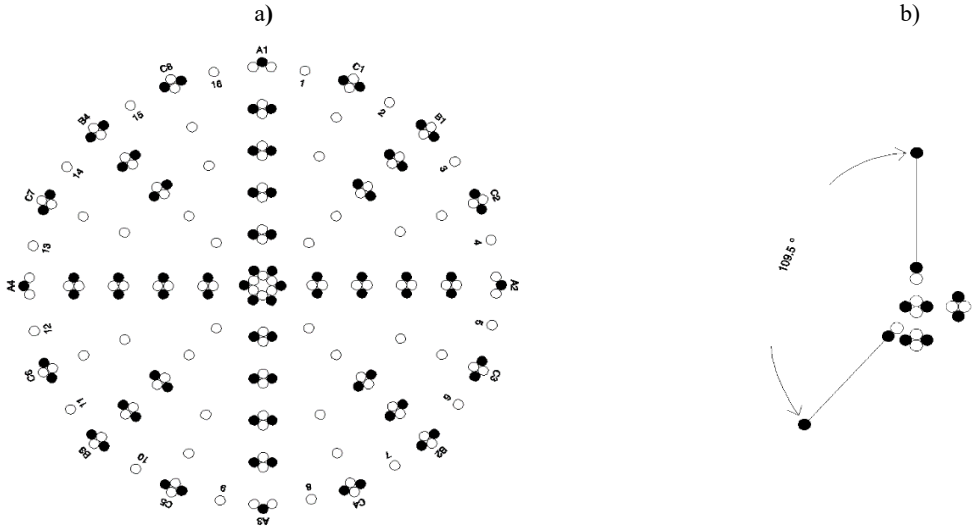

Figure 2. A crystal images of ^{208}Pb (unfolded) and $^1H_2{}^{16}O$. (a) Closed and open circles are protons and neutrons. In $^{208}{}_{82+86+40}Pb_{c\text{-}6+6,v\text{-}4,4,8,8,16}{}^{c\text{-}4444\text{-}4444,b\text{-}4444,a\text{-}3333}$, right superscript is skin configuration, subscript c-6+6 is core (n+p), v-4,4,8,8,16 is n_v number in the 2-6 layers, and 82+86+40 is $Z+n_p+n_v$ three shells, where n_p is pair neutron, and n_v is valence neutron (single open circles) to fill gaps in axes and layers. A nuclear coordinate was introduced to describe fission that the serial numbers of axes and layers are after *a*, *b*, and *c* letters; for valence neutron is *n* that it is clockwise rotating from *a*1 axis to the origin point: 1→4, 1→8, and 1→16 in the 2-3, 4-5, and 6-7 steps, respectively. This figure suggests that in 1-1/4-8 fission (from *n*1-6 through 1/4 core to *n*8-6), 1-8 and 8-1 sectors are light (A_L) and heavy (A_H) fragments, some of 6 n_v (*n*1-6, 1-4, 1-2 and *n*8-6, 4-4, 2-2) became prompt neutrons in the split line, and angular distributions of α-particle were 90 – 22.5° for A_L and 90+22.5° for A_H coming from *c*1-6 or *c*4-6. (b) In the center is a $^{16}O_{c\text{-}2+2}{}^{4242}$ and the farthest are 2 ^{1}H, suggesting that its chemical valence and their angle are rooted in the 2 d. If 2 d of $^{16}O^{4242}$ (99.757%) were replaced by 1 or 2 t, it is $^{17}O^{4342}$ (0.038%) or $^{18}O^{4343}$ (0.205%)

One of extraordinary feature in the periodic table is old group 8B existence, implying that nuclei contain an expansible core, the other is the number of inner transition metals, from where a particular place, $_{57}$La-e(54)ds^2/p(54)f^3, start to grow out between 4 *a* and 4 *b* α-clusters, implying that nuclei are folding. The extrapolation is that, if inner transition p_l were on 6 faces or 12 sides of Figure 1a, it needs 12 or 24 p_l, what is both impractical. Thus, it may averagely vacate 4 of 12 sides to grow 16 elements. On the other hand, whether inner transition contains 14 elements? If so, given that α is one of particles to construct a nucleus, as such an odd number of 7 α will be asymmetric in a nuclear shape (coordinate). So far, it is thought that nuclear shapes might have not been so easy to recognize, whereas in here are visible that almost are tetrahedral in the 2-3 step (^{12}C, ^{28}Si) and cubic in the 4-5 step (^{74}Ge, ^{120}Sn), but in the 6-7 step (^{208}Pb), their shapes would be kept in a phase between cubic and flat, which might relate to a nuclear vibratory form. In fact, originally this nuclear pattern was two dimensional using Go game stones to put on the floor, however, it was so coincidental that when it was folded into three dimensional.

Folding nuclei were suggested from the 16 axes that in Table 1 show to correspond to the groups, which is almost same in a tri-group, regardless of group A, B, and C, such as skin configuration 4443 in tri-group 7 (7A, 7B, 13-14C: $^{165}Ho^{c\text{-}4443\text{-}4343}$ and $^{166}Er^{c\text{-}4443\text{-}4443}$). In tri-group 3, a di-neutrons may serve as a proton in skins of ^{45}Sc and ^{89}Y in 3B that each of them has 3 p_l to stay on 3 of 4 *b* axes, then a di-neutrons will substitute for a proton to occupy a surplus axis to form a stable *b*-tetrahedron out of their c_m, i.e., ^{40}Ar+b-111$\underline{2}$ (^{45}Sc, 100%) and ^{84}Kr+b-111$\underline{2}$ (^{89}Y,

100%). In stable nuclei, ^{45}Sc is likely emerging di-neutrons for the first time, which seems a unique structure that its proton distribution differs with of electron, as earlier mentioned. In group 1A, a ^{7}Li (92.5%) may prefer a-1$\underline{11}$ to a-3 (a single triton) in its skin, including below ^{23}Na$^{1\underline{11}}$ (100%), ^{39}K$^{1\underline{11}}$ (93.3%), ^{87}Rb$^{1\underline{11}}$ (27.83%), ^{135}Cs$^{1\underline{11}}$ (2.3×10^{6} y), and ^{225}Fr$^{1\underline{11}}$ (3.95 m), because skin particle masses will smoothly increase from 1 to 4 along with sweeping tri-groups from 1 (1A, 1B, 1-2C) to 8 (8A, 8-10B, 15-16C). Apparently, there is a correspondence between atomic and nuclear periodicity, such as a-4443 in ^{19}F, ^{35}Cl, ^{79}Br, and ^{127}I in group 7A that all their chemical main valence is 1. Perhaps, it cannot be excluded that the element properties were related to that long *a*, mid *b*, and short *c* axes extend a different depth in nuclei (Figure 2a). For example, lanthanide contraction may be relevant to inner transition 16 p_l trapped in 8 *c* axes where is low lying between 4 *a* and 4 *b* axes. Also, in ^{23}Na^{35}Cl, thin a-1$\underline{11}$ in ^{23}Na (^{20}Ne+a-1$\underline{11}$) may be looser to its ^{m}c than thick a-4443 in ^{35}Cl (^{20}Ne+a-4443), somewhat like that nucleon halo, if involved nuclear force, a factor possible influence on their atomic radii (0.15 and 0.09 nm), implying that nuclear radii might link to atomic radii.

3. Valence Neutron

General in a nucleus, neutrons exceed protons in number, as the slope of beta stable line plotting in a chart (Nudat 2), suggesting obeyed

$$A = Z + n_p + n_v, \quad (1)$$

where $n_v = 2(2^2, 2^3, 2^4)$ are valence neutron holes in the 2-3, 4-5, and 6-7 steps of nuclei, respectively (Figure 2a), e.g. ^{132}Xe = 54 + 54 + $2(2^2+2^3)$. Also, n_v approximates to α, e.g., ^{132}Xe = $24(n_v+\alpha)$ + $_6$12, where $_6$12 is its core in $_ZA$; the $_6$12 might be replaced by a $_6$18 in ^{222}Rn (Table 1). Commonly, isotopic mass change for light nuclei was n_p as ^{16,17,18}O in Figure 2b. For mid nuclei, e.g., ^{112}Sn$_{v\text{-}12}{}^{2222}$ and ^{124}Sn$_{v\text{-}20}{}^{3333}$, both their n_p and n_v were varied (Table 2). In Table 1 grown masses show a regular phenomenon that 1, 3, 1, 3, 1, 3, and 5 in the 3rd period, when grow from odd to even *Z*, only fill 1 p_l (^{23}Na$^{1\underline{11}}\rightarrow{}^{24}Mg^{1\underline{111}}$) or with 4 n_v (^{35}Cl$^{4443}\rightarrow{}^{40}Ar_{v\text{-}4}{}^{4444}$), but 1 p_l is often accompanied by 2 n_p (^{28}Si$^{2222}\rightarrow{}^{31}$P^{4232}) from even to odd *Z*.

Table 2. A tentative nucleon arrangement of $^{99\text{-}138}$Sn

Sn nuclide	c_m	n_v	skin configuration b	skin configuration a	abundance (%) / $T_{1/2}$
99	76	0, 0, 3	4444	1111	
100	-	0, 0, 4	-	1111	0.86 s (ε, εp)
101	-	0, 0, 5	-	-	1.7 s (ε, εp)
102	-	0, 0, 6	-	-	3.8 s (ε)
103	-	0, 0, 7	-	-	7.0 s (ε, εp)
104	-	0, 0, 8	-	-	20.8 s (ε)
105	-	0, 0, 8	-	2111	32.7 s (ε, εp)
106	-	0, 0, 8	-	2211	115 s (ε)
107	-	0, 0, 8	-	2221	2.90 m (ε)
108	-	0, 0, 8	-	2222	10.30 m (ε)
109	-	0, 1, 8	-	-	18.0 m (ε)
110	-	0, 2, 8	-	-	4.11 h (ε)
111	-	0, 3, 8	-	-	35.3 m (ε)
112	-	0, 4, 8	-	-	0.96
113	-	0, 4, 8	-	3222	115.09 d (ε)
114	-	0, 4, 8	-	3322	0.66
115	-	0, 4, 8	-	3332	0.34
116	-	0, 4, 8	-	3333	14.54
117	-	1, 4, 8	-	-	7.68
118	-	2, 4, 8	-	-	24.22
119	-	3, 4, 8	-	-	8.59
119m	-	4, 4, 8	-	3332	291.1 d (IT)
120	-	4, 4, 8	-	3333	32.58
121	-	4, 4, 8, 1	-	-	27.03 h (β^-)
121m	-	3, 4, 8, 2	-	-	43.9 y (IT)
122	-	4, 4, 8, 2	-	-	4.72
123	-	4, 4, 8, 3	-	-	129.2 d (β^-)
124	-	4, 4, 8, 4	-	-	5.94
125	-	4, 4, 8, 5	-	-	9.64 d (β^-)
126	-	4, 4, 8, 6	-	-	2.3×10^5 y
127	-	4, 4, 8, 7	-	-	2.10 h (β^-)
128	-	4, 4, 8, 8	-	-	59.07 m (β^-)
129	-	4, 4, 8, 8, 1	-	-	6.9 m (β^-)
130	-	4, 4, 8, 8, 2	-	-	3.72 m (β^-)
131	-	4, 4, 8, 8, 3	-	-	56.4 s (β^-)
132	-	4, 4, 8, 8, 4	-	-	39.7 s (β^-)
133	-	4, 4, 8, 8, 5	-	-	1.46 s (β^-, β^-n)
134	-	4, 4, 8, 8, 6	-	-	1.05 s (β^-, β^-n)
135	-	4, 4, 8, 8, 7	-	-	530 ms (β^-, β^-n)
136	-	4, 4, 8, 8, 8	-	-	0.25 s (β^-, β^-n)
137	-	4, 4, 8, 8, 9	-	-	190 ms (β^-, β^-n)
138	-	4, 4, 8, 8, 10	-	-	~ 408 ns

In 39 neutrons (138 - 99), $n_v \sim 21$, $n_p \sim 8$, and 10 n in the 6th layer is neutron skin (halo). Valence neutrons in the 2-6 layers are compiled in a column. Decay modes: ε, electron capture; p, proton emission; IT, isomeric transition; β^-, beta-minus decay; n, neutron emission.

Admittedly, in many cases this primary neutron fit is alternative. For example, a ^{36}S (0.014%) is $^{36}S_{v\text{-}4}4^{242}$ or $^{36}S_{v\text{-}2}4^{343}$ that how to balance n_p and n_v, and 20 n_v of ^{127}I is v-0,4,8,8 or v-4,4,8,4 (Table 1) in the 2-5 layers. Perhaps, in a nucleus neutron different distributions are correlated with nuclear isomers (Hahn, 1921) (marked m1, m2, m3…), while its proton shell is unconcerned; e.g., $^{79}Br_{v\text{-}4,4}$ (50.69%) and $^{79m}Br_{v\text{-}0,0,8}$ (5.1 s), or other distributions in the 2-4 layers (see also $^{119m,121m}Sn$ in Table 2). However, $^{12}C^{2222}$ (98.93%), $^{13}C^{3222}$ (1.07%), $^{14}C^{3232}$ and $^{28}Si^{2222}$ (92.223%), $^{29}Si^{3222}$ (4.685%), $^{30}Si^{3232}$ (3.092%) demonstrate the higher abundance, the more concise structure.

Away from the beta stable line, ^3He was estimated to generate in skin of neutron-deficient light nuclei, e.g. $^{19}Ne_{c\text{-}2+2}{}^{4443}$ (17.22 s) and $^{17}Ne_{c\text{-}2+2}{}^{4333}$ (109.2 ms). Moreover, a heavy nucleus lack of neutrons, n_v, to bind its vertical *a*-(5α), *b*- (3α, $^{12\text{-}15}C$, Rose & Jones, 1984), and *c*- (1α) clusters may more easily cause decay, corresponding to the fact that α-decay only happen in neutron-deficient heavy nuclei (excepting super heavy nuclei, in mid nuclei almost never, e.g. $^{99\text{-}111}Sn$ in Table 2) that begin to grow *c*-1α clusters. Therefore, it seems difficult to distinguish α-cluster decay and nuclear fission that only split ratios are different, if nuclei were a skeleton of 16 α-clusters (Table 3).

Toward neutron drop line, e.g., a structure of super large $^{11}Li\text{-}2{1^2},2^{a\text{-}2\underline{111}},3^{\underline{11}}$ (8.75 ms) might be a c_m of ^9Li with a 2-neutron halo (CERN, 2004). Additionally, a neutron skin (halo) may happen in a stable nucleus; e.g., $^{136}Xe\text{-}{6}1^6,{}_8{4}2^8,{}_4{3}3^8,{}_8{16}4^{16},{}_8{16}5^{16},6^{\underline{1111}}$ (8.9%), this $6^{\underline{1111}}$ skin will cage a ^{132}Xe, for its n_p and n_v shells have been closed.

Note that, unexpectedly, all of Z , n_p, and n_v three shells filled up ($A = 2Z + n_v$, ideal nucleus) shows not a most proper structure from two abundance ($T_{1/2}$) lines of ideal nuclei and their maximal abundant isotopes intersecting at $^{132}Xe_{v\text{-}4,4,8,8}$ (26.9%), i.e., n_v too many in $^{24}Ne_{v\text{-}4}$ (3.38 m), $^{44}Ar_{v\text{-}4,4}$ (11.87 m), and $^{88}Kr_{v\text{-}4,4,8}$ (2.84 h), but too few in $^{212}Rn_{v\text{-}4,4,8,8,16}$ (23.9 m) and $^{292}118_{v\text{-}4,4,8,8,8,16,16}$ (?). Nevertheless, here was unable to find a better way to fit pair and valence neutrons with the line of beta stability.

4. Fission Outlines

On the whole, fission fragments seem to agree with nuclear 16 α-clusters splitting into different ratios (Table 3). Relatively complicated is to consider a possible skin particle glide in asymmetric fission. Here a mode is taking a fragment to be a mixture of c_m and s_p partly. For example, in 1-1/4-8 fission of ^{235}U+n, its c_m is lined off:

$$^{212}Rn_{\ 1\text{-}1/4\text{-}8} \rightarrow {}_{53}129 + {}_{33}83, \tag{2}$$

and its s_p falls into

$$c\text{-}222\underline{2},b\text{-}\underline{11},a\text{-}\underline{111} + c\text{-}222\underline{2},b\text{-}\underline{11},a\text{-}\underline{1} = {}_3{13} + {}_3{11}, \tag{3}$$

then add Equations 3 to 2,

$$^{235}U+n_{\ 1\text{-}1/4\text{-}8} \rightarrow ({}_{53}129+{}_3{13}) + ({}_{33}83+{}_3{11}) = {}^{142}Ba + {}^{94}Kr, \tag{4}$$

$$^{235}U+n_{\ 1\text{-}1/4\text{-}8} \rightarrow {}_{53}129 + ({}_{33}83+{}_6{24}) = {}^{129}I + {}^{107}Y, \tag{5}$$

$$^{235}U+n_{\ 1\text{-}1/4\text{-}8} \rightarrow ({}_{53}129+{}_6{24}) + {}_{33}83 = {}^{153}Pr + {}^{83}As, \tag{6}$$

suggesting that a fragment peak yield (Thomas & Vandenbosch, 1964) could be partly contributed from ${}_3{13}$ and ${}_3{11}$ glide, albeit likely, the higher shift ratio, the lower yield. In Equation 4 s_p has not glided that two fragment yields are ~ 6% at peak. The valley is a symmetric fission:

$$^{235}U+n_{\ 1\text{-}1/2\text{-}9} \rightarrow {}_{46}118 + {}_{46}118, \tag{7}$$

~ 0.1%.

Comparing Equations 5 and 6 suggests that s_p prefer to glide upon A_L ($3^a2^b4^c{:}1^a2^b4^c{+}s_p$), likely that it is to balance two fragment masses to rip a nucleus, for the yield of Equations 5 is roughly higher than 6. This view is also illustrated in Fig. 1 of Unik et al., (1973) that A_H masses are nearly constant, while A_L masses increase in ^{229}Th, $^{233,235}U$, ^{239}Pu, ^{245}Cm, ^{249}Cf, and ^{254}Es (n,f). However, s_p may glide to affect thermal neutron (n,f) and spontaneous (sf) asymmetric fission that transition from asymmetry to symmetry is about in two sides of Z 94±6 ($_{88}Ra\text{-}_{100}Fm$) [Z 94 = (86+102)/2, where 86 and 102 are representative and inner transition closed shells], implying that its mass number is neither too many, nor too few. For example, ^{226}Ra (^3He, df) simultaneously revealed asymmetric and symmetric fission (Konecny, Specht, & Weber, 1973), and from $^{254}{}_{100+114+40}Fm^{c\text{-}4443\text{-}4443,b\text{-}\underline{2222},a\text{-}\underline{1111}}$ (sf, asymmetric) (Gindler, Flynn, Glendenin, & Sjoblom, 1977) to $^{258}{}_{100+118+40}Fm^{c\text{-}4443\text{-}4443,b\text{-}\underline{2222},a\text{-}\underline{2222}}$ (^{257}Fm+n, symmetric) (Flynn, Gindler, & Glendenin, 1975) a-$\underline{1111}$ was replaced by a-$\underline{2222}$ that is likely closed n_p-118 shell fenced against the

s_p glide. In the case of $^{252}{}_{102+110+40}No^{c\text{-}4444\text{-}4444,b\text{-}\underline{1111},a\text{-}\underline{1111}}$, despite its *Z*-102 shell closure, it is an asymmetric fission (Bemis et al., 1977), not impossible that it lacks 8 n_p than ^{258}Fm to resist the s_p glide.

In addition, possible to result in even-*Z* fragment that its energy release is greater than odd (fine structure of fragment masses, interval $A \sim 5$, $n_v+\alpha$) (Thomas & Vandenbosch, 1964), part of s_p might be fused in glide, since in ^{235}U (n,f), its skin having no an innate α-particle, has occurring polar α-particle emission, about 0° or 180° with respect to the fission axis (Piasecki, Dakowski, Krogulski, Tys, & Chwaszczewska, 1970). Moreover, the yield is over 3 times for A_L to A_H flight directions (Piasecki & Nowicki, 1979), which is in favor of s_p to glide upon A_L again.

At leftmost bottom sides of a double peak curve, $A \sim 80$ and ~ 130, are two vanishing points of A_L, A_H (Unik et al., 1973), neutron (Bowman, Milton, Thompson, & Swiatecki, 1963), and α-particle (Schmitt, Neiler, Walter, & Chetham-Strode, 1962), which both point to a sector where its 2 edges are enclosed by long 2 *a* axes, i.e., $2^a1^b2^c$ (A_L) and $3^a2^b4^c$ (A_H) α-clusters. Take neutron yields for example, in

$$^{252}Cf_{\ 1\text{-}1/4\text{-}8} \rightarrow {}_{53}129 + ({}_{33}83+{}_{12}40) = {}_{53}129 + {}_{45}123, \quad (8)$$

where $_{53}129$ is a minimal $3^a2^b4^c$ and $_{45}123$ is a complementary $1^a2^b4^c$ to yield maximal neutrons (~3) (Bowman, Milton, Thompson, & Swiatecki, 1963), suggesting that maximal neutron yield is from a sector of short 2 *c* axis edges. In ^{254}Fm (sf) that both ^{252}Cf and ^{254}Fm neutron shells were n_p-114+n_v-40 shows a similar result of neutron yield: minimum at *A* 129-130 of A_H and maximum at *A* 123-124 of A_L (Gindler, Flynn, Glendenin, & Sjoblom, 1977).

Similarly, a neutron deficient fragment seems also relating to this. For instance, in $^{238}U+^{12}C$ (Delaune et al., 2013), a ^{73}As may consist with $_{30}70+{}_3 3$ in 4-1/4-9 fission, where $_{30}70 = 5\alpha\times2+3\alpha+1\alpha\times2+10n_v$ and $_3 3$ is from core. In $^{238}U+p$ (Klingensmith, & Porile, 1988), ^{72}As and ^{69}Zn might come from other ways, because the 10 n_v normally cannot be released inside a minimal $2^a1^b2^c$ ($^{70}{}_{30}Zn$), unless one of them has become a delayed neutron (Amiel, 1969) that when the fragment was reconstituted to turn into a daughter nucleus.

However, 4 *a*, 4 *b*, and 8 *c* α-clusters could set up different fission barriers that 2 of 4 *a* will be the biggest. On the other hand, a split line sweeps a single *c*, *b*, or *a* axis that will create a new mass difference (Table 3). To an *a* axis, it is, e.g.,

$$^{235}U+n_{\ 1\text{-}1/2\text{-}8} \rightarrow ({}_{53}126+{}_3 13) + ({}_{33}86+{}_3 11) = {}^{139}Ba + {}^{97}Kr = ({}_{46}118+{}_{10}21) + ({}_{46}118 - {}_{10}21), \quad (9)$$

where $_{10}21 = {}_{10}20 + 1$, a cluster of 5 α (*a*3 axis) plus 1 n at *a*3-7 position, when the split line swept anticlockwise from 1-1/2-9 (Equation 7) to 1-1/2-8.

Table 3. Some fission depths and paths of ^{236}U.

fission depth and path	split ratio of 16 α-clusters	*Z*-*A* distribution A_L	A_H
1-1/2-9	$2^a2^b4^c : 2^a2^b4^c$ (8 : 8)	^{118}Pd	^{118}Pd
2-1/2-9	$2^a2^b3^c : 2^a2^b5^c$ (7 : 9)	^{111}Tc	^{125}In
3-1/2-9	$2^a1^b3^c : 2^a3^b5^c$ (6 : 10)	^{95}Rb	^{141}Cs
4-1/2-9	$2^a1^b2^c : 2^a3^b6^c$ (5 : 11)	^{88}Se	^{148}Ce
1-1/4-8	$1^a2^b4^c : 3^a2^b4^c$ (7 : 9)	^{94}Kr	^{142}Ba
2-1/4-8	$1^a2^b3^c : 3^a2^b5^c$ (6 : 10)	^{85}As	^{151}Pr
3-1/4-8	$1^a1^b3^c : 3^a3^b5^c$ (5 : 11)	^{69}Co	^{167}Tb
4-1/4-8	$1^a1^b2^c : 3^a3^b6^c$ (4 : 12)	^{60}Cr	^{176}Er
1-0-9	$2^a2^b4^c : 2^a2^b4^c$ (8 : 8)	^{112}Tc	^{124}In
2-0-9	$2^a2^b3^c : 2^a2^b5^c$ (7 : 9)	^{105}Zr	^{131}Te
3-0-9	$2^a1^b3^c : 2^a3^b5^c$ (6 : 10)	^{89}Se	^{147}Ce
4-0-9	$2^a1^b2^c : 2^a3^b6^c$ (5: 11)	^{82}Ga	^{154}Pm
α-cluster decay			
1-0-2	1^c : $4^a4^b7^c$ (1 : 15)	^4He	^{232}Th
2-0-3	1^b : $4^a3^b8^c$ (1 : 15)	^{12}C	^{224}Rn
4-0-5	1^a : $3^a4^b8^c$ (1 : 15)	^{20}Ne	^{216}Pb

A structure of ^{236}U was $^6{}_1{}^6,{}^8{}_4{}^2,{}^8{}_4{}^3{}^8,{}^{16}{}_8{}^4{}^{16},{}^{16}{}_8{}^5{}^{16},{}^{32}{}_{16}6^{32},7^{c\text{-}2222\text{-}2222,b\text{-}\underline{1111},a\text{-}\underline{1111}}$. Fission depth (different divide of core $_6$12 nucleons) was mainly classified into: 1/2, $_3$6:$_3$6; 1/4, $_3$3:$_3$9; 0, 0:$_6$12. The n_v number error is about ±3 in mass division, which could be related to isotopic products. In the split lines s_p and n_v have not been allotted to α-cluster decay.

A binary fission in Figure 2a could draw a line from one side through core to the opposite side. When draw three lines, e.g., 1-c (from *n*1-6 to core), 2-c, and 9-c, it is a ternary 1-2-9 fission. Usually, 1-2 sector (one of 8 *c* axes) is a place of light charged particle (LCP) emission that can partition it into three points: *c*1-7 (p, d, t, α), *c*1-6 (α), and *c*1-6+*c*1-7 (^{7,8,9}Li, ^{9,10}Be). LCP emission probabilities in per 10^3 sf of ^{252}Cf$^{c\text{-}4343\text{-}4343,b\text{-}2222,a\text{-}1111}$ are: α-3.3, t-0.2, d-0.02, and p-0.06, respectively (Wild et al., 1985), slightly less than ideal that its skin has 4 α and 4 t, no d and p, which might be able to serve as a probe to identify skin configurations. If the track varied from 1-2-9 to 1-4-8 randomly, it is a three large fragment fission (Muga, Rice, & Sedlacek, 1967), in which ^{235}U (n,f), three sectors are about 1-4 (^{35}Mg), 4-8 (^{56}Sc), and 8-1 (^{145}Pr). It therefore was sensible to deduce that lighter fragments most likely result from a different combination of *a*, *b*, and *c* axes, e.g., 1^c, $A \sim 10$, LCP; 1^b2^c, $A \sim 30$, ^{28}Mg (Iyer & Cobble, 1966); $1^a1^b1^c$, $A \sim 50$, ^{47}Ca, ^{48}Sc (Klingensmith, & Porile, 1988). From here, naturally, it is tempting to expect that a nucleus might deeply be fragmented into four large fragments; e.g., in a quaternary 1-3-9-14 fission of ^{235}U+n, four sectors are 1-3 (^{25}F), 3-9 (^{93}Rb), 9-14 (^{69}Co), and 14-1 (^{49}K). However, four coincident fragment angular, energy, and mass distributions in a quaternary fission would shed light upon that whether a nuclear shape is from folded to unfolded in fission.

5. Discussion

To explain fission phenomena rely on what a nuclear model was based on. However, this work seems flexible to fit. Namely, a nuclear fission, asymmetric limited within Z 94 ± 6 nuclei as a rule, is likely that its 16 α-clusters are splitting into different ratios from 15:1 (1^c, α decay; 1^b or 1^a, cluster decay, essentially similar to three large fragments in a fission) to 8:8 to produce different mass fragments, and n_v in a split line will prevail over n_p to convert prompt neutrons. For example, if 16 α-clusters were splitting into 9:7, a pair fragment mass difference is ${}_ZA \geqslant {}_{20}40$ (±1 *a* axis, 2 clusters of 5 α) in ^{235}U+n→^{137}Ba+^{97}Kr+2n. In addition, among LCP most probable emission is α that its angle differs from polar emission is perpendicular to fission axis, nearly $90\pm22.5^\circ$ to A_H and A_L, respectively, where $22.5^\circ = 360^\circ/16$. Since a fission nucleus is almost impossibly complete unfolded, its α emitting angle is within 67.5° -112.5° that came from one of inner transition 8 α-particles, which is satisfactorily in agreement with Fig. 9 of Fluss, Kaufman, Steinberg, and Wilkins (1973).

In addition, the yields of various fragments suggest to vanish in the same two points: $3^a2^b4^c$ ($A \sim 130$) and $2^a1^b2^c$ ($A \sim 80$) α-clusters. Currently, fragment $A \sim 130$ and $A \sim 80$ were explained near *Z*-50, *N*-82 and *Z*-28, *N*-50 doubly magic shells, respectively, which seem that there has no a distinction of proton and neutron shells. Perhaps, their shells are the same only in magic number 2 (^{4}He), 8 (^{16}O), and 20 (^{40}Ca) (Table 1); for the 28, 50, and 82, it is to differ because of valence neutron emergence. To *N*-126 shell in Figure 2a shows to derive from n_p-86+n_v-40, a frame to grow $^{208}{}_{82+86+40}$Pb^{3333}, ^{209}Bi^{4333}, ^{210}Po^{4343}, ^{211}At^{4443}, and $^{212}{}_{86+86+40}$Rn^{4444}. Though only *Z*-2, *N*-2, *Z*-28, and *N*-126 shells are closed here (even if completely closed ideal nuclei are not most stable, except ^{132}Xe), magic nuclei have been displayed a definite image (Figures 2a-b). And, it is undeniable that all magic nuclei together with their neighbor nuclei able to grow is so smooth in Table 1, which will be helpful to account for magic number phenomena in the future.

On the other hand, a nucleus might emerge different structures in ground and excited states. For example, a ^{16}O in ground state is $^{16}O_{c\text{-}2+2}{}^{4242}$ and in excited state is 4 α-structure that skin 2 d of $^{16}O_{c\text{-}2+2}{}^{4242}$ were combined 1 α; otherwise in ground state a 4 α-structure of ^{16}O is inconceivable to carry two hydrogen atoms to build a water molecule. Whereas a $^1H_2{}^{16}O$ will have in the main understood at a glance in Figure 2b. Also, it appears straightforward, if alternating single and double bonds of a benzene ring ($^{12,13,14}C_6{}^1H_6$), a buckyball ($^{12,13,14}C_{60}$), and diamond ($^{12,13,14}C_n$) were rooted in a tetrahedral nucleus of ^{12,13,14}C. Obviously, this covered atomic scope that was broadened to proton distribution, which presents another way to explain *Z* that was shown to occupy constant spatial positions not only in nuclei, but in molecules (Figure 2b).

In conclusions, the compelling evidences suggest that a special shape of the periodic table is rooting in atomic nuclei that can only grow 1 α-particle in the 1st layer intensified by 4 p_I of $_{27}$Co, $_{28}$Ni, $_{45}$Rh, and $_{46}$Pd, and then grow 2^3, 2^4, and 2^5 α-particles together with nearly same number valence neutrons in the 2-3, 4-5, and 6-7 layers, respectively, that noble nuclei demonstrated perfect nucleon distributions, which is well consistent with the line of beta stability. Furthermore, the number of the elements [$2(2^3+2^4+2^5)$ besides groups 9-10B] and valence neutrons ($2^3+2^4+2^5$) in the 2-3, 4-5, and 6-7 steps being a square relation therefore indicates that a nucleus unusually is a two-dimensional structure in a nuclear phase, a folding nucleon disc that may be the heavier, the flatter, a possible reason resulting in super heavy element lives becoming shorter and shorter. Also, so that gives rise to it, a crude nucleon aspect was seemingly suggested from macrocosm. However, though here is an empirical nucleon distribution that could avoid stuck on details to some extent, it provides a visible nuclear image for the first time, which will benefit to further clarify and/or integrate nuclear, atomic, and molecular structures. It is significant, especially, in the present nanoparticle time.

Acknowledgments

This work was partly supported by Changzhou bureau of science and technology, China. The author thanks Mr. Benlin Liu for a suggestion.

References

Amiel, S. (1969). Delayed neutrons in fission. In *Proceedings of the Second IAEA Symposium on the Physics and Chemistry of Fission held by the International Atomic Energy Agency in Vienna* (Vol. 28, pp. 569-590).

Bemis Jr, C. E., Ferguson, R. L., Plasil, F., Silva, R. J., Pleasonton, F., & Hahn, R. L. (1977). Fragment-mass and kinetic-energy distributions from the spontaneous fission of No 252. *Physical Review C*, *15*(2), 705.

Bohr, N. (1913). On the constitution of atoms and molecules. *Phil. Mag., 26*, 476-502.

Bohr, N., & Wheeler, J. A. (1939). The mechanism of nuclear fission. *Phys. Rev., 56*, 426.

Bowman, H. R., Milton, J. C. D., Thompson, S. G., & Swiatecki, W. J. (1963). Further studies of the prompt neutrons from the spontaneous of ^{252}Cf. *Phys. Rev., 129*, 2133.

CERN. (2004). *ISOLDE goes on the trail of superlatives*. CERN Courier May 4.

Delaune, O. (2013). Isotopic yields distributions of transfer- and futon-induced fission from ^{228}U + ^{12}C reactions in inverse kinematics. *Phys. Rev. C, 88*, 024605.

Fluss, M. J., Kaufman, S. B., Steinberg, E. P., & Wilkins, B. D. (1973). Angular distribution of alpha particles in the spontaneous fission of ^{252}Cf. *Phys. Rev. C, 7*, 353.

Flynn, K. F., Gindler, J. E., & Glendenin, L. E. (1975). Distribution of mass in thermal-neutron-induced fission of ^{257}Fm. *Phys. Rev. C, 12*, 1478.

Gindler, J. E., Flynn, K. F., Glendenin, L. E., & Sjoblom, R. K. (1977). Distribution of mass, kinetic energy and neutron yield in the spontaneous of ^{254}Fm. *Phys. Rev. C, 16*, 1483.

Hafstod, L. R., & Teller, E. (1938). The alpha-particle model of the nucleus. *Phys. Rev., 54*, 681.

Hahn, O. (1921). Über ein neues radioaktives Zerfallsprodukt im Uran. *Naturwissenschaften*, *9*(5), 84-84.

Haxel, O., Jensen, J. H. K. & Suess, H. E. (1949). On the “magic numbers” in nuclear structure. *Phys. Rev., 75*, 1766.

Iyer, R. H., & Cobble, J. W. (1966). Evidence of ternary fission at lower energies. *Phys. Rev. Lett., 17*, 541-545.

Jones, S. E., Palmer, E. P., Czirr, J. B., Decker, D. L., Jensen, G. L., Thorne, J. M., ... & Rafelski, J. (1989). Observation of cold nuclear fusion in condensed matter. *Nature*, *338*(6218), 737-740.

Klingensmith, D. L., & Porile, N. T. (1988). Fragment emission in the interaction of ^{238}U with 400 Gev protons. *Phys. Rev. C, 38*, 818.

Konecny, E., Specht, H. J., & Weber, J. (1973). Symmetric and asymmetric fission of Ra- and Ac-isotopes. *Proc. IAEA Symp. Phys. Chem. Fission, 2*, 3-18.

Lewis, G. N. (1916). The atom and the molecule. *J. Am. Chem. Soc., 38*, 762.

Moseley, H. G. J. (1913). The high frequency spectra of the elements. *Phil. Mag., 26*, 1024.

Muga, M. L., Rice, C. R., & Sedlacek, W. A. (1967). Ternary fission of heavy nuclei. *Physical Review Letters*, *18*(11), 404-408.

Piasecki, E., & Nowicki, L. (1979). Polar emission in fission. In *Physics and chemistry of fission* (pp. 193-221).

Piasecki, E., Dakowski, M., Krogulski, T., Tys, J., & Chwaszczewska, J. (1970). Evidence of the polar emission of alpha-particles in the thermal neutron fission of 235U. *Physics Letters B*, *33*(8), 568-570.

Poenaru, D. N., Ivascu, M., & Sandulescu, A. (1979). Alpha-decay as a fission-like process. *J. Phys. G: Nucl. Phys., 5*(10), L169-L173.

Rose, H. J., & Jones, G. A. (1984). A new kind of natural radioactivity. *Nature, 307*, 245.

Schmitt, H. W., Neiler, J. H., Walter, F. J., & Chetham-Strode, A. (1962). Mass distribution and kinetics of ^{235}U thermal-neutron-induced three-particle fission. *Phys. Rev. Lett., 9*, 427.

Thomas, T. D., & Vandenbosch, R. (1964) Correlation of fission-fragment kinetic-energy fine structure with a semiempirical surface. *Phys. Rev., 133*, B976.

U.S. National Nuclear Data Center. (n.d.). *Nudat 2*.

Unik, J. P., Gindler, J. E., Glendenin, L. E., Flynn, K. F., Gorski, A., & Sjoblom, R. K. (1974). Fragment mass and kinetic energy distributions for fissioning systems ranging from mass 230 to 256. In *Physics and chemistry of fission* (pp. 19-46).

Wild, J. F., Baisden, P. A., Dougan, R. J., Hulet, E. K., Lougheed, R. W., & Landrum, J. H. (1985). Light-charged-particle emission in the spontaneous fission of ^{250}Cf, ^{256}Fm and ^{257}Fm. *Phys. Rev. C, 32*, 488.

Applied Physics Research; Vol. 9, No. 6; 2017
ISSN 1916-9639 E-ISSN 1916-9647
Published by Canadian Center of Science and Education

Can the Planck Length Be Found Independent of Big G?

Espen Gaarder Haug[1]

[1] Norwegian University of Life Sciences, Norway

Correspondence: Espen Gaarder Haug, Norwegian University of Life Sciences, Norway. E-mail: espenhaug@mac.com

Received: May 22, 2017 Accepted: June 24, 2017 Online Published: November 12, 2017

doi:10.5539/apr.v9n6p58 URL: https://doi.org/10.5539/apr.v9n6p58

Abstract

In this paper we show how it is possible to measure the Planck length through a series of different methods. One of these measurements is totally independent of big G, but moving from the theoretical realm to the empirical realm would require particle accelerators far more powerful than the ones that we have today. However, a Cavendish-style experiment can also be performed to find the Planck length with no knowledge of the value of big G. Furthermore, the Cavendish style set-up gives half of the relative measurement error in the Planck length compared to the measurement error in big G.

Keywords: Planck length, independent of big G, maximum velocity, Cavendish-style experiment, gravity, orbital velocity, gravitational red-shift, deflection of light, Planck constant, speed of light, mass

1. Introduction and Challenge

The Planck length was first introduced by Max Planck in 1906, see (Planck, 1906), and is given as

$$l_p = \sqrt{\frac{\hbar G}{c^3}} \approx 1.616229 \times 10^{-35} \text{ meter} \tag{1}$$

This shows the Planck length as a function of Newton's (1686) big G, the reduced Planck constant, and the speed of light. Haug (2016a, 2016b, 2016c) has recently suggested that big G is a universal composite constant that can be written in the form

$$G = \frac{l_p^2 c^3}{\hbar} \tag{2}$$

Using this formula for big G simplifies and quantifies a long series of equations in Newton's and Einstein's conception of gravity. It has recently come to our attention that (McCulloch, 2014) has derived a similar formula for big G based on Heisenberg's uncertainty principle (Heisenberg, 1927)

$$G = \frac{\hbar c}{m_p^2} \tag{3}$$

Since $m_p = \frac{\hbar}{l_p}\frac{1}{c}$ the (McCulloch, 2014) and the (Haug, 2016a) formulas are basically the same

$$\cdot\, G = \frac{\hbar c}{m_p^2} = \frac{\hbar c}{\left(\frac{\hbar}{l_p}\frac{1}{c}\right)^2} = \frac{l_p^2 c^3}{\hbar} \cdot \tag{4}$$

Formula (4) can naturally be found by simply rewriting the Planck length formula (1) with respect to big G. However, (Haug, 2016b) has also derived this formula from dimensional analysis as well as from Heisenberg's uncertainty principle, using his newly-introduced maximum velocity formula for matter (Haug, 2017). McCulloch has derived his formula from Heisenberg's uncertainty principle as well, but relies on a very different method. The argument in favor of writing big G in this way is grounded in the fact that it helps us quantize and simplify a long series of formulas from Einstein's and Newton's gravitational theories without changing their values.

Both of these proposed formulas (Haug and McCulloch) for big G may be criticized for appearing to lead to circular arguments that have no solution, at least at first glance. Until recently, the Planck length has only been known to be found by using big G. From this perspective, the Planck length seems to be a derived constant from the more fundamental constant, big G. Therefore, it may not seem sound to claim that big G can be a function of the Planck length. Here we will challenge this view by pointing out several ways of finding the Planck length independently of knowing big G.

2. The Planck Length Totally Independent of Big G

Haug (2016d, 2016e, 2016f, 2017) has suggested that there may be a maximum velocity for matter just below the speed of light given by

$$v_{max} = c\sqrt{1 - \frac{l_p^2}{\bar{\lambda}^2}} \tag{5}$$

This formula can be derived by assuming that the reduced Compton wavelength can never be shorter than the Planck length, or that the maximum frequency we can observe on relativistic Doppler shift is the Planck frequency. The formula has also been derived from the recent progress in mathematical atomism. Haug (2014) has shown that all of Einstein's special relativity mathematical end results can be derived from atomism when using Einstein-Poincarè synchronized clocks. He assumes that the diameter of the smallest possible fundamental particle is the Planck length and that this particle makes up all energy and matter; this must not be confused with the standard view of particles.

Assuming that this is the maximum velocity of anything with rest-mass also seems to solve a series of infinity challenges in modern physics. It gives a limit on the maximum kinetic energy for a subatomic particle, as well as a maximum on the momentum and on the proper velocity for anything with rest-mass. Haug has further shown that the absence of such a speed limit leads to absurd possibilities, such as a single electron with a relativistic mass equal to that of the Sun, or even an entire galaxy. If a single electron like this ever hit the Earth, the Earth would be pulverized. Clearly, this has not happened in the billions of years the Earth has existed and indicates that there must be an exact upper boundary on the velocity on the electron that falls below the speed of light.

The maximum velocity formula given by Haug can be solved with respect to the Planck length.

$$l_p = \bar{\lambda}\sqrt{1 - \frac{v_{max}^2}{c^2}} \tag{6}$$

The reduced Compton wavelength of an electron can also be found independently of big G, see (Prasannakumar, Krishnaveni, & Umesh, 2012). v_{max} had to be observed experimentally to find the Planck length.

Calculations show that this maximum velocity for any known observed subatomic particle (such as an electron) is just below the speed of light, but far above the rate that has been attained for particle acceleration in the Large Hadron Collider (LHC), for example. In other words, this new way of observing the Planck length is only a theory at this time. However, if we assume that this represents the maximum velocity of anything containing matter, then we will find that a series of infinity's challenges in physics will disappear, see (Haug, 2016f).

Furthermore, recent developments in mathematical atomism strongly strengthen our suspicion that the Planck length is one of the most fundamental constants. All of Einstein's special relativity equations and a series of additional equations have been derived simply by assuming that everything consists of indivisible particles always traveling at the speed of light in the void (empty space). First, when linking the diameter of this particle with the Planck length we are able to get the mass of the electron consistent with the reduced Compton wavelength of the electron under a theory derived from atomism. Atomism is also one of several ways to calculate the maximum velocity of anything with rest-mass.

3. Planck Length from a Cavendish-Style Set-Up

We can easily set up a Cavendish-style (Cavendish, 1798) experiment (even with a low budget) and find the Planck length without direct knowledge of big G. Further, we need no knowledge of the mass of the Earth or any other cosmological objects. The Cavendish experiments consist of first finding the weight of four balls, two small ones and two large ones. These balls can consist of any element, but here we will use an example of lead balls. The mass of these balls can be found by taking a weight at the surface of the Earth, or one could use the Watt Balance, see (Stock, 2011), for example. The two small lead balls are placed at a distance of L apart on a rod that we will hang on a wire. We leave the two heavier lead balls in a stationary position next to each of the smaller lead balls.

For a full understanding of the set-up, we recommend reading about the Cavendish experiment; see Cavendish 1798, for the original description; many other sources are available in books and online.

We will call the distance between centers of the large and small balls (when the balance is deflected) r. The period of oscillation of torsion balance is measured as T. If we have an accurate estimate of the Planck constant and know the value of the speed of light[1] through other experiments, we can now directly find the Planck length from the Cavendish-style experiment by using the following formula

$$l_p = \sqrt{\frac{\hbar 2\pi^2 L r^2 \theta}{MT^2 c^3}} \tag{7}$$

where θ is the angle in radians of deflection of the torsion balance beam from its rest position. (See Appendix A for a full derivation of this formula when not relying on big G at all). This is basically the same experiment that Cavendish performed. Cavendish did not actually calculate big G, but used his experiment to find the density of the Earth and thereby determine the weight of the Earth. One could imagine that the Planck constant and the speed of light had been measured and were well-known before anyone had figured out the value of big G.

In such a case, one could come up with the gravitational formula $F = \frac{l_p^2 c^3}{\hbar}\frac{MM}{r^2}$ without knowing big G and the unknown we would be searching for would be the Planck length and not big G.

Before the development of Newton's theory of gravitation, if one assumed that gravity had to travel with the speed of light then it would be natural to think that one needed to include the speed of light somehow in the formula for gravity. Now, in our view, the speed of light is embedded even within Newton's formula inside big G.

We can actually measure the Planck length from the kitchen table using a small size Cavendish-style set-up, likely with less than a 5% error. One can build such an apparatus for a few dollars in materials, or one can buy a ready-to-use commercial ``home-kit'' for a few thousand dollars. A small-size armature Cavendish-style set-up can measure big G to an accuracy of $\pm 10\%$ or better (depending on the apparatus), and the Planck length to an accuracy that is twice as good at that.

4. The Error in the Newton Gravitational Constant Is Twice the Measurement Error in the Planck Length

To measure the gravitational constant and the Planck length is, in many ways, two sides of the same coin, particularly under the view that Newton's gravitational constant is a composite constant that is a function of the Planck length. When using any form of gravitational measurement to find the Planck length, we will see that it looks like the measurement error in Newton's gravitational constant should be about twice the error of the measurement in the Planck length.

The partial derivative of big G with respect to the Planck length is given by

$$\frac{\partial G}{\partial l_p} = \frac{2c^3 l_p}{\hbar} \tag{8}$$

In terms of percentage sensitivity in G with respect to the percentage error in the Planck length, we must have

$$\%\text{Sensitivity} = \frac{2c^3 l_p}{\hbar}\frac{l_p}{G\times 100} = \frac{2\frac{l_p^2 c^3}{\hbar}}{G\times 100} = \frac{2}{100} \tag{9}$$

That is for a 1% error in the measurement in the Planck length, we get about a 2% error in the measurement of the gravitational constant. Further, we can partially derive the Planck formula for the Planck length with respect to big G, and we get

$$\frac{\partial l_p}{\partial G} = \frac{\hbar}{2c^3\sqrt{\frac{G\hbar}{c^3}}} \tag{10}$$

This gives us the percentage sensitivity in the Planck length for a percentage point change (error) in big G

$$\%\text{Sensitivity} = \frac{\sqrt{\hbar}}{2\sqrt{Gc^3}}\frac{G}{l_p\times 100} = \frac{\sqrt{\frac{G\hbar}{c^3}}}{l_p\times 200} = \frac{1}{200} \tag{11}$$

That is to say, for each one percent error in the measurement of Newton's gravitational constant we only have about half a percent error in the measurement of the Planck length. One could argue that for the Planck length we have uncertainty in the Planck constant that will affect the uncertainty of the Planck length. This is true, but the uncertainty in the Planck constant is almost negligible. If we take into account three standard deviations in the uncertainty of the Planck constant[2] (from 2014 CODATA), we get a percentage error in the Planck length of only ±0.00002304%. The one standard deviation relative error is only about $-7.68084199413574 \times 10^{-08}$. This is negligible compared to the known relative standard error in the Planck length.

We can also indirectly see from the CODATA 2014 reported standard errors that the measurement error (as measured in percentage of the constant) is twice as large for Newton's gravitational constant as it is for the Planck length. For big G, the CODATA reports a standard error of $0.000\ 31 \times 10^{-11}$ $m^3\ kg^{-1}\ s^{-2}$, in percentage of the gravitational constant that is a relative standard error of 4.65×10^{-05}. And for the Planck length, the CODATA reports a standard error of $0.000\ 038 \times 10^{-35}$ and a relative standard error of 2.3×10^{-5}. It is no coincidence that the relative standard error in the Planck length is basically half of the standard error for the gravitational constant; it comes from the relationship between them.

5. The Planck Length from Orbital Velocity

We can also find the Planck length from orbital velocity. The orbital velocity is given by

$$v_o = \sqrt{\frac{GM}{r}}$$

$$v_o = \sqrt{\frac{\frac{l_p^2 c^3}{\hbar} M}{r}} \tag{12}$$

$$v_o = \sqrt{\frac{l_p^2 c^3 M}{\hbar r}}$$

Solved with respect to the Planck length we get

$$l_p = \sqrt{\frac{v_0^2 \hbar r}{c^3 M}} \tag{13}$$

We can find the Planck length from knowing the orbital velocity of a satellite. This again would require knowledge of the mass of the Earth (or the mass we are measuring orbital velocity around). We could easily find the mass of the Earth by performing the Cavendish experiment and finding the Planck length before calculating big G based on the Planck length, the Planck constant, and the speed of light.

Assume a human-made satellite is orbiting the Earth at an altitude of 600 *km* and at a measured orbital velocity of 7561.36 *m/s*. Since the radius of the Earth is about 6,371 *km*, this gives a radius of the satellite (relative to the center of the mass it is orbiting) of 6,971,000 meters. The mass of the Earth is 5.972×10^{24} *kg*. This gives us the input to find the Planck length

$$l_p = \sqrt{\frac{v_0^2 \hbar r}{c^3 M}} = \sqrt{\frac{7561.36^2 \times \hbar \times 6{,}971{,}000}{c^3 \times 5.972 \times 10^{24}}} \approx 1.6162 \times 10^{-35}\ \text{m}$$

Again one can argue that we need to know big G to know the mass of the Earth and that we are entering in a circular argument. However, the bottom line here is that we can find the Planck length, the Planck constant, and the speed of light independent of any knowledge of big G. Further, the mass of fundamental particles can be found simply by knowing their reduced Compton wavelength, which can be found by Compton scattering.

6. The Planck Length from the Gravitational Acceleration Field

We can also find the Planck length from the gravitational acceleration field.

$$l_p = r\sqrt{\frac{g\hbar}{c^3 M}} \tag{14}$$

For Earth, the gravitational acceleration field at the surface is about 9.807 m/s^2. From this plus the radius and mass of the Earth we know the Planck length

$$l_p = 6371000\sqrt{\frac{9.807 \times \hbar}{c^3 \times 5.972 \times 10^{24}}} \approx 1.61519 \times 10^{-35}$$

7. The Planck Length from Gravitational Light Deflection

By assuming $G=\frac{l_p^2c^3}{\hbar}$ we can rewrite Einstein's gravitational light deflection formula

$$\begin{aligned}\delta &= \frac{4GM}{c^2r}\\ \delta &= \frac{4\frac{l_p^2c^3}{\hbar}M}{c^2r}\\ \delta &= \frac{4l_p^2Mc}{\hbar r}\end{aligned} \tag{15}$$

This we can solve with respect to l_p, which gives us

$$l_p = \sqrt{\frac{\hbar r\delta\frac{\pi}{648000}}{4Mc}} \tag{16}$$

where $\delta$is the observed bending of light in arcseconds, r is the radius from the center of the mass bending on the light to the point at which the light passes the object, M is the mass of the object, c is the speed of light, and $\hbar$is the reduced Planck constant.

To give an example: for the Sun, the observed light bending is 1.75 arcseconds or 1.75/3600 of a degree. The radius of the sun is 696,342,000 meters and the mass of the Sun is $M_S \approx 1.98810^{30}$ *kg*. We can plug this into the formula above and obtain

$$l_p = \sqrt{\frac{\hbar r_s\delta_s\frac{\pi}{648000}}{4M_sc}} = \sqrt{\frac{\hbar\times 696342000\times 1.75\times\frac{\pi}{648000}}{4\times 1.988\times 10^{30}\times c}} \approx 1.6162\times 10^{-35}\ \text{m}$$

8. The Planck Length from Gravitational Red-Shift

Gravitational deflection is hard to measure very accurately. The technology used to measure gravitational red-shift is (likely) much more accurate. This involves gravitational time dilation that can be measured with very accurate optical clocks today. In a weak gravitational field (like we have on the Earth and that also exists on the surface of the Sun) we have

$$\begin{aligned}\lim_{r\to+\infty} z(r) &\approx \frac{2GM}{c^2r}\\ \lim_{r\to+\infty} z(r) &\approx \frac{2\frac{l_p^2c^3}{\hbar}M}{c^2r}\\ \lim_{r\to+\infty} z(r) &\approx \frac{2l_p^2Mc}{\hbar r}\end{aligned} \tag{17}$$

Solved with respect to the Planck length we get

$$l_p = \sqrt{\frac{\hbar r z(r)}{2Mc}} \tag{18}$$

We could even measure the gravitational red-shift between two different altitudes on the surface of the Earth, on smaller sized objects like the Moon, or even onboard a large spherical space station. For the gravitational red-shift measured from two different radius related to the same mass (object), we have the following formula that works very well in weak gravitational fields

$$\frac{\lambda_2-\lambda_1}{\lambda_1}\approx\frac{1+\frac{2GM}{c^2r_1}}{1+\frac{2GM}{c^2r_2}}-1$$
$$\frac{\lambda_2-\lambda_1}{\lambda_1}\approx\frac{1+\frac{2\frac{l_p^2c^3}{\hbar}M}{c^2r_1}}{1+\frac{2\frac{l_p^2c^3}{\hbar}M}{c^2r_2}}-1 \tag{19}$$
$$\frac{\lambda_2-\lambda_1}{\lambda_1}\approx\frac{1+\frac{2\frac{l_p^2c}{\hbar}M}{r_1}}{1+\frac{2\frac{l_p^2c}{\hbar}M}{r_2}}-1$$

Solved with respect to the Planck length we get

$$l_p=\sqrt{\frac{\frac{\lambda_2-\lambda_1}{\lambda_1}\hbar r_1r_2}{2cMr_2-2cMr_1-2\frac{\lambda_2-\lambda_1}{\lambda_1}cMr_1}} \tag{20}$$

In other words, we can find the Planck length simply from gravitational red-shift observations, the mass of the object, the reduced Planck constant, and the speed of light.

8. Table Summary

In the table below we show a series of formulas related to different types of measurements that can be used to measure the Planck length

Table 1. Ways to Find the Planck Length

Ways to find the Planck length	**Planck length formulas**	**Comments**
Traditional Max Planck Formula	$l_p=\sqrt{\frac{G\hbar}{c^3}}$	Directly dependent on big G.
Maximum velocity of subatomic particles	$l_p=\bar{\lambda}\sqrt{1-\frac{v_{max}^2}{c^2}}$	No need for big G in calculation, but v_{max} above current accelerators.
Cavendish-style experiment	$l_p=\sqrt{\frac{\hbar 2\pi^2Lr^2\theta}{MT^2c^3}}$	Can be done from kitchen table.
Orbital velocity	$l_p=\sqrt{\frac{v_0^2\hbar r}{c^3M}}$	Easy to do from Earth's surface.
Gravitational acceleration field	$l_p=r\sqrt{\frac{g\hbar}{c^3M}}$	Easy to do from Earth's surface.
Gravitational red-shift	$l_p=\sqrt{\frac{\hbar rz(r)}{2Mc}}$	Easy to do from Earth's surface.
Gravitational deflection	$l_p=\sqrt{\frac{\hbar r\delta}{4Mc}}$	Solar deflection observed from Earth.

Note. In the table above we show a series of formulas related to different types of measurements that can be used to measure the Planck length elsewhere in the article.

8. Conclusion

We have shown how the Planck length can be found through a number of methods including a Cavendish-style experiment, the orbital velocity, the gravitational acceleration field, the gravitational red-shift, and the gravitational deflection. To do this we need to know the mass of the object, the reduced Planck constant, the speed of light, and the radius related to the measurements. We have also shown that one can find the Planck length from the newly-introduced maximum velocity of something with rest-mass.

The notation in Newton's gravitational constant offers a hint that it is a universal composite constant rather than a fundamental constant. It makes sense when we have meters and time, that the Planck length is the shortest length unit that can ever be measured. The speed of light is the fastest rate at which something can travel and it consists of distance divided by time. The Newton gravitational constant is in the form $m^3\,kg^{-1}\,s^{-2}$ – it seems unlikely that anything at the very deepest level should be meters cubed divided by *kg* and seconds squared.

The gravitational constant is a composite (derived) constant, while the Planck length represents something physical; it is the shortest reduced Compton wavelength possible. According to recent developments in mathematical atomism, there are also strong indications that the Planck length is the diameter of the only truly fundamental particle, namely an indivisible particle that together with void is making up all matter and energy, see (Haug, 2014, 2016f).

Acknowledgments

Thanks to Victoria Terces for helping me edit this manuscript and thanks to Mike McCulloch and Eric Thompson for useful comments.

References

Cavendish, H. (1798). Experiments to determine the density of the Earth. By Henry Cavendish, Esq. FRS and AS. *Philosophical Transactions of the Royal Society of London*, *88*, 469-526.

Haug, E. G. (2017). *A Suggested Boundary for Heisenberg's Uncertainty Principle*. Retrieved from http://vixra.org/abs/1701.0497

Haug, E. G. (2014). *Unified Revolution: New Fundamental Physics*. Oslo: E.G.H. Publishing.

Haug, E. G. (2016a). Planck Quantization of Newton and Einstein Gravitation. *International Journal of Astronomy and Astrophysics*, *6*(02), 206.

Haug, E G. (2016b). The gravitational constant and the Planck units. A simplification of the quantum realm. *Physics Essays*, *29*(4), 558-561.

Haug, E. G. (2016c). *Planck Quantization of Newton and Einstein Gravitation for Planck Masses and Smaller Size Objects.* Retrieved from www.viXra.org 1610.0328 2017

Haug, E. G. (2016d). *A New Solution to Einstein's Relativistic Mass Challenge Based on Maximum Frequency*. Retrieved from http://vixra.org/abs/1609.0083

Haug, E. G. (2016e). *Deriving the Maximum Velocity of Matter from the Planck Length Limit on Length Contraction*. Retrieved from http://vixra.org/abs/1612.0358, 2016

Haug, E. G. (2016f). *The Planck Mass Particle Finally Discovered! Good bye to the Point Particle Hypothesis!* Retrieved from http://vixra.org/abs/1607.0496

Haug, E. G. (2017). The ultimate limits of the relativistic rocket equation. The Planck photon rocket. *Acta Astronautica*, *136*, 144-147.

Haug, E. G. (2017b). *Newton's $E = mc^2$ Two Hundred Years Before Einstein? Newton = Einstein at the Quantum Scale*. Retrieved from http://vixra.org/abs/1706.0371

Heisenberg, W. (1927). Über den Anschaulichen Inhalt der Quantentheoretischen Kinematik und Mechanik. *Zeitschrift für Physik, 43*.

McCulloch, M. E. (2014). Gravity from the Uncertainty Principle. *Astrophysics and Space Science, 349*(2).

Newton, I. (1686). *Philosophiae Naturalis Principia Mathematica*. London.

Planck, M. (1906). *The Theory of Radiation*. Dover 1959 translation.

Prasannakumar, S., Krishnaveni, S., & Umesh, T. K. (2012). Determination of Rest Mass Energy of the Electron by a Compton Scattering Experiment. *European Journal of Physics, 33*(1).

Stock, M. (2011). The Watt Balance: Determination of the Planck Constant and Redefinition of the Kilogram. *Philosophical Transactions of the Royal Society of London, 369*.

Notes

Note 1. The speed of light is exact by definition.

Note 2. CODATA 2014 gives a Planck constant of $6.626070040\times10^{-34}$, and a one standard error of $0.000000081 \times 10^{-34}$.

Appendix A: The Planck Length Found Directly from a Cavendish Apparatus

From a Cavendish apparatus one can surprisingly find the Planck length directly without any knowledge of big G. A Cavendish apparatus consist of two small balls (made of lead, for example) and two larger balls. The torque is given by

$$\kappa\theta \tag{21}$$

where κ is the torsion coefficient of the suspending wire and θ is the deflection angle of the balance. We have the following well-known relationship

$$\kappa\theta = LF \tag{22}$$

where L is the length between the two small balls in the apparatus and F is the gravitational force given by the Newton formula, but also by the alternative gravitational constant-less formula, see (Haug, 2017b)

$$F = G\frac{Mm}{r^2} = \frac{Mc^2}{r}\frac{m}{m_p}\frac{l_p}{r} \tag{23}$$

One could easily imagine that someone had suggested the last part of formula (23) as a formula for gravity instead of the Newtonian version with a gravitational constant. In the last part of formula (23), however, we have what would be the unknown Planck length and the Planck mass; could we find them without any reliance on big G?

From equation (22) and (23) we must have

$$\kappa\tau = L\frac{Mc^2}{r}\frac{m}{m_p}\frac{l_p}{r} \tag{24}$$

Further, the natural resonant oscillation period of the torsion balance is given by

$$T = 2\pi\sqrt{\frac{I}{\kappa}} \tag{25}$$

The moment of inertia I of the balance is given by

$$I = m\left(\frac{L}{2}\right)^2 + m\left(\frac{L}{2}\right)^2 = 2m\left(\frac{L^2}{2}\right) \tag{26}$$

This means we have

$$T=2\pi\sqrt{\frac{mL^2}{2\kappa}} \tag{27}$$

And solved with respect to κ this gives

$$\begin{aligned}\frac{T^2}{2^2\pi^2} &= \frac{mL^2}{2\kappa}\\ \kappa &= \frac{mL^2}{2\frac{T^2}{2^2\pi^2}}\\ \kappa &= \frac{mL^2 2\pi^2}{T^2}\end{aligned} \tag{28}$$

Next we are replacing this expression for κ into equation (24) and solving with respect to the Planck length

$$\frac{mL^2 2\pi^2}{T^2}\theta = L\frac{Mc^2}{r}\frac{m}{m_p}\frac{l_p}{r}$$

$$\frac{mL^2 2\pi^2}{T^2}\theta = L\frac{Mc^2}{r}\frac{m}{\frac{\hbar}{l_p}\frac{1}{c}}\frac{l_p}{r}$$

$$\frac{\hbar L 2\pi^2 r^2}{Mc^3 T^2}\theta = l_p^2$$

$$l_p = \sqrt{\frac{\hbar L 2\pi^2 r^2 \theta}{Mc^3 T^2}} \tag{29}$$

Be aware that *M* here is the mass of the large lead balls in the Cavendish apparatus, not the mass of the Earth. All we need to find the mass of the large balls is an accurate weight. The Planck constant can be measured by a Watt Balance experiment, for example, and the speed of light is given. The point is that we can find the Planck length with no knowledge of the gravitational constant.

After we have found the Planck length, we can find the mass of the Earth by measuring the gravitational acceleration of an object and then using the formula

$$M = \frac{gr^2\hbar}{l_p^2 c^3} \tag{30}$$

From this we can easily calculate the orbital velocity of the Moon around the Earth, or any other gravitational calculation we are interested in. Our approach has the strength that the Planck length is something we can logically understand. It is a length and likely is linked to the smallest relevant length in the universe. On the other hand, what is the gravitational constant, this exotic animal that is meters cubed divided by kg and seconds squared (m^3 kg^{-1} s^{-2})? It is difficult to get any intuition from the gravitational constant alone, except from understanding that it is a constant we can measure empirically and use to get Newton's formula to match actual observations. By looking at it as a composite constant, we can break it down into its more fundamental parts, all of which can be measured without big G.

In fact, we need no knowledge of big G to do any of the gravitational calculations. The smallest of all lengths is far too small to be seen, even using the most advanced electron microscope. Suprisingly, the smallest of all lengths can easily be measured from the kitchen table using a miniature Cavendish experiment plugged into a computer. In our wonderful modern age, ancient mechanical technology like the Cavendish apparatus can be combined with high-precision electronics to measure milliradians and time data that are fed straight into the computer and then the Planck length is revealed at last.

Applied Physics Research; Vol. 9, No. 6; 2017
ISSN 1916-9639 E-ISSN 1916-9647
Published by Canadian Center of Science and Education

Dilation of Time Dilation

Tadeusz Wajda[1]

[1] Polytechnic University Krakow, Poland

Correspondence: Tadeusz Wajda, Polytechnic University Krakow, Poland. E-mail: tadeuszwajda@outlook.com

Received: September 29, 2017 Accepted: October 20, 2017 Online Published: November xx, 2017

doi:10.5539/apr.v9n6p67 URL: https://doi.org/10.5539/apr.v9n6p67

Abstract

The study addresses the issue of the so-called time dilation in the sense of the origin of its creation and the physical existence.

Based on the work of Lorentz, who the lack of displacement of interference fringes in the Michelson interferometer explained wrongly with, shortening one arm of the interferometer, I propose the construction of the light pulse clock, in which to measure the rate of the passage of time is used constancy speed of light in vacuum.

Light clock, the construction of which is described in the paper, stationary in relation to the ether, will measure constant time intervals. The same clock transported, will slow down the pace of his walk as a function of transportation speed v and that is a novelty, will slow depending on its orientation relative to the direction of motion. Light clock transported transversely with respect to the stationary clock will slow gamma times, transported lengthwise will slow gamma to the second power.

Basing on the obtained dependences I maintain that time dilation defined in the theory of relativity (SR) as the slowing of the lapse of time, does not physically exist and identification the varying pace of walk clock with the pace of lapse of time I consider a fundamental error resulting from the postulates of this theory.

1. Introduction

In 1881, Mr. Michelson (Michelson, 1881; Michelson & Morley, 1887) constructed an interferometer, whose aim was to demonstrate the existence of ether or medium in which and against which, propagates light.

Interferometer consisted of two mutually perpendicular arms with a length of about 1.2 m each, at the ends of whom where mounted mirrors. Two light rays derived from the same source, distributed on a semi-permeable mirror, ran in these two optical systems back and forth and interfered with each other on that separating them before mirror.

Michelson foresaw that if the ether exists and a terrestrial globe turns in it, it should, obtain the movement of bands originated from the interference of these two waveforms. Assuming that if "ether wind" blowing perpendicular to one arm interferometer, that the wind has to blow parallel to the other. After turning the device by 90 degrees, arms somehow turns into functions. Longitudinal frame becomes transverse and transverse - longitudinal.

Unfortunately, the measurements did not show noticeable movements interference fringes. Later measurements made by Michelson and Michelson (1887) with the participation of Morley in 1887 for the interferometer with arm lengths of about 11 m, also the zero offsets results confirmed.

Then scientists intensively searched for lack of those movements.

Then Mr. Lorentz who interpreted this phenomenon as occurring in a stationary ether, analyzed the layout and calculated the times of passage of the light rays in the two mutually perpendicular arms (Lorentz ether theory, 2017). These times he found different. Time of ray flight in the arm "longitudinal" was for him longer and the transverse section - shorter.

Lorentz divided these times by themselves and as a result of division has acquired one of the best known patterns later on so-called "Beta" or also "Lorentz factor". Or “gamma”, algebraic inverse of the Beta. This pattern has the form:

$$\text{gamma} = 1 / [(1- (v / c) ^ 2] ^ 0.5$$

Lorentz submitted a new hypothesis that if the length of the longitudinal arm of the interferometer is divided by this factor, it will shorten the frame due to this time of flight of light also will shorten so, then the time waveforms

of light in both arms will be identical. It explained the no transfers interference fringes in the Michelson interferometer. And thus "invented" shortening of the length of the segment being in motion with respect to the ether. This shortening is known under the name of the Lorentz contraction.

Surprisingly, this elucidation however erroneous, in the absence of other explanations, has been approved by many contemporary Lorentz scholars.

A dozen years later, in 1905, Mr. Einstein, pretending not heard of Michelson or Lorentz, β published work commonly known under the name of "Special Relativity" (SR) (Einstein, 1905; Wielka encyklopedia powszechna PWN, 2017; Wydawnictwo Naukowe PWN, 2017). Works based on his postulate of constancy of the velocity of light 'in a vacuum' and the independence of this velocity of speed of light source. Asked in relation to which the speed of light in a vacuum has a constant value, replied that light has a constant speed in a vacuum in relation "to everything."

In this statement lies the contradiction, because in accordance with the content of the postulate, a source of light in motion, here is the exception. In my opinion, speed of light in vacuum designated in relation to the movable light source is different from the value of c.

Based on these postulates Einstein "guessed" pattern on gamma, invented relativistic time dilation and length contraction. Of course, the coefficient slowing down the lapse of time had identical to the Lorentz form, only that Einstein called it a beta (β), whose reversal was the same as the gamma (γ).

Many years later (2014) the author of this paper proposed a thesis, the atmospheric air is a stationary medium, form of the ether in relation to whose speed of light is constant in all directions.

It follows a conclusion that the experience of the Michelson type, carried out in still air, in a dark basement, under pressure close to atmospheric pressure at sea level, and did not have right to demonstrate any difference in the speed of light in the air, which depends on the direction of propagation of light.

Therefore, with respect to the ambient air, the interferometer arms remain stationary. When we carry it in the air, or put an instrument in a wind tunnel, then anisotropy of light velocity and displacement of interference fringes will appear.

They will be also present in interferometer working in the air under reduced pressure, which in the years 1905 - 1923 provided evidence Mr. Dayton Miller performing identical measurements to Michelson at the top of Mt Wilson in California (Miller, 1925).

Mr. Einstein uncritically extrapolated a constancy speed of light in air, to vacuum and ignored measurements of Miller, which showed a non-zero offset values.

2. The Light Pulse Clock

By way of construction of the Michelson interferometer we can build a light pulse clock.

Principle of operation and construction of this clock is relatively simple. The clock consists of a pulsed light source and a mirror placed at a distance L from it, on which emitted pulse of light is reflected and returns to the source. The time interval of flight of the light back and forth, in a vacuum, can be a very good standard unit of time.

In this context, I understand the material or non-material medium filling the space in relation to whose light propagates in all directions at a constant speed c. Each medium has electromagnetic parameters; μ and ε, and the speed of light is dependent on them.

The medium for this light is of course also vacuum. Because it has the smallest known in nature numeric values μ and ε, therefore compared with other centers, speed of light in a vacuum has the greatest value.

The mathematical form of this function for electromagnetic waves foresaw Mr. Maxwell, before Hertz experimentally confirmed the existence of electromagnetic waves. It has the form $c = \sqrt{1 / \mu\varepsilon}$ (axwell's equations, 2017).

3. Schematic design and operation of the light pulse clock

Light clock consists of rigid rail at one end is installed perpendicular mirror and the other end equipped with a pulsating light source and a light detector to measure the time of flight of the light beam back and forth. Rail, which is the base of this clock has a constant length L.

Schematic design light clock I present in Figure 1

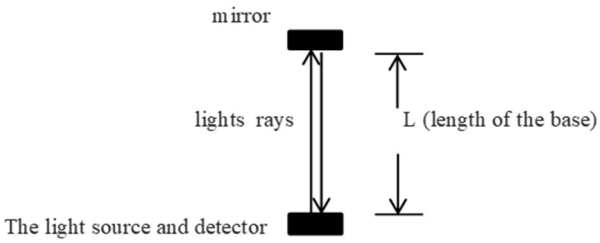

Figure 1

This clock, stationary in relation to the media, will be walked constant pace, depending only on the length L of the base and value of velocity of light c in the medium.

I maintain the same clock which is in relation to the medium in motion, will slow down the pace of his walk otherwise will measure the longer time intervals.

Below I show that light clocks, moving, will be to slow down the pace of their walk not only in dependence on the speed v, but also on their orientation relative to the direction of their movement in medium.

4. Analysis Work of the Stationary Clock

The source sends short light pulse (Figure 1). Spherical wave propagates in all directions with the same speed equal to c. One of the rays of the wave reaches the mirror, from which reflected returns to the place from which emitted. Time T0, of his flight back and forth, is recorded with photodiode installed near to the source of light.

Time T0 interval that will be measured by this clock, will be 'real time' or ‘proper time’ that will be stationary and an independent of the orientation of the clock. It will be equal:

$$T0 = 2L / c \quad [0]$$

Where L - length of the base [m], c - the speed of light 300000 km / s.

If base (we assume) will have a length L = 150000 km, this clock will measure 1 second intervals time. T0 = 1 sec.

we can build a clock with a much shorter base eg. L = 1.5 m. The clock will then ticked time intervals equal: T0 = 2L / c = 2 * 1.5 m / 300,000,000 m / s = 0.00000001 sec or = 1 e-8 sec = 10 ns. This time is to be understood as a time interval of his single "tick".

This clock, we can modify. If instead of a single light pulse generator, we will use similar generator but triggered when the previous pulse returns to the detector and equipped with a pulse counter, counting to a hundred million, we can get to the exit clock, also 1-second intervals, of the “real” time T0. It is real time, because "working" light beam flying from the source to the mirror and back, in a stationary clock runs at the shortest possible way. Light ray will fall onto the mirror and reflect from it exactly at right angles. Such a clock, stationary, will then have the fastest possible pace of walk T0.

5. Analysis of the light clock in motion, in terms of its orientation relative to the direction of his movement.

5.1 Clock transported transversely

We set the clock transversely to the direction of flight of the rocket. Of course, the clock must be installed on the outside of the rocket. Angle ϕ between the base clock and the direction of its movement is equal to ϕ = 90°. The rocket moves at a speed v defined as the ratio of the traveled distance divided by the stationary time.

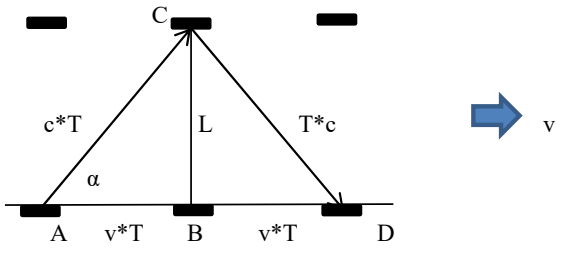

Figure 2

Figure 2 will be helpful in calculating the walking speed of this clock in motion. Pace of walking of this clock Tt, will be function of speed v, its movement with respect to the medium in which light propagates at a constant speed c.

The light pulse emitted by the generator at the point A, runs along the hypotenuse of a right triangle ABC. In the interval T = ½ Tt clock will travel the way AB and at the same time, the light pulse will pass the way AC.

We see that the light beam runs at an angle **α** to the direction of movement of the clock and comes to the detector, which will find at point D moving with speed v.

Considering geometry of flight (triangle ABC) and applying the Pythagorean theorem, we formulate the equation:

$$(0.5\ Tt * c)^2 = (0.5\ Tt * v)^2 + L^2$$

From this we get the flight time of light pulse from the generator (point A) to the mirror (point B) and back to the detector, which finds at point D.

This clock will measure time intervals, let's call them transverse, with time interval Tt, equal:

$$\mathbf{Tt = 2L / (c^2 - v^2)^0.5} \qquad \mathbf{[1]}$$

This clock will walk in relation to a stationary clock slower, because "working" light beam will run along a zigzag line that is along hypotenuses formed by way of light Lc, way vT of clock and constant length L of base (Figure 2).

5.2 Clock moving lengthwise.

The same clock now we set in parallel to the direction of movement. Light pulse emitted from the source (pulse generator) runs to the mirror, which gets away from him in the direction of movement at a speed v. This ray is reflected from mirror and returns to the detector, which "is approaching". This running away and approach are to be understood as a phenomenon of movement in relation to a stationary medium in which light propagates at a constant speed c.

Figure 3 facilitates way of calculation of the walking speed of the clock working as "longitudinal".

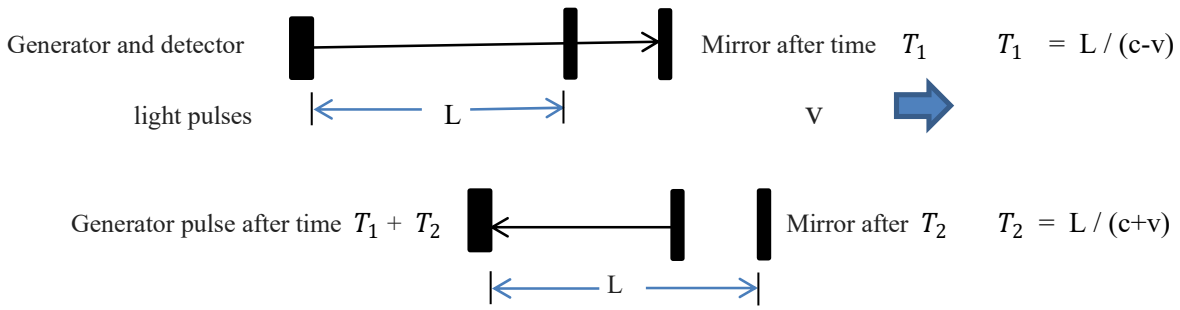

Figure 3

Time Tl of pulse flight back and forth will be equal to the sum of the time intervals T1 and T2.

Clock moving lengthwise, will measure time interval equal

$$Tl = L / (c + v) + L / (c - v).$$

After algebraic transformation, this time interval will be equal to:

$$\mathbf{Tl = 2Lc / (c^2 - v^2)} \qquad \mathbf{[2]}$$

The calculation of the walking speed of the clock section in relation to the walking speed of a stationary clock.

We count how many times slower compared to the clock stationary will walk clock transported with speed v, transversely to direction of its movement.

We divide walking pace [1] by walking pace [0]

$$Tt / T0 = 2L / [c^2 - v^2]^{0.5} / 2L / c = 1 / [1- (v / c)^2]^{0.5}$$

$$\text{Time } Tt = T0 * 1 / [1- (v / c)^2]^{0.5}$$

We note that the value 1 / [1- (v / c) ^ 2] ^ 0.5 is equal to Lorentzian gamma.

$$Tt = T0 * \text{gamma} \quad \text{where gamma} = 1 / [1- (v / c) ^ 2] ^ 0.5$$

Note: The calculation is more convenient if to apply the formula derived by me, based on trigonometric functions.

Since the hypotenuse of the triangle ABC (Figure 2) is equal to L = c * T0 and the hypotenuse of the triangle is equal c * T, so the ratio of these sides cT0 / cT is sine of angle α. After simplifying by the c receive T0 / T = sin α.

$$v*T / T*c = \cos \alpha$$

Angle α = arc cos (v/c)

From this time T = T0 / sin arc cos (v / c).

According to conventional terminology, **gamma = 1 / sin arc cos (v / c).**

An interesting letter time interval T is equal to T = T0 *gamma.

To derive this formula for gamma, you do not need any new assumptions or postulates; classical laws of motion, optics and knowledge of trigonometric functions are sufficient.

The pattern is the same as the classic relativistic pattern,

gamma = 1 / sin arc cos (v / c) == 1 / [1- (v / c) ^ 2] ^ 0.5

6. The calculation of the walking speed of the longitudinal clock

We count how many times slower than a stationary clock, the clock will walk when is transported with a speed v, lengthwise that is in parallel to the direction of its movement.

Divide walking pace [2] by [0]

$$Tl /T0 = 2Lc / [c^2 - v^2] / 2L / c = 1 / [1- (v / c) ^ 2]$$

We note that the ratio of the times is gamma to the second power

The time Tl = T0 * 1 / [1- (v / c) ^ 2]

We have, **Tl = T0 * gamma ^ 2**

In result from the above analysis and calculations that:

Light clock moving and oriented transversely, will slow the pace of his walk in relation to a stationary clock, in accordance with Lorentz, gamma times.

The same clock oriented lengthwise, will slow the pace of his walk, gamma to the second power times!

The concept of “walking pace” should be understood as measured out with this clock time interval T, which compared with interval T0 which is measures with the stationary clock – will always be longer.

From the above it follows that every light clock in motion – will slow down. The rate of slowing down will be a function of speed v and the orientation of the clock in relation to the direction of his movement.

7. A few comments criticisms of the currently valid Special Theory of Relativity

Mr. Einstein is the author or inventor of “time dilation”. He noticed that the clock transported, moving in vacuum with a speed v, it is the same clock, the clock with identical structure like a stationary clock.

His reasoning was the following. Since the same clock, identically constructed, transported with a speed v, slowing down his walk gamma times, well, according to Mr. Einstein, there is no other explanation of this phenomenon, as such, the time in the system of reference in motion, has to slow down the pace of his lapse otherwise must undergo dilation …

I think the greater nonsense it’s even hard to imagine.

8. Argumentation

Light pulse clock, despite identical mechanical design, during its movement, behaves and works significantly different from stationary clock.

In the stationary clock, “working” light beam runs along the shortest possible way, because runs to the mirror at right angles and is reflected from it at the same right angle. So it comes the mirror and returns to the source, along the shortest possible, straight line. Due to this pace of his walk is maximum. Stationary clock will measure the shortest possible time intervals.

The clock transported transversely to the direction of motion, working light ray, runs to the mirror at an angle α, (as defined in relation to the direction of travel and mirror plane). The value of this angle is equal to

$$\alpha = \arccos (v / c).$$

At the same angle α, this ray is reflected from the mirror, but does not return to the point in space from which it was generated. He arrives at the site, which will house the generator (and the detector coupled with), which during the flight of working ray covered distance, s = v * T0.

Unfortunately, the "brilliant" conclusion of Mr. Einstein, it's not the clock slows down his walk, but time slows down his lapse, was by many scientists and world press interpreted as the greatest scientific achievement of the twentieth century.

Especially, with this slowing the lapse of time by Mr. Einstein, can be so large, that this elapse can be stopped. It just suffices to move enough fast. And you can even go back in time, if would manage to exceed the speed of light!

And many contemporaries Einstein scientists believed into those nonsense. And many of our contemporaries scientists still believe in these absurdities.

9. Summary

I proved that the light clock transported transversely to the direction of travel, in relation to the stationary clock slows down his walk gamma times.

I proved that the clock oriented lengthwise to the direction of travel, in relation to the clock transported transversely, slows down his walk again gamma times.

I showed that the light clock oriented lengthwise, in relation to the stationary clock, slows down his walk gamma*gamma times.

These calculations proved that the light clocks slow down their walk depending not only on the transportation speed v, but also depending on their orientation relative to the direction of their movement.

The differences are large; clock oriented transversely slows the pace according with gamma function, while the same clock oriented longitudinally, slows down his walk gamma to the second power.

I stress, the above coefficients gamma determine the walking pace of light clock and not slowing down the passage of time. Time is a material constant therefore his pace elapse can't change.

In the entire Universe time elapses in its constant invariant pace.

Identifying the walking pace of clocks, including "atomic", with the pace of the passage of time, I consider the greatest scientific scam of the twentieth century.

10. Concluding remarks.

For a comparison of the differences between values of normal and square dilation, we assume missile velocity v = 0.1 c. Then gamma "normal" that is specified for the transverse clock, will be equal to 1,005, while gamma "square", or longitudinal, will have a value of 1,005 ^ 2 = 1.01.

For speed v = 0.999 c, the corresponding gamma values will be equal 22.35 and 500.25.

An inquisitive reader will notice that the light clock shown in Figure 1, which is stationary, in the real space intergalactic vacuum which we of Earth orbiting the Sun as it orbits around the nucleus of the Milky Way, which in turn wanders somewhere to the south of the visible Universe, it this clock also will not order the correct rate of the passage of time, which I called a real time or stationary. And the reader will be right.

The use of the light clock will be equally as the existence of gamma square – unexpected.

With the help of such a clock placed in a vacuum, we can determine our direction, in the sense of US hiking in the universe. Just in relation to a number of distant pulsars, or galaxies, which can be treated as cosmic lighthouses, we can find the direction in which our clock will walk slowest. This will mean that in this direction it moves. Based on the indications of our clock, we can also determine its speed in absolute intergalactic vacuum.

Speed is defined in relation to the Universal Reference System (URS), which is the visible Universe. For this purpose we use the clock longitudinal. Knowing the gamma value defined as the ratio of the walk paces of longitudinal clock to a transverse one, or classical Lorentz gamma, we can determine its speed of movement in relation to the fixed, three-dimensional space, characterized by that in it every motion of material bodies takes place and the light propagates with the constant speed c. Space shall be defined as a Universal Reference System.

What my "discovery" may have consequences for the theory of relativity?

So far we did not include the possibility of other than a specific by Lorentz, the rate of slowing down of clock pace. The rate defined by a specific coefficient gamma. While this rate is misidentified with the rate of the passage of time.

Meanwhile, the clock in the same inertial system, which my URS is transported with the same speed of v, but oriented parallel to the direction of travel, will slow down significantly more!

Physicists faithful to demands and theses of special theory relativity, following its author argue that the clocks always walk in the same pace only time undergoes dilation, which is evident absurdity.

We assume for the moment that this is true.

My discovery created a problem, which dilation will be now applied in SR? The transverse or longitudinal. Transverse, used since the times of the Lorentz to the present, or longitudinal, which in my humble opinion, should be used in all systems where previously erroneously applied transverse dilation.

It will be an inexhaustible source of new experiences and new industrial themes for academic discussion. In this new absurdities connected with the theory of relativity.

How will behave, which is what will notice an imaginary observer, who with his frame of reference, by the great telescopes, will observe the walking speed of two clocks in the rocket, one of which will be positioned transversely to the direction of flight, and the second longitudinally? It is found that, however, this “time dilation” is a real phenomenon, possible to observe for observers by going along with the clocks in their frame reference. Thus, relativistic jump from one system to another to see it – it is not necessary at all.

Has time dilation, as according to Mr. Einstein – light a dual character?
And how will grow older this cult paradox twin since the aging process will depend on this, which clock will be observed? And if by chance it will not age faster in the flight direction of a significantly more slowly in the direction transverse to the direction of flight of the rocket?

And what about the process of the relativistic contraction, along with the rocket course? In a direction transverse to the direction of flight – to the left and owing to turn – more?

Perhaps for the faithful believer SR my calculations will prove illegal in the sense of compliance with the postulate of constancy of the velocity of light and the relativity of motion. In the derivation of formula for the walking pace of longitudinal clock model of Lorentz and basing on the principles of classical physics, I relied on the constancy of the velocity of light in vacuum and on speed of clock motion also in a vacuum and not in relation to some undefined observer or also another reference system to which it is necessary to jump to the “time dilation” see.

And that’s why I came out with “time dilation of dilation”.

What should be understood that the light clock transported lengthwise in relation to the fixed clock, slows down his pace according to the gamma function to the second power.

Will not it be outright beating source of new absurdities affectionately called paradoxes of this absurd “theory”?

Because so far by any applicable rules in theory, twin will be shortened only in the direction of travel. And here comes that he will become thinner also in the transverse direction.

For small speed difference will be negligibly small but for examples of v = 0.999 c, already enormous. Pilot becomes cross thinner 22 times but will reduce his thickness the 500 times. And the speed v = 0.9999 c is it just a sheet of thick row 1/5000 thickness astronaut at the waist, when a rocket was going to start. In the same proportion the dimensions of the rocket will decrease.

With flight speed equal to c, rocket would have been annihilated?

Acknowledgements

Translation into English and adjustment, PhD Janusz Maczka, Poland.

References

Einstein, A. (1905). Zur elektrodynamik bewegter körper. *Annalen der physik*, *322*(10), 891-921.

Lorentz ether theory. (2017). In *Wikipedia, the free encyclopedia*. Retrieved from https://en.wikipedia.org/wiki/Lorentz_ether_theory

Lorentz, H. A. (1904). Electromagnetic phenomena in a system moving with any velocity smaller than that of light. *Proceedings of the Royal Netherlands Academy of Arts and Sciences, 6*, 809–831

Maxwell's equations. (2017). In *Wikipedia, the free encyclopedia*. Retrieved from https://en.wikipedia.org/wiki/Maxwell%27s_equations

Michelson, A. A. (1881). The relative motion of the Earth and of the luminiferous ether. *American Journal of Science*, (128), 120-129. https://doi.org/10.2475/ajs.s3-22.128.120

Michelson, A. A., & Morley, E. W. (1887). On the Relative Motion of the Earth and the Luminiferous Ether. *American Journal of Science, 34*, 333–345. https://doi.org/10.2475/ajs.s3-34.203.333

Miller, D. C. (1925). Ether-drift experiments at Mount Wilson. *Proceedings of the National Academy of Sciences*, *11*(6), 306-314.

Miller, D. C. (1933). The ether-drift experiment and the determination of the absolute motion of the earth. *Reviews of modern physics*, *5*(3), 203. Retrieved from http://www.orgonelab.org/EtherDrift/MillerRMP1933.pdf

Oostra, B. (2012). Measurement of the Earth's rotational speed via Doppler shift of solar absorption lines. *American Journal of Physics*, *80*(5), 363-366.

Sagnac, G. (1913). L'éther lumineux démontré par l'effet du vent relatif d'éther dans un interféromètre en rotation uniforme. *CR Acad. Sci.*, *157*, 708-710.

Voigt, W. (1887). Ueber das Doppler'sche Princip. *Göttinger Nachrichten,* (7), 41–51 Reprinted with additional comments by *Voigt in Physikalische Zeitschrift, XVI*, 381–386 (1915).

Wielka encyklopedia powszechna PWN. (2017). In *Wikipedia, the free encyclopedia*. Retrieved from https://pl.wikipedia.org/wiki/Wielka_encyklopedia_powszechna_PWN

Wydawnictwo Naukowe PWN. (2017). In *Wikipedia, the free encyclopedia*. Retrieved from https://pl.wikipedia.org/wiki/Wydawnictwo_Naukowe_PWN

Applied Physics Research; Vol. 9, No. 6; 2017
ISSN 1916-9639 E-ISSN 1916-9647
Published by Canadian Center of Science and Education

The Pan-STARRS1 Static Sky: A Classical Physics Goldmine for Cosmology, Astrophysics and Atomic Physics

Ogaba Philip Obande[1]

[1] Department of Chemistry, Ahmadu Bello University, Zaria, Nigeria (Retired)

Correspondence: Ogaba Philip Obande, Department of Chemistry, Ahmadu Bello University, Zaria, Nigeria. E-mail: gababands@gmail.com

Received: October 6, 2017 Accepted: October 25, 2017 Online Published: November 30, 2017

doi:10.5539/apr.v9n6p75 URL: https://doi.org/10.5539/apr.v9n6p75

Abstract

Image of the entire sky, the "Static Sky" recently released to the public by scientists at the Pan-STARRS1 telescope in Hawaii is analyzed. It depicts, for the very first time, nature's intrinsic wave-particle duality; the horizontal fine-grained darker envelope is nature's waveform, i.e., the imponderable bosonic cosmic vacuum field, while the brighter coarser-grained vertical envelope belongs to aggregate radiation of visible and invisible particulate matter (fermionic) fields. Earlier investigations were cited to inform that: i) corresponding bosonic field envelope encloses every particulate matter exactly as shown in the Static Sky image; ii) reprocessing the image into a brighter shade reveals the vertical envelope to comprise three bands with diminishing brightness from the center attributed to three ref. frames or universes with common chemical periodicity in line with previous reports on the subject; iii) the visible universe is bifurcated, the effect gives rise to its proximate linear atomic mass growth rate as against logarithmic growth rates in the invisible universes; iv) the two main observational evidences supporting the Big Bang model are faulted on fundamental theoretical grounds which show that: a) cosmological redshift phenomena arise from axial not radial motion, the effect is created by the vacuum field parametric self-interaction ρ_w/σ_w = 8.5114 x 10^{-19} (m rad/s)$^{-2}$ whose dimensional analysis yields the superluminal angular velocity v_w = 4.709 x 10^8 m/s; b) the cosmic microwave background CMB radiation is classical zero-point radiation whose temperature easily evaluates from summation of bosonic transverse fields' energies $E_w/J = h\vartheta_w$ of the chemical elements, $T_{vac.} = \sum_e^{Am} E_w/k$ = 3.675 x 10^{-23}J/1.381 x 10^{-23} J/K = 1. 662 K; v) resolution of the vertical envelope into three bands of diminishing brightness indicates that material composition of the two invisible universes, i.e., "dark matter" is accessible with the techiques employed by the Pan-STARRS' scientists.

Keywords: big bang model, classical atomic physics, cosmic microwave background, metric space expansion, pan-starrs static sky

1. Introduction

Scientists at the Pan-STARRS telescope in Hawaii released to the public a unique image of the visible universe which they call "Static Sky", credited to Danny Farro Science Consortium and Max Planck Institute for Extraterrestrial Physics; New Atlas published the image in 2016. In our opinion the "Static Sky" has the potential to resolve *all*, pending and yet to be contemplated, questions in physics. Here, we try to explain what we think gives rise to the image and why we have the highest expectation of its potential for unprecedented revolution in classical quantum physics, astrophysics and cosmology.

2. Method

We will use methods which we have reported severally to support our explanation of the image and suggest ways to harness its immensely rich potentials; see Obande (2013, 2015a, 2015b, 2015c, 2016a) for detailed descriptions of the methods.

3. Results

We illustrate some of our positions with a set of five figures: Figure 1 is, of course, a reproduction of the "Static Sky" as made public by Newatlas.com (2016), Figure 2 is an illustration of mutual orthogonality of frames of reference or universes that work in harmony to create in us a profound experience of reality, Figure 3 illustrates the bifurcation of our visible universe without which our experience of reality would be entirely different and Figs. 4 and 5 illustrate the causality of radioactivity, a common feature of every particulate matter.

4. Discussion

If you try to simulate observational relative atomic mass m_r values using the classical mass formula $m = h\vartheta/c^2$ you get values that do not seem to relate to reality; they start with 7.3725×10^{-51} kg/atom for $\vartheta = 1.0$ Hz and rise to $m = 4.7432 \times 10^{-38}$ kg/atom for $\vartheta = 6.4425 \times 10^{9}$ Hz for americium which marks the end of the natural periodicity; these values contrast with approximate linear growth rate and two orders of magnitude difference between empirical relative atomic mass values of H and Am. Thus, use of the classical mass formula yields quantum mass values of the atomic waveform, they follow a logarithmic function with about 12 orders of magnitude difference between H and Am; we attribute these ultra low rest mass values, of course, to "absolute atomic mass" m_{abs} or simply m_w. If you now divide ϑ or m values of the elements by H atom's value you get theoretical m_r values, they correspond to empirical values only up to He from which you observe increasing deviation from empirical values with an increase in atomic number. In order to realize empirical values, you may have to employ a semi-empirical model that produces a linear function from appropriate combinations of two exponential functions. It will yield a final result that makes a compelling case for existence of three ref. frames or universes which work in harmony to produce a common experience of reality; they include: i) an Absolute universe or ref. frame U^*_w that comprises only elemental waveforms; ii) a particulate matter component of the Absolute universe or ref. frame U^*_p; iii) our visible condensed matter universe U^o_p, and iv) an invisible particulate matter analogue of our visible universe U'_p. Notably, all four universes identify with a common periodicity of the chemical elements; in other words, each chemical element exists in four forms comprising one microcosmic waveform and three particulate matter forms; physics identifies the condensed matter forms with "particle generations" Francis (2015).

In order to unambiguously identify the first element of the chemical periodicity, call it E1, you will adopt the convention that reduces absolute atomic mass values to unit H atom for which we have $m_{abs(H)} = 1.5078 \times 10^{-47}$ kg/u and $\vartheta_{abs(H)} = 2048$ Hz. The values give $m_{r(E1)} = 1 \times 10^{-3}/2048 = 4.8828125 \times 10^{-7} = 7.3725 \times 10^{-51}/1.5078 \times 10^{-44} = 4.8896 \times 10^{-7}$ kg/u. From closeness of the results to electron's empirical relative atomic mass, $m_{r(e)} = 5.4858 \times 10^{-7}$ kg/u, you cannot but conclude that E1= e, the electron. In other words, you find amazingly that there exists a "natural" periodicity of the chemical elements that accords e full-fledged elemental status and identifies it with premier position. The line of investigation leads you to discover 27 unknown elements that seamlessly add to the conventional periodicity - that is a summary of results of our investigations, Obande (2013, 2015a, 2016a); it leads to the unavoidable conclusion that: i) reality comprises a universe made up entirely of waveforms and ii) two invisible particulate matter universes work in harmony to produce our visible matter universe. We now present the "Static Sky".

4.1 The Static Sky is the Cosmic Large Scale

Newatlas.com's (2016) publication of the "Static Sky" is reproduced in Figure 1, it comprises two distinct spacetime envelopes, a vertical granular brighter envelope is encased in a finer darker horizontal envelope. We submit that the image presents, for the very first time, a visual evidence of nature's intrinsic wave-particle duality; we review the details.

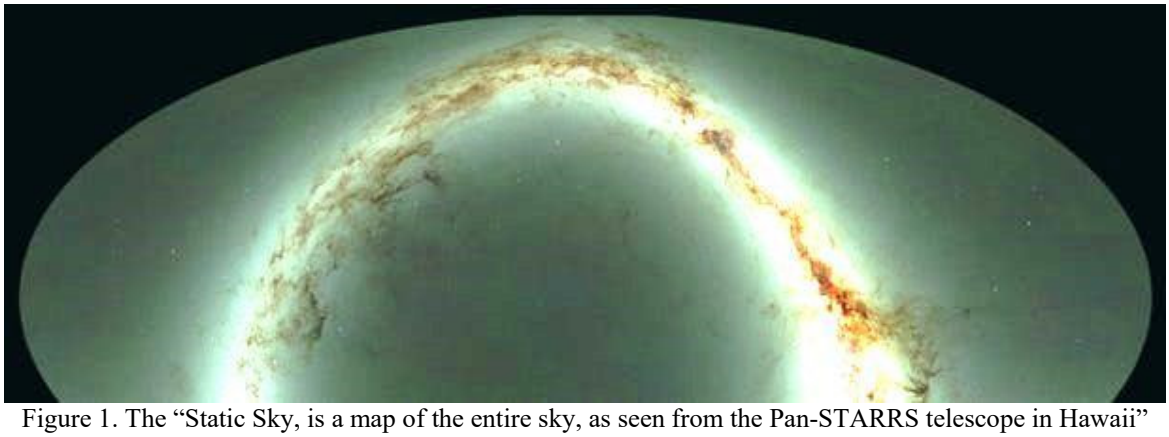

Figure 1. The "Static Sky, is a map of the entire sky, as seen from the Pan-STARRS telescope in Hawaii" (*Credit: Danny Farro Science Consortium and Max Planck Institute for Extraterrestrial Physics*).Posted by Newatlas.com (Color online)

4.1.1 The Cosmic Bosonic Vacuum Field

The horizontal envelope is matter's waveform, it is the cosmic bosonic vacuum field which we call "Absolute Universe U^*_w", it accounts for many observational effects including: Newtonian gravitation, the strong nuclear force (SNF), electron magnetic moment, electric permittivity constant, magnetic permeability constant, electric polarizability, nuclear magnetic moment, radioactivity and metric expansion of space, Obande (2017a). The classical mass formula holds strictly *only* in this field where we have $\phi_w = h\vartheta_w/m_w c^2 = 1.0$, Obande (2015a).

4.1.2 The Fermionic Field (Particulate matter) Universes

The vertical envelope comprises three condensed matter fermionic fields, each is a universe including the invisible Component of the Absolute U^*_p, our Visible U^o_p and our invisible Analogue U'_p; they are co-existent, exchange mass-energy m-e matrices and made up of clusters, nebulae, galaxies, stars, satellites of the stars, et cetera. These material universes are collectively responsible for such effects as gravitational acceleration, magnetic flux density, the fine structure constant, electron Compton wavelength and nuclear quadrupole moment. The classical mass formula fails to apply strictly here as we find $\phi_p = h_p^x/h\vartheta_p^x c^{o2} = k$ where x indicates the universe and all three identify with the common fermion transverse field c^o = 3.71535229 x 10^{-14} m/s; the coefficient k is element and universe specific, its value 1.0172 obtains for most elements in U^*_w, U^*_p and U^o_p but fluctuates significantly in U'_p where it records the figures 10 to 102, the latter is recorded by Fe, Obande (2015a), it would account for Fe's exceptional binding energy.

4.1.3 Relative Brightness of the two Envelopes

Relative brightness of the two envelopes reflects atomic energy disparity between the boson (b) and fermion (f) fields, the energy ratio E_f/E_b varies from 1.0 to 102/atom as explained above. Avogadro number, i.e., 6.23 x 10^{43}, Obande (2015a), multiples of this difference amounts to an immense aggregate molar energy contribution from zillions of tons of material objects in the three particulate matter universes to the brightness of the fermionic envelope.

An attempt to brighten the downloaded New Atlas' image produced a surprise; the vertical envelope resolves into three bands of shades if the image is printed in black and white with reduced contrast (ink-deficient cartridge); we attribute these bands to the three particle generations, with diminishing order of brightness from the center we have $U^o_p \gg U'_p > U^*_p$. It is the first evidence that the normally invisible U'_p and U^*_p do indeed give off measurable radiation if the procedure adopted by the Pan-STARRS scientists is followed, it points to an exciting possibility for "dark matter" research.

4.1.4 Orthogonality of the Fermion Field Universes and Invisibility of U^*_p and U'_p

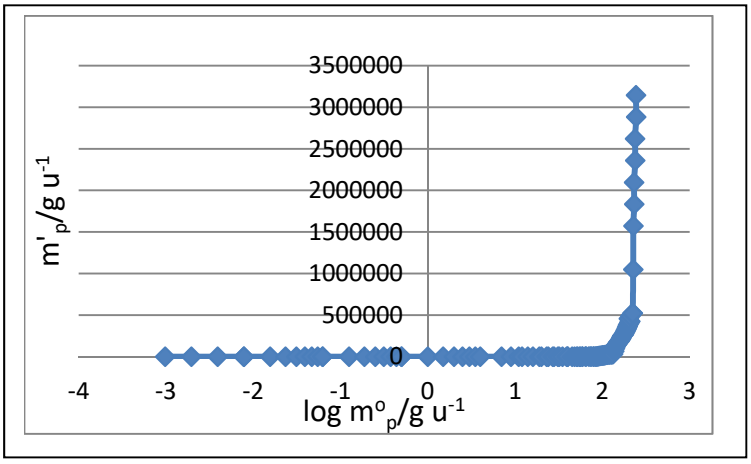

Figure 2. Plot of m'_p vs. log m^o_p

Figure 2 is a correlation of m'_p/u vs. log m^o_p/u, use of logarithmic scale for m^o_p merely facilitates a smooth rather than staggered curve. The figure reveals that m-e matrices of the two universes are orthogonal, and indeed all three particle-generation universes are mutually orthogonal; the subject is a bit involved, it traces to radioactivity and includes topics that fall outside the scope of this report. We see no immediate reason to ascribe some special qualities (such as life forms and intelligent beings) to our visible universe U^o_p which nature would contrive to deny our invisible co-tenants U^*_p or U'_p or, indeed, U^*_w, we expect, therefore, that same chemical reactions that produce visible matter and life forms in U^o_p would do likewise in the invisible. Invisibility has earned them the appropriate

tag "dark matter/dark energy", however, their contributions to our observational physical parameters, strongly speak to their physical existence, Obande (2017a). We celebrate Figure 1 as it resolves so many pending issues in contemporary atomic physics. U^*_w is a waveform, characteristically invisible, however, the question of invisibility of U^*_p and U'_p remains pressing, we note as follows: i) existence of two or more material universes that co-exist with and exchange spacetime matrices with our universe is entirely new to physics, at the moment there is no theoretical framework for information (light) communication across mutually orthogonal ref. frames; ii) as evident in Figure 2, there is continuous matrix exchange between the three material universes, in the visible universe the exchange gives rise to high energy γ and α radiations, Obande (2016b), particularly those associated with black holes and the cosmic large scale, Cartlidge (2011), Cowan (2011), Dylan (2014), Borghino (2015).

4.2 Bifurcation of the Visible Universe

Figure 3 is a plot of ϑ^x_p vs. Z_n for U^*_p, U^o_p and U'_p, where Z_n is the element's atomic number in nature's chemical periodicity, Obande (2016a). Notice the bulge in ϑ'_p values at the 5th chemical period/space octave, the interval Z_n = 30 to 35, and observe that beyond this interval values of ϑ^o_p degrade progressively relative to corresponding ϑ^*_p and ϑ'_p values down to the end of the periodicity, it presents a bifurcated visible universe. The feature makes a lengthy subject which again cannot be taken here; briefly, i) it is responsible for proximate linear atomic mass growth rate in U^o_p relative to logarithmic growth rates in U^*_w, U^*_p and U'_p; ii) it marks the periodic space wherein our invisible analogue U'_p exchanges spacetime matrices with the visible U^o_p; iii) it traces to the classical black hole; a detailed report on the subject is in progress.

The quantitative implication of the bifurcation is remarkable. It divides the visible universe into three distinct blocks of chemical elements: i) the linear mass progression from electron e to Na which includes 22 inaccessible elements existing between e and H conventionally called "elementary particles", Obande (2016a); ii) the inflexion block from Li to Mg, it gives rise to the bulge in Figure 3 and associates with the classical black hole, and iii) the pseudo-logarithmic rest mass growth rate from Mg to the end of the periodicity. Our investigation reveals that the interval Z_n = 30 - 35 marks spacetime quanta that demarcate material and spatial periodicities, it is nature's device for m–e matrix exchange between U^o_p and U'_p, relative atomic mass m_r values in our universe owe to this device, i.e., m_r (m^o_p) = $m^*_p \pm m'_p$; before the device, the sum applies and after it the difference applies. An attempt to rid the simulation of reference to empirical m_r values produced the expression to $m^o_p = \vartheta'_p(1 \pm \psi)/2048$, where the ratiot $\psi = \vartheta'_p/\vartheta^*_p$ and $\vartheta^*_{w(H)} = \vartheta^*_{p(H)} = \vartheta'_{p(H)} = 2048$; it shows that U^o_p results from non-linear wave dynamics of U^*_p and U'_p.

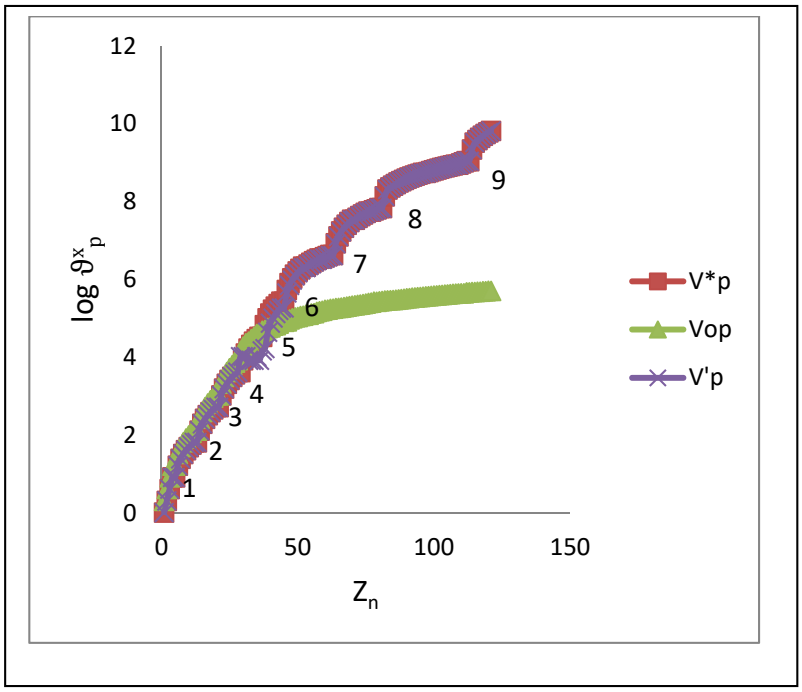

Figure 3. Plot of log ϑ^x_p vs. Z_n (Color online)

4.3 Radioactivity, Stellar Explosion and Metric Space Expansion

4.3.1 Radioactivity and Stellar Explosion/Supernova

Conventional notion attributes radioactivity to instability of the atomic nucleus with nuclidic content as culprit. According to this notion, the atom achieves stability through energy loss in the form of α-, β- and neutrino decays, γ-ray emission and/or e-capture. Radioactivity is believed to be a random ("stochastic") process, impossible to predict regardless of how long the atom existed. Three models are adjudged successful to partially or fully account for the effect: the collective model; independent particle model; and the combined model, acclaimed most successful of the three, Halliday et al. (2002). Beyond numerical nuclidic proton-neutron balance, particularly the concept of magic numbers, conventional notion sees no further details on the specific causality of nuclear instability.

Classical Newtonian physics, however, traces radioactivity to convergence of absolute values of tensile properties of the waveform e-m harmonic oscillator, it reveals that spontaneous radioactivity occurs once the oscillator's angular speed attains a critical value, Obande (2015b). A recent investigation of the familiar physical constant $|e-| = 1.6022 \times 10^{-19}$ yields the relationship,

$$\rho_w \vartheta_w^4 = 3m_w/\omega_w c^3 = 1.0691\ x\ 10^{-19} N\ m/(m/s)^3 rrd^{-1}s^{-1} \quad (1)$$

Eq. (1) describes "an effect in which the torque field imposes an accelerated (bulk) compression which couples with angular speed to impact an aggressive hydrostatic pressure on the bosonic envelope", Obande (2017a). It is further posited that: i) on atomic scale, precisely at At ($m_r = 0.210$ kg/u, $\omega^o_p = 2 \times 10^{10}$ rad s^{-1}), the effect initiates spontaneous radioactivity, and ii) on stellar and galactic scales, it is responsible for stellar explosion/supernova at a yet to be investigated ω value. Thus, classical analysis reveals that variation of vacuum radiation density with oscillation frequency gives rise to spontaneous radioactivity at a critical angular speed value; notably, the same parametric combination initiates radioactivity on atomic scale and stellar explosion on cosmological scale. In other words, stellar explosion/supernova is cosmological equivalent of spontaneous radioactivity, it adds an important cosmological dimension to universal discrete scale relativity.

Figs. 4 and 5 illustrate causality of spontaneous radioactivity with plots of τ^*_w vs. ω^*_w/r^*_w and τ^*_w vs. Z_n respectively. Observe as follows: i) radioactivity is caused exclusively by changes in tensile properties of the boson field that encases fermionic matter exactly as shown in Figure 1; in other words, the wave component of the atom exercises significant control over the particulate matter component likewise, the cosmic vacuum field exercises similar control over its material cosmological content; ii) Figure 4 pinpoints spontaneous radioactivity at At, $\tau^*_w = 2.14$, i.e., 214%; iii) Figure 5 facilitates visualization of the stepwise process of nuclear instability that leads to radioactivity. Discernible evidence of instability commences at Ru, $Z_n = 70$, where a change becomes noticeable in the τ^*_w/Z_n gradient, the change progresses gradually up to Xe, $Z_n = 80$ where a sudden jump occurs signifying considerable instability albeit insufficient to initiate spontaneity which eventually occurs at At, $Z_n = 111$, Obande (2015c). The quotient $\tau/(\omega/r)$ denotes electrostatics effect, it manifests atomic mass, Obande (2016a), it would account for m-e packet ejection at spontaneity as reflected in the staggered mass distribution. Given that 1.0 mole contains 6.23×10^{43} (*not* 6.02×10^{23}) particles, even if only a few m-e packets are ejected per second, it would account for values of half lives of most natural radioactive decays.

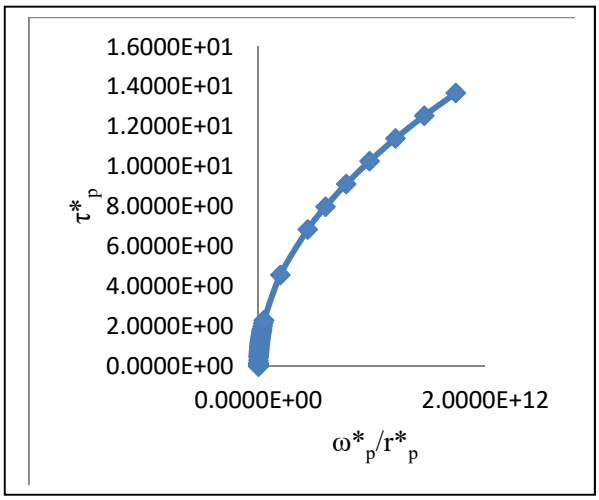

Figure 4. Plot of τ^*_w vs. ω^*_w/r^*_w

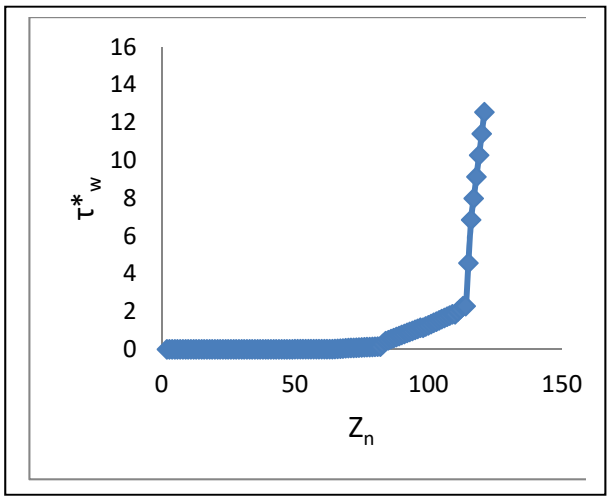

Figure 5. Plot of τ^*_w vs. Z_n

4.3.2 Metric Expansion of Space

Few issues command wider physical research attention than the nature and causality of space expansion yet, several questions remain pressing. Is space actually expanding or is it a classical de Sitter (1917) static universe? If expanding, is it Hubble's (1929) radial motion as formalized by Hoyle (1948), or is it angular motion as some insist?, Peebles & Ratra (2003), Longo (2011), Raghuprasad (2013), Jakubowski (2016).

In a tabulation titled "Timeline of Cosmology" Wikipedia provides a succinct but quite informative highlight on development of cosmological theories from Hindu Rigveda (2000BC) to the reigning paradigm. Notably, the table provides snapshots of the cosmologies of Einstein, de Sitter, Friedmann, Lemaitre (Big Bang Model, BBM), Milne & McCrea, Robertson & Walker, Bondi, Klein, Guth, Steinhardt & Turok, and Baum & Frampton. It highlights an epic marked with key developments, notably, Friedmann's (1922) field equation indicating expanding space; Hubble's (1929) observational evidence, and Lemaitre's (1931) construction of the BBM. From Einstein's (1920) original static finite universe, modern Standard Cosmological Model SCM uses the Hubble Constant to construct first, a linearly expanding space, Hoyle (1948), then an accelerating universe, Reiss (1998), Floerchinger (2015) and now, recent observational evidence would seem to favor a return to a linear but *incredibly fast* expansion, Nielsen et al. (2016), Reiss et al. (2016), Castelvecchi (2016).

Notably, majority positions on space expansion derive from redshift measurement. In line with sound wave Doppler shift, it would seem quite natural to interpret Hubble's (1929) results in terms of radial motion; the same notion had earlier informed Slipher's (1913) interpretation of radial velocity of Andromeda Nebula. It is, therefore, a matter-of-course for same notion to inform Lemaitre's (1931) BBM and Hoyle's (1948) expanding universe model. The question of whether or not cosmological redshift is due to radial or angular motion remains open to date. One thing is certain, most cosmological structures literally spin on their axis, however, the effect is not quantitatively explicit at the quantum level.

Quantum mechanics QM notion of spin replaces Uhlenbeck and Goudsmit's (1926) explicit definition with a non-specific notion that differs significantly from literal physical rotation; for instance, Wikipedia says, "In 1925, Ralph Kronig, George Uhlenbeck and Samuel Goudsmit at Leiden University suggested an *erroneous* physical interpretation of particles spinning on their own axis", emphasis ours. Thus, spin in QM admits of quantized (classical) angular momentum but rejects (quantized) classical physical rotation, it makes it a bit challenging to rationalize QM's spin with observational evidence see, for instance, Moskowitz (2014) and Siegel (2017). One would have expected that by now there should be no doubt regarding universality of scale-free spin in the context of physical rotation; it comes quite naturally in analysis of the classical quantum state, Obande (2015b, 2015c, 2016a) and in observational cosmology, Rubin (2000). Indeed, existence as we know it in terms of say, gravitation, magnetism and random (thermal) motion would cease without scale-free physical rotation of matter waves, Obande (2017a). We see no peculiar characteristics capable of precluding the atom or "sub-atomic" particle from physical rotation. The situation is traceable to statistical mechanics, the subject contributed much to early development of QM, e.g., Pauli (1940), if the development had been informed by the atomic quantum e-m harmonic oscillator, physics might have taken an entirely different course, likely a lot more observational, conceptual and cognitive than the reigning paradigm.

Classical analysis reveals that space is indeed not accelerating but "expanding" at a superluminal velocity; the parametric interaction causality is spatial variation of bosonic flux density with stress field, interestingly, it identifies also with the ubiquitous $|e^-| = 1.6022 \times 10^{-19}$, Obande (2017a); a log-log plot of ρ_w vs.σ_w yields,

$$\rho_w/\sigma_w = 8.5114\ 10^{-19}\ (m\ rad/s)^{-2} \quad (2)$$

Dimensional analysis gives $\rho_w/\sigma_w = 3/4(r_w\omega_w)^2 = 3.3819\ \ 10^{-18}(m/s)^{-2}$, i.e., $v_w = 4.709 \times 10^8$ m/s; in plain words, the vacuum field is moving *tangentially* at superluminal velocity 1.57c m/s. We hasten to note here that the denominator 4 was omitted from the coefficient 3/4 in our earlier report, Obande (2017a), it gave the wrong value $v_w = \pi c$, instead of ~ $0.5\pi c$; the final conclusion that vacuum space is moving tangentially at superluminal velocity is not affected but the correct value of the velocity field is about half of the reported value, the error is regretted. Given the vacuum density $\rho_w = 2.609 \times 10^{-36}$ kg/m^3, Obande (2016b) and stress field $\sigma_w = 3.086 \times 10^{-18}$ Pa, Obande (2015b), theory suggests that the rate of metric space expansion is assessable from tensile properties of the vacuum.

Notably, the result ($v = r\omega$) shows clearly that space *is not* expanding radially, the effect is tangential velocity; more significantly, spatial expansion is not caused by negative gravitation, cosmological constant or "dark energy", it results from an ingenious field engineering whereby the field density/stress quotient produces a constant superluminal tangential velocity field, i.e., isotropic, isostasic, bolometric vacuum space subjected to a constant hydrostatic shear stress complies through a constant superluminal angular speed.

4.4 The Static Sky and Universal Conformal Invariance

For the very first time in history, mankind is able to see the primitive structure of reality, by all standards it is the greatest empirical feat since Galileo. Figure 1 is an image of the primitive structure of every material object including the isolated atom, "sub-atomic" particle, molecule, cell, organism, animate and inanimate forms and, of course, the cosmos. The literature on discrete scale relativity such as Oldershaw (2007, 2014), Fedosin (2017) and Wikiversity, might seem to lack direct bearing to Figure 1 and that informs our goal in this paper – to show that the "Static Sky" makes the most powerful addition to existing evidences that conformal invariance is a fundamental attribute of nature. From the atom to the cosmos, matter intrinsically comprises wave and particulate forms orthogonally positioned as shown in Figure 1; it informs observationals like relative orthogonality of major axes of the developing chick and the egg shell or the mammalian embryo and the womb, its presence at the level of the cell has been identified with cosmological structures, Oldershaw (2014), Berry et al. (2016). Without prior knowledge, our recent classical analysis produced evidence that took us by surprise and led to a literature search that called our attention to the subject, Obande (2017b). Right from the onset, our investigations have consistently compelled definition of reality with a clear distinction between the atomic wave and particulate forms that transform to the cosmic large scale comprising the vacuum (boson) field and condensed matter (fermion) field, it informs our sheer excitement with the visible evidence.

So, how does evidence for wave-particle nature of reality answer *all* existing and conceivable questions in physics? There is no short answer to that question; the implications are enormous and we must expect that every atomic physicist is well aware of the fact. Simply, it calls for a major review of the conventional fundamental approach. Hitherto, physics has focused on only one half of reality, now we have observational evidence that presents the complete picture; it merges cosmology, astrophysics and atomic physics into a single profound physical discipline that identifies with same classical Newtonian physics which differentiates only in values of extensive properties. It suddenly promotes the telescope a most invaluable physical research tool on equal, if not superior, footing with the accelerator for investigating internal structure and properties of the isolated atom.

This is a summary of our take on Figure 1: discrete scale relativity informs that the cluster and galactic dimensional hierarchicals replicate chemical periodicity in which the galaxy is equivalent to the chemical element. The galaxy in turn comprises a periodicity in which the star is equivalent to the chemical element and the star comprises a periodicity in which the satellite (planet) is equivalent to the element; thus, an investigation of cosmological dynamics corresponds to an investigation of atomic dynamics, the two extreme scales identify with same formalism but differ only in extensive properties.

4.5 Size of the Cosmos and the Big Bang Model

4.5.1 Size of the Universe

Until some theoretician (often mathematician) comes up with (usually compelling) quantitative accounts of why what we see might not be what we think, thanks to Figure 1, we now have a visible evidence to address whether or not the observable cosmos is (visually not mathematically) flat or curved, open or closed, finite or infinite. We must await the outcome of detailed evaluation of the image's spatial dimensions to get an idea of its total size and, possibly, dimensions of the constituent envelopes, i.e., the universes U^*_p, U^o_p and U'_p. However, the question of its boundary, and by implication exact shape, might not be as simple as the image would suggest; for certain, the boundary would be an impenetrable invisible pitch-black zero-Kelvin vacuum, the shape of the entire system would depend on its symmetry group. We have argued that every natural form, be it electron or the galaxy, belongs to one of only four symmetry groups, Obande (2017b); it invariably starts off as symmetry group SG 1, ideally a perfect sphere, or cycle in 2D, matures as SG 4, ideally a perfect cube or sphere and evaporates into space through the tortuous gradual processes of highly distorted SG 3, SG 2 and finally, again SG 1, see the image posted by Sparknotes (2015) of an evaporating cosmic object in highly distorted, indeed fragmented, SG 1. If the two elliptical envelopes of Figure 1 were re-constructed and the vertices joined, we would get a rectangle which ideally would be a square for SG 4 in 2D, a deviation from the square would indicate corresponding deviation from full maturity and gradual slide into distortion. Given the previous and present analyses, we take the position that Figure 1 is the *current* image of our observable cosmos, it would seem to suggest a healthy state of maturity for our cosmos; but cosmology attests to the fact that the state of health of the cosmic envelope does not necessarily translate to the state of health of constituent galaxies; it should be possible to assess the state of health of a galaxy, and possibly a stellar system, when the subject is sufficiently developed. Majority literature estimates put the diameter of the visible cosmos at 90 (±2) billion light years, Carlstrom (2015), Azher (2016) and Redd (2017); however, as observed by NASA (2015, 2017), at the moment no one knows for certain the size of the whole universe.

4.5.2 The Big Bang Model

Two key observational evidences claim support for the BBM: the Hubble Constant HC and the Cosmic Microwave Background CMB. We find above that HC refers to angular not radial motion, space is not expanding into newly created matrices, it identifies with varied scales of angular motion; we examine the case for the CMB.

Contrary to literature, Hu et al. (1997), The Task Force Report (2005), Bennet (2006), Bennet et al. (2013), Peplow (2013), the CMB is not an "after glow" of BB's original radiation, *it is* the vacuum field, i.e., classical zero-point radiation. Planck energy $h\vartheta$ of the chemical elements' waveforms vary from electron's $E_{e(w)} = 6.6261 \times 10^{-34}$ J/atom to americium's $E_{Am(w)} = 4.2688 \times 10^{-24}$ J/atom, Obande (2015a). A vacuum property obtains not as an average but summation of each element E's value, Obande (2016c) thus, we have $\sum E_{w(E)} = 3.6749 \times 10^{-23}$ J; it gives (delete space) $T = \sum E_w/k = 3.6749 \times 10^{-23}/1.381 \times 10^{-23} = 2.662$ K, a value well in line with empirical 2.725 K, Big Bang (2017). We must call attention to wrong attribution of the CMB to de Broglie radiation in all preceding reports, the error arose from avoidable inadequate attention to details whenever the subject is not the principal object of investigation, it is regretted. The present analysis immediately accounts for anisotropy. The CMB arises from only bosonic envelopes that enclose fermionic packets as shown in Figure 1, it demarcates concentrations of matter, with zero Kelvin voids in between envelopes as shown in the WAMP map, Bennet (2013); compare, for instance, the "… WAMP image…" and the "Panoramic view of the entire infra-red sky…" in (Big Bang 2017), juxtaposition of transparencies of the two images would make interesting comparison.

Some respectable opinions have persistently refuted existence of a link between the CMB and the BB, Assis and Neves (1995), Arp (2005), Mersini-Houghton (2014); Figure 1 is, perhaps, the best large-scale visual evidence yet revealing a profoundly ordered cosmic envelope. Now that we have a visual evidence, some might want to work out a quantitative procedure that permits an uncontrolled cataclysmic cosmic explosion to eventually cool to the ordered system of Figure 1 but, certainly it would be taking an expensive joke much too far to attempt an account of the separation and mutual orthogonal orientation of the boson and fermion fields. Already, an attempt exists that explains away discrete scale relativity in the context of a "… Background of the Cosmological Collider", Chen et al. (2017); in other words, physics is rapidly losing its science to a veritable mathematical gymnastics.

5. Summary and Conclusion

i. Image of the entire sky, the "Static Sky" recently released to the public by scientists at the Pan-STARRS1 telescope in Hawaii is analysed. It depicts, for the very first time, nature's intrinsic wave-particle duality.

ii. The horizontal fine-grained darker envelope is nature's waveform, i.e., the imponderable bosonic cosmic vacuum field, while the brighter coarser-grained vertical envelope belongs to composite radiation of visible and invisible particulate matter fields. Relative brightness of the two envelopes reflects quantifiable energy difference between the atomic wave and particulate forms; mass-energy m-e equivalence holds strictly only in the vacuum field where the wave/particle energy coefficient is unity, i.e., $\phi_w = h\vartheta/mc^2 = 1.0$, the same coefficient is greater than unity in the fermionic matter field, i.e., $\phi_p = h\vartheta^x{}_p/m^x{}_p c^{o2} = k$, where k varies in value from 1.0172 to 102, index x refers to the ref. frame and c^o is invariant transverse field of particulate matter radiation.

iii. Earlier investigations were cited to inform that corresponding bosonic field envelope encloses every particulate matter exactly as shown in the Static Sky image, it is exclusively responsible for observational effects such as gravitation, radioactivity, metric space expansion, vacuum permittivity, magnetic permeability and the strong nuclear force that holds matter together on all, from submicroscopic to cosmic, scales.

iv. Earlier investigations were also cited to inform that the vertical coarse-grained brighter envelope comprises three ref. frames or universes with common chemical periodicity, two invisible material universes co-exist in harmony with our visible universe, all three are mutually perpendicular. Particulate matter (fermionic) field exclusively manifests the fine structure constant, magnetic flux density, electron Compton wavelength and gravitational acceleration.

v. The visible universe is bifurcated and the effect is responsible for its proximate linear atomic mass growth rate as against logarithmic growth rates in the invisible universes; the bifurcation occurs within a narrow atomic mass interval which marks periodic space within which the visible universe and its invisible analogue exchange m-e matrices.

vi. The two main observational evidences supporting the Big Bang model are faulted on fundamental theoretical grounds which show that: a) cosmological redshift phenomena arise from axial rather than radial motion, the effect is manifested by the vacuum field parametric self-interaction $\rho_w/\sigma_w = 8.5114 \times 10^{-19}$ (m rad/s)$^{-2}$ whose dimensional analysis yields the superluminal angular velocity $v_w = 4.709 \times 10^8$ m/s; b) the cosmic microwave background CMB radiation is classical zero-point temperature easily

evaluated from summation of bosonic transverse fields' energies $E_w = h\vartheta_w$ of the chemical elements, $T = \sum_e^{Am} E_w/k = 3.675 \times 10^{-23}$J/1.381 10^{-23} J/K = 1.662 K.

We conclude that the Pan-STARRS' "Static Sky" is indeed physics all-time goldmine whose theoretical and empirical potentials are likely inexhaustible in the foreseeable future. Given the mounting evidences for universality of discrete scale relativity DSR, the Static Sky merges atomic physics with astrophysics and cosmology in a way never before imaginable. We expect that when fully developed DSR, with the assistance of topology, would subsume all science disciples in physics.

Recommendation

In our opinion, since Galileo, there has been no greater empirical contribution to physical knowledge of reality than the "Static Sky". Without considering ourselves qualified to do so, we crave indulgence to recommend to the physical community for the highest decoration in physics, the key contributor(s), without whom realization of Figure 1 would be either impossible or of much lower definition for meaningful analysis.

References

Arp, H. (2005). Observational cosmology: from high redshift galaxies to the blue pacific. *Progress in Physics*, *3*, 3.

Assis, A. K., & Neves, M. C. (1995). History of the 2.7 K temperature prior to Penzias and Wilson. *Apeiron*, *2*(3), 79-87.

Azher, A. (2016). *What is the size of the universe in cm*? Retrieved from https://socratic.org/questions/what-is-the-size-of-the-universe-in-centimeters

Bennett, C. L. (2006). Cosmology from start to finish. *Nature*, *440*(7088), 1126-1131. http://dx.doi.org/10.1038/nature04803

Bennett, C. L., Larson, D., Weiland, J. L., Jarosik, N., Hinshaw, G., Odegard, N., ... & Komatsu, E. (2013). Nine-year Wilkinson Microwave Anisotropy Probe (WMAP) observations: final maps and results. *The Astrophysical Journal Supplement Series*, *208*(2), 20. http://arxiv.org/abs/1212.5225

Berry, D. K., Caplan, M. E., Horowitz, C. J., Huber, G., & Schneider, A. S. (2016). "Parking-garage" structures in nuclear astrophysics and cellular biophysics. *Physical Review C*, *94*(5), 055801. https://dx.doi.org10.1103PhysRevC.94.55801

Big Bang. (2017). In *Wikipedia, the free encyclopedia*. Retrieved from http://en.wikipedia.org/wiki/BigBang

Borghino, D. (2015). New model suggests dark matter is made up of electrically charged tparticles. *Gizmag magazine Sept. 27*.

Carlstrom, J. E., Crawford, T. M., & Knox, L. (2015). Particle physics and the cosmic microwave background. *Physics Today*, *68*(3), 28-34. Retrieved from

http://scitation.aip.org/content/aip/magazine/ physicstoday/article/68/3

Cartlidge, E. (2012). *Gamma rays hint at Dark Matter*. Retrieved from http://physicsworld.com/cws/article/news/2012/apr/24/gamma-rays-hint-at-dark-matter

Castelvecchi, D. (2016). Measurment of Universe's expansion rate creates cosmological puzzle. *Nature News & Comments 14th April*. Retrieved from https://www.nature.com/news/measurement-of-univesses-expansion-rate-creates-cosmological-puzzle-1.19715?WT.mc_id=SFB_NNEWS_1508_RHBox

Chen, X., Wang, Y., & Xianyu, Z. Z. (2017). Standard Model background of the cosmological collider. *Physical Review Letters*, *118*(26), 261302. https://dx.doi.org10.1103/PhysRevLett116261302

Cowan, R. (2011). Shedding light on the mystery of dark matter. *Nature News*. http://dx.doi.org/10.1038/news.2011.531

Einstein, A. (1920). Relativity: The Special and General Theory, trans. *Robert W. Lawson (New York: Crown, 1961)*, *26*. Retrieved from http://www.archive.org/details/cu392401180

Fedosin, S. (2017). *Infinite Hierarchical Nesting of Matter*. Retrieved from

https://en.wikiversity.org./wiki/Essays/ Fedosin/Infinite_hierarchical_Nesting_of_Matter

Floerchinger, S., Tetradis, N., & Wiedemann, U. A. (2015). Accelerating cosmological expansion from shear and bulk viscosity. *Physical review letters*, *114*(9), 091301. https://dx.doi.org/10.1103/PhysRevLett.091301

Francis, M. R. (2015). *The Mystery of particle generations*. Retrieved from http://www.symmetrymagazine.org/article/august2015/the-mystery-of-particle-generations

Friedman, A. A. (1922). Uber die Krummung des Raumes. *Zeitschrift fur Physik, 10*(1), 377.

Friedman, A. A. (1999). On Curvature of Space. *Gen. Rel. Grav., 31*(12), 1991

http://dx.doi.org/10.1023/A:10267 1225741

Gott III, J. R. (2005). A Map of the Universe. *Astrophys. J., 624*, 463 http://arxiv/abs/atsro-ph/0310571

Halliday, D., Resnick, R., & Walker, J. (2002). *Fundamentals of Physics*. N.Y.: John Wiley.

Hoyle, F. (1948). A New Model for the Expanding Universe. *Mont. Not. Roy. Astron. Soc., 108*, 372. Retrieved from http://adsabs.havard.edu/abs/1948MNRAS.108..372H

Hu, W., Sugiyama, N., & Silk, J. (1997). The physics of microwave background anisotropies. *Nature, 386*, 37.

Hubble, E. (1929). A relation between distance and radial velocity among extra-galactic nebulae. *Proceedings of the National Academy of Sciences*, *15*(3), 168-173. http://dx.doi.org/10.1073/pnas/15.3.168

Jakubowski, P. (2016). Consiquences of the unification in physics II, Cosmic hierarchy of the solar system. *Physics Essays, 29*(1), 129. http://dx.doi.og/0836-1319-29.1.129

Lemaitre, G. (1931). The Evolution of the Universe: Discussion. *Nature, 128*(3234), 699.

Linden, T. (2014, August). The Characterization of the Gamma-Ray Signal from the Central Milky Way: A Compelling Case for Annihilating Dark Matter. In *AAS/High Energy Astrophysics Division* (Vol. 14). http://arxiv.org/abs/astro-ph/1402.6703

Longo, M. J. (2011). Circumferential movement rather than radial. *Phys. Lett., G699*(4), 244.

Mersini-Houghton, L. (2014). *Black holes don't exist and Big Bang theory is wrong*. Retrieved from http://www.huffington.com./2014/09/29/black-holes-dont-exist-n-5885940

Moskowitz, C. (2014). *Proton Spin Mystery Gains a New Clue*. Retrieved from http://www.scientificamerican.org/article/proton-spin-mystery-mystery-gains-a...

NASA. (2015). *The Cosmic Distance Scale*. Retrieved from https://imagine.gsfc.nasa.gov/cosmic/farthest_info.html

NASA. (2017). *How big is our Universe*? Retrieved from https://www.nasa.gov/audience/foreducators/5-8/F_How_Big_is_Our_Universe.html

National Science Foundation (USA). (2005). *Report of the Task Force, Cosmic Microwave Background Research*. Retrieved from http://www.nsf.gov/mps/ast/tfcr.jsp>(2005)

New Atlas. (2016). *Static Universe*. Retrieved from http://newatlas.com//pan-starrs-largest-digital-survey-visible-universe

Nielsen, J. T., Guffanti, A., & Sakar, S. (2016). Marginal evidence for cosmic acceleration from Type 1A supernovae. *Sci. Reports, 6*, 35596. https://dx.doi.org/10.1038/sreo35596

Obande, O. P. (2013). Notes on Russellian cosmogony – Part I: Absolute Atomic Mass. *Int. J. Eng. Sci., 2*(4), 68. Retrieved from http://wwwtheijes.com/papers/v2-i4/part.%20(2)/M0242058077.pdf

Obande, O. P. (2015a). Notes on Russellian Cosmogony. II.A procedure for theoretical evaluation of relative atomic mass and internal energy. *Phys. Essays., 28*(1). http://dx.doi.org/10.4006/0836-1398-28.1.78

Obande, O. P. (2015b). Classical mechanical analysis of the atomic wave and particulate forms. *Int. J. Eng. Sci., 4*(6), 1. Retrieved from http://www.theijes.com/papers/v4-i6/version-2/a0462010ll.pdf

Obande, O. P. (2015c). Classical Defifitions of Gravitation, Elelctricity and Magnetism. *Appl. Phys. Res., 7*(6), 85 http://dx.doi.org/10.5539/apr.v7n6p85

Obande, O. P. (2016a). Atomic mass: Origin, Units and Constants. *Appl. Phys. Res., 8*(1), 92. http://dx.doi.org/10.5539/apr.v8n1p92

Obande, O. P. (2016b). On the Photon's Identity: Implications for Relativity and Cosmology. *Appl. Phys. Res., 8*(5), 10. http://dx.doi.org/10.5539/apr.v8n5p10

Obande, O. P. (2016c). A classical perspective of the cosmological constant. *Phys. Essays., 29*(2), 228. http://dx.doi.org/10.4006/0836-1398-29.2.228

Obande, O. P. (2017a). On the Fundamental Physical Constants: I. Phenomenology. *Appl. Phys. Res., 9*(5), 42. http://dx.doi.org/10.5539/apr.v9n5p42

Obande, O. P. (2017b). On the Fundamental Physical Constants: II. Field Coupling Geometry. *Appl. Phys Res., 9*(5), 62. http://dx.doi.org/10.5539.apr.v9n5p62

Oldershaw, R L. (2007). Discrete Scale Relativity. *Astroph. Space Sci., 311*(4), 431. http://dx.doi.org/10.1007/s10509-007-9557-x

Oldershaw, R L. (2014). *A Surprising Similarity Between Stars and Atoms*. Retrieved from http://www3.amherst.edu/~rloldershaw/OBS.HTML

Pauli, W. (1940). The Connection Betweeb Spin and Statistics. *Phys. Rev., 58*(8), 716

https://dx.doi.org/10.1103/ PhysRev.58.716

Peebles, P. J. E., & Ratra, B. (2003). The cosmological constant and dark energy. *Rev. Mod. Phys., 75*, 559.

Peplow, M. (2013). Planck telescope peers into the primordial universe. *Nature News*. http://dx.doi.org/10.1038/Nature.2013.12658

Raghuprasad, P. K. (2013). Planetary spin-orbit attributes in the solar system and their wider implications. *Phys. Essays, 26*(2), 331.

Redd, N. T. (2017). *How big is the Universe*? Retrieved from http://www.space.com/24073-how-big-is-the-univese.html

Reiss, A. G. (1998). *Evidence that the universe has only recently entered on an era of acceleration out of a previous era of deceleration*. Retrieved from http://arxiv.org/abs/astro-ph0104455

Riess, A. G., Macri, L. M., Hoffmann, S. L., Scolnic, D., Casertano, S., Filippenko, A. V., ... & Chornock, R. (2016). A 2.4% determination of the local value of the hubble constant Based on observations with the NASA/ESA Hubble Space Telescope, obtained at the Space Telescope Science Institute, which is operated by AURA, Inc., under NASA contract NAS 5-26555. *The Astrophysical Journal, 826*(1), 56. http://arxiv.org/pdf/1604.0124.pdf

Rubin, V. C. (2000). One hundred years of rotating galaxies. *Publ. Astron. Soc. Pacific, 112*(772), 747. http://dx.doi.org/10.1086/316573

Siegel, E. (2017). *Why Does The Proton Spin? Physics Hold A Surprising Answer*. Retrieved from https://www.forbes.com/sites/startswithabang/2017/04/19/why-does-t...

Slipher, V. M. (1913). The radial velocity of the Andromeda Nebula. *Lowell Observatory Bulletin*, *2*, 56-57. Retrieved from http://adsabs.havard.edu/abs/1913lLewOB...2...56S

Sparknotes. (2015). *The Most Beautiful Outer Space Image of the Last decade*. Retrieved from http://www.sparknotes.com/mindhut/2015/01/12/the-most-beautiful--out...

Spin. (2017). In *Wikipedia, the free encyclopedia*. Retrieved from https://en.wikipedia.org/wiki/Spin(physcs)-20/09/17

Uhlenbeck, G. E., & Goudsmit, S. (1926). Spinning Electrons and the Structure of Spectra. *Nature, 117*, 264. Retrieved from https://lorentz.leidenuniv.nl/goudsmit.html

Uhlenbeck, G. E., & Goudsmit, S. (1926). Spinning Electrons and the Structure of Spectra. *Nature, 117*, 264. Retrieved from http://lorentz.leidenuniv.nl/goudsmit.html

Wikiversity. (2017). *Similarity of matter levels*. Retrieved from https://en.wikiversity/wiki/Similarity_of_matter_levels

Applied Physics Research; Vol. 9, No. 6; 2017
ISSN 1916-9639 E-ISSN 1916-9647
Published by Canadian Center of Science and Education

Reviewer Acknowledgements

Applied Physics Research wishes to acknowledge the following individuals for their assistance with peer review of manuscripts for this issue. Their help and contributions in maintaining the quality of the journal is greatly appreciated.

Applied Physics Research is recruiting reviewers for the journal. If you are interested in becoming a reviewer, we welcome you to join us. Please find the application form and details at http://recruitment.ccsenet.org and e-mail the completed application form to apr@ccsenet.org.

Reviewers for Volume 9, Number 6

Antonio O. Dourado, Hardware Laboratory, Brazil

Balagopalakrishna Chavali, Eli Lilly and Company, United States

Chandrasekhar Roychoudhuri, University of Connecticut, USA

L. Chitra, Mahalingam college of Engineering & Technology, India

Lin Chen, Institute of Fluid Science, Tohoku University, Japan

Pante'a Davoudifar, Research Institute for Astronomy and Astrophysics of Maragha, Iran

Puramanathan Naidoo, Mangosuthu University of Technology, South Africa

Rachid MASROUR, Cady Ayyed University, Morocco

Rami Ahmad El-Nabulsi, Key Laboratory of Numerical Simulation of Sichuan Province, China

Ran Wang, Arizona State Univeristy, United States

Sérgio Costa Ulhoa, Universidade de Brasília, Brazil

Thenappan Chidambaram, College of Nanoscale Science and Engineering, United States

Zhou Xing, Syracuse University, United States

Call for Manuscripts

Applied Physics Research is an international, double-blind peer-reviewed, open-access journal published by the Canadian Center of Science and Education. The journal focuses on the following topics: acoustics, astrophysics and geophysics, biophysics, computational physics, condensed matter physics, engineering physics, free electron physics, laser and quantum electronics, medical physics, optics, semiconductor physics and devices, solid state physics, space physics. The journal is available in electronic form in conjunction with its print edition. All articles and issues are available for free download online.

We are seeking submissions for forthcoming issues. All manuscripts should be written in English. Manuscripts from 3000–8000 words in length are preferred. All manuscripts should be prepared in MS-Word or LaTex format, and submitted online, or sent to: apr@ccsenet.org

Paper Selection and Publishing Process

a) Upon receipt of a submission, the editor sends an e-mail of confirmation to the submission's author within one to three working days. If you fail to receive this confirmation, your submission e-mail may have been missed.

b) Peer review. We use a double-blind system for peer review; both reviewers' and authors' identities remain anonymous. The paper will be reviewed by at least two experts: one editorial staff member and at least one external reviewer. The review process may take two to three weeks.

c) Notification of the result of review by e-mail.

d) If the submission is accepted, the authors revise paper and pay the publication fee.

e) After publication, the corresponding author will receive two hard copies of the journal, free of charge. If you want to keep more copies, please contact the editor before making an order.

f) A PDF version of the journal is available for download on the journal's website, free of charge.

Requirements and Copyrights

Submission of an article implies that the work described has not been published previously (except in the form of an abstract or as part of a published lecture or academic thesis), that it is not under consideration for publication elsewhere, that its publication is approved by all authors and tacitly or explicitly by the authorities responsible where the work was carried out, and that, if accepted, the article will not be published elsewhere in the same form, in English or in any other language, without the written consent of the publisher. The editors reserve the right to edit or otherwise alter all contributions, but authors will receive proofs for approval before publication.

Copyrights for articles are retained by the authors, with first publication rights granted to the journal. The journal/publisher is not responsible for subsequent uses of the work. It is the author's responsibility to bring an infringement action if so desired by the author.

More Information

E-mail: apr@ccsenet.org

Website: http://apr.ccsenet.org

Paper Submission Guide: http://submission.ccsenet.org

Recruitment for Reviewers: http://recruitment.ccsenet.org

The journal is peer-reviewed
The journal is open-access to the full text
The journal is included in:

Bibliography and Index of Geology
EBSCOhost
Google Scholar
JournalTOCs
LOCKSS
NewJour (Georgetown University Library)
Open J-Gate
PKP Open Archives Harvester
SHERPA/RoMEO
Standard Periodical Directory
Ulrich's
Universe Digital Library
WorldCat

Applied Physics Research

Bimonthly

Publisher Canadian Center of Science and Education
Address 1120 Finch Avenue West, Suite 701-309, Toronto, ON., M3J 3H7, Canada
Telephone 1-416-642-2606
Fax 1-416-642-2608
E-mail apr@ccsenet.org
Website apr.ccsenet.org

ISSN 1916-9639